Optimised Chiral Quantum Emission in Glide Plane Photonic Crystal Waveguides

Christopher Steven O'Rourke

A thesis presented for the degree of
Doctor of Philosophy

Department of Physics and Astronomy
The University of Sheffield
United Kingdom

July 18, 2023

Optimised Chiral Quantum Emission in Glide Plane Photonic Crystal Wavegudies

Mr Christopher Steven O'Rourke

Abstract

This thesis presents work on the integration of single-photon emitters inside specially engineered photonic crystal structures. By describing the behaviour of confined electromagnetic fields on the size scales of photonic crystal waveguides, modifications of the crystal parameters can lead to interesting effects. The geometries of these crystals have been designed for a variety of beneficial circumstances relevant to III-V, on-chip photonic networks, such as enhancing emitter brightnesses through the Purcell effect, and directional emission through a unique crystal geometry known as the glide plane symmetry. Specifically, the work is focussed on the study of suspended structures in order to procure highly-chiral, Purcell-enhanced quantum dots that would see plenty of interest for a quantum network.

Additionally, this thesis presents an investigation into the ability to perform single electron spin initialisation within a quantum dot suspended in a photonic structure, contained within a p-i-n diode format. So far, this work has only been shown in a p-i-n-i-n format [1].

Dedication

I dedicate this thesis to my late Dad, who wanted nothing more than for me to finish my PhD, and to my Mum, who constantly ensures that this journey through life is possible.

I finally rest, and watch the sunrise on a grateful Universe.

Publication

- Siampour, H., O'Rourke, C., Brash, A.J. et al. Observation of Large Spontaneous Emission Rate Enhancement of Quantum Dots in a Broken-symmetry Slow-light Waveguide. *npj Quantum Inf.* **9**, 15 (2023).

Acknowledgements

The last five years of my PhD have encapsulated some of the most positive and negative emotional extremes I hope I will ever experience in my life. The most important lesson that I have learned is that life is not a solo experience. I begin by expressing my thanks to all those that have ever been close to me. Thank you to Fran, for making the daunting start of the PhD so much simpler and for being a perfect partner. I express my deepest thanks to my friends who were there for me after my father passed: Elliot, James, Ashni, Michael, Mahmoud, Sajad and Toby. Special thanks to also to Emma and Alfie.

I also wish to thank every colleague with whom I have ever had a conversation in the department, both past and present. Science is, and always will be, a collaborative effort, and we truly do stand on the shoulders of giants...or other lowly PhD students. With this, I give great thanks to the PhD students before me: Dave Price, Charles Whittaker, Dominic Hallett, Joe Maguire, Catherine Phillips, Ian Griffiths and the rest of the coffee-loving, sleep-deprived office members.

I express my gratitude to anyone and everyone that has ever made my day remotely better, by lending an ear, or reminding me what a T_2 time is. Of the present cohort, I give special thanks to Mahmoud Jalali, Toby Dowling, George Gillard, Dan Gillard (no relation, I think) and George Davis. For those that joined after, I thank Alex Morris, Luke Brunswick and Sam Sheldon. Our discussions were always a good balance of scientific debate and utter drivel.

I express my thanks to multiple postdoctoral researchers in the department, namely Dominic Hallett (yes, this is mention number two in the professional capacity),

Alistair Brash, Andrew Foster and Maxim Makhonin (especially for showing me the ropes in the lab). I also wish to thank Hamidreza Siampour, with whom I worked very closely for the final two years. I wish all of you the best in your scientific careers.

Thank you to my supervisor, Mark Fox, for all of the guidance and discussion over all of these years. Many thanks also to Maurice Skolnick and Luke Wilson for their additional support. Many thanks to Professor Richard Warburton and Professor Alexander Tartakovskii for an enthralling viva, providing the final enhancements I needed for a insightful thesis.

I finally give thanks to the rest of the physics department, one I know to be above all others. Many thanks to Matt Mears for all of the discussions over the years, stretching from undergrad to now. Thanks to Ed Daw and Susan Cartwright for hosting random, impromptu discussions about physics. Thanks for David Whittaker and Rhoda Hawkins for handling my most pressing issues, and thanks to Richard Parker, my personal tutor.

Contents

1 Introduction and Background **30**

1.1 Thesis Outline . . . 32

1.2 Quantum Information Processing and Semiconductor Photonics . . . 33

1.3 Quantum Dots as Single-photon Emitters . . . 36

1.4 Quantum Dot Energy Level Structure . . . 37

1.5 On-chip Integration of Single Photon Emitters . . . 41

1.5.1 The DiVincenzo Criteria . . . 42

1.6 The Importance of Chirality . . . 46

1.7 Enhancement of Light-Matter Interactions . . . 48

1.7.1 Photonic Crystals . . . 48

1.7.2 The Purcell Effect - Weak Coupling . . . 52

1.7.3 Waveguide Coupling - The Beta Factor . . . 55

2 Sample Fabrication and Experimental Methods **58**

2.1 Growth of III-V InGaAs QDs on (Al)GaAs wafers . . . 59

2.2 Device Fabrication on Monolithic Heterostructures . . . 62

2.3 Experimental Set-Up, Cryogenics and Sources of External Fields . . . 70

2.4 Spectroscopy, Single Photon Measurements and Time-Correlated Measurements . . . 72

2.4.1 Resonant and Non-resonant Spectroscopy . . . 73

2.4.2 Single Photon Measurements and Time-Correlated Measurements . . . 75

2.5 External Fields 76
  2.5.1 Electric Fields and The DC Stark Effect 77
  2.5.2 Magnetic Fields 80

3 Optimisation of Chiral Behaviour Inside Nanophotonic Structures 83

3.1 Introduction to Nanophotonic Devices and Chirality 84
3.2 Origin of Chirality 86
3.3 The Nanobeam Waveguide (NBWG) 91
3.4 The W1 (defect) Photonic Crystal Waveguide (PhCWG) 93
3.5 The Glide Plane Waveguide (GPW) 95
  3.5.1 The Standard GPW 96
  3.5.2 Modifications to the GPW 99
  3.5.3 The Glide Plane Nanobeam (GPN) 103
3.6 Discussion 105

4 Spin to Path Conversion of QD Excitonic Emission 108

4.1 Determination of the Chiral Contrast 109
4.2 Chiral areas of the Glide Plane Waveguide 111
4.3 Spin Readout of QDs Inside Nanophotonic Waveguides 112
4.4 Measurement of Exciton g-factor 120
4.5 Summary 121

5 Demonstration of Purcell Enhancement Tuning Inside Modified Glide Symmetric Structures 123

5.1 Emitter Lifetime Measurements 124
5.2 The Glide Plane Nanobeam 128
  5.2.1 Glide Plane Waveguides with a Glide Plane Nanobeam taper . 131
5.3 Tuning of Emitter Lifetime Through Application of External Fields . 133
  5.3.1 A Waveguide-Based, Record-Breaking Short Lifetime 137
  5.3.2 Intrinsic Effect of Magnetic and Electric Fields on Lifetime . . 140
5.4 Conclusion 142

6 **Charged QDs and Spin Pumping of QDs Inside Nanophotonic Structures** **143**
  6.1 Electrical Control of Charge-Tuneable Heterostructures 143
  6.2 Resonance Fluorescence and Spin Pumping of QDs for State Initialisation 146
  6.3 The Charging Plateau 149
  6.4 Spin Pumping Inside Nanobeam Waveguides 151
  6.5 Comparison of Spin Pumping Success Rates Between p-i-n and p-i-n-i-n Heterostructures 156
  6.6 Conclusion 157

7 **Further Work and Project Direction** **158**
  7.1 Spin Pumping of Purcell-Enhanced, Chirally-Coupled Emitters Inside Glide-Symmetric Structures 158
  7.2 Use of QD Registration to house Super-Radiant Emission 159
  7.3 Measurement of Phase Shifts through Chiral Resonant Scattering . . 160
    7.3.1 The Implementation of an on-chip Mach-Zender Interferometer for Induced Phase Shifts on Flying Qubits 161

8 **Conclusion** **162**
  8.1 Chapter 3 162
  8.2 Chapter 4 163
  8.3 Chapter 5 164
  8.4 Chapter 6 164

A **Appendix** **167**

List of Figures

1.1 **Density of states for the four different dimensions of degrees of freedom** | Each level of confinement, is colour-coded, with the 3D bulk obeying a parabolic function, the 2D well obeying a step function, the 1D wire obeying an inverse energy relation, and the 0D the quantum dot, which sees a series of mono-energetic states available. The exact locations of these curves are not necessarily important, but it is important to note that all energies are bounded by the free energy of the 0D confinement. Excitonic effects and further quantum confinement effects push the energies further, with the first excited QD state starting above all of the others. 37

1.2 **Carrier band diagram for direct-gap bulk semiconductors** | At zero crystal strain, the light (dashed red) and heavy (solid red) holes are degenerate. The split off (SO - dot/dash line) band exists at zero strain because of the spin-orbit coupling. The parabolic shape is only an approximation for small k values [54, 55] 39

1.3 **Level diagram for the neutral $\mathbf{X}^0$ and singly-charged exciton states $\mathbf{X}^{+/-}$** | A magnetic field splits all three states, lifting the degeneracy of the spin ground states of the charged exciton, and overcoming the exchange splitting from the neutral exciton to restore the circular polarisation of the transitions. Circularly polarised photons carry the momentum between excited and ground states. 41

1.4 **Chiral molecular enantiomer of an amino acid** | This amino acid has a chiral structure, as the reflection about the central dotted line means that the mirror image cannot be aligned with the original image. Choosing any of the individual bonds as an overlap point causes a misalignment in at least one of the other bonds. 47

1.5 **Transmission electron microscopy of a binary super lattice viewed from different crystallographic planes** | Each viewing plane is presented in the inset of the various TEMs. The periodic nature of the CaF_2-style structure is clearly present in all three images. Images from [75]. 48

1.6 **1D photonic crystal cavity with a single hole defect, and the corresponding transmission band structure, showing a photonic band gap and the allowed mode at wavelength λ_0** | The 1D crystal has a period, a, of hole sizes, d. S is the cavity's main region. Transmitted light drops to effectively zero intensity at a particular wavelength, depending on the periodicity and the size of the holes. The allowed mode (red curve) of the photonic crystal, because of the defect, would be a single, dirac delta in principle, but unavoidable hole shape and period imperfections allow for a broadening of this mode. The size of the gap, **s** determines the spectral position of the cavity (allowed) mode. 50

1.7 **A waveguide coupled to a 2LS depicting the consequence of a β factor** | A single photon propagating along the waveguide, from the left, interacts with the two level system, whose resonant energy is $\hbar\omega$. Light is either, in principle, reflected, or transmitted, or lost from the waveguide through the factor of 1-β. The reflection or transmission should occur with the rate of β. The addition of $\pm\Delta$E accounts for the possibility of off-resonant interactions between the light and the emitter. 56

2.1 **Layering of p-i-n heterostructure wafer** | Doping is achieved for the p- and n- layers by Beryllium and Silicon doping respectively. The QD layer is the 0.7nm InAs layer, and the top p- and bottom n- layers are connected to Ti/Au contacts. 59

2.2 **QD Island formation method** | Deposition of InAs (yellow) creates a strain mismatch. After a certain amount of material has been deposited in stage (a), stage (b) island formation occurs. The InAs QDs are topped with more (blue) GaAs as seen in (c), which does admix with the InAs slightly. 60

2.3 **Linewidth distribution of random but bright QDs on a sample** | A sample denoted "SF1520." A diode contact is fabricated without nanophotonic devices to study individual QDs. Low power micro-photoluminescence is used to collect these individual QD lines. A skewed normal distribution provides a 34.8μeV mean over the 128 QD lines studied. 61

2.4 **SEM of 24 devices + 5 nanobeam waveguides** | The horseshoe gold contact is the elevated surface surrounding the numbered devices. This image is before the 3-point cleaning stage, which takes place before the wire contact bonding. 64

2.5 **Cross section of the photonic device etching stages** | An electron beam resist first coats the grown p-i-n wafer. This resist is then exposed to the EBL. This exposed resist is then developed, allowing for the RIE and ICP to quickly lift up the GaAs material, as is seen in **(e)**. Step **(f)** encompasses the processes of figure 2.6 but represents the end goal. The etching steps are described in detail in the text. . . 65

2.6 **Cross section of nanophotonic devices undergoing the critical point drying process** | Deionised water, used to wash away the HF to halt overetching, is eventually replaced by air through the CPD process. Similar to the main etching process, details are provided in the text. Each stage is depicted in the order progressing left to right, first along the top row and then the second row in the same fashion. Each stage involves a chemical in a thermodynamic state that is miscible with the contents already present. 66

2.7 **Optical image of a final bonded chip, mounted on a non-magnetic ceramic carrier** | Each external, gold-painted pin is exclusively connected to individual diodes, except the ground pin, which has multiple contact points to prevent overall contact failure (as it is common to all diodes). These pins are labelled GND and 2 → 20. Glue sticks the wafer to the carrier to maintain alignment once placed into the cryostat, and to prevent further tension on the small gold wires. The different decimal values pasted across the arrays of horseshoes indicate the different EBL doses, generating different true values of etched hole sizes. 68

2.8 **Room temperature (RT) and cryogenic temperature (LT) IV characteristics for the diodes used in chapter 6** | The coordinate labels are defined relative to the matrix of diodes shown in figure 2.7, with the bottom left being (1,1) and the top right being (4,4). Only five pins are available in the cryostat for low temperature study. Diodes are chosen based on their design, SEM quality and electrical response. The colours marked on the LT plot are the same as in the RT plot. The low voltage behaviour (in the LT graph) of the low temperature plot is likely not due to the full diode behaviour, and is probably a contact resistance that accidentally forms from contracting material. 69

2.9 **Experimental set-up used for probing samples discussed in chapters 4-6. Some components, such as polarisers, aren't shown as they do not appear in all experiments** | The excitation laser of segment (a) is either a non-resonant diode laser, a tuneable CW/pulsed laser, or a white light laser. Through the variable ND filter wheel, laser light can enter segment (b) with a user-defined power. Segment (b) depicts how light from (a) is passed towards the sample, (c), dictated by the red beam. The beam splitter is 50/50 to gauge how much power is directed to the sample. The green PL leaves the sample and is sent to the detection region. 71

2.10 **Example QD lifetime data of a QD integrated in a nanobeam waveguide** | Each datum represents one in a series of time-resolved PL measurements resulting from pumping a QD with a laser pulse. The QD is more likely to emit at shorter lifetimes, and the probability is governed by the lifetime of the emitter. The bottom half of the data set is fitted with an exponential decay (in red) to avoid fitting a convolution of the detector response. Knowing the temporal detector response to the pulse excitation laser allows the fitting of a convolution, but this is mitigated by fitting the lower half of the curve. 75

2.11 Photoluminescence is obtained under a 1s exposure of 4W of applied laser power at 808nm. At each voltage step between -1000mV and 5000mV, a PL spectrum is taken. The bright spots are cosmic rays. The doublets of lines are because of the magnetic field's effects. The tuning range begins at a similar location to the current (turn-on) response, around 1.5V. Around 1.5nm of tuning is applied to the QD lines over a 1V range, after which the intensity remains the same. Eventually, carriers can tunnel directly from the p- and n- contacts to directly produce electroluminescence, though the effects are not obvious here. Some QDs do not appear to charge, but many do. The reason is unclear. 79

2.12 **Neutral, positively, and negatively charged exciton states** | These states are under a magnetic field to lift the degeneracy of the ground states of the charged species. The B field also overcomes the FSS and restores the circularity of the neutral exciton recombination paths. 81

3.1 **Series of scanning electron micrographs of various nanophotonic designs** | (a): a ring resonator of radius 2μm and 350nm width; (b): quantum valley-hall [111] topological waveguide; (c): standard nanobeam waveguide; (d): multi-mode interferometer (MMI) splitter. 84

3.2 **Layout of a rectangular nanobeam waveguide, clad in air** | The dimensional size of 183 x 270 nm reflect the nanobeams which appear on the diodes present for the work in chapter 5. The axes are specified such that the z axis is the longitudinal direction, and the x-z plane is normal to the growth axis, along y. The InAs layer of QDs is at the middle of the height, 91.5nm along the y-axis. 87

3.3 **Phase between the z and y components** | Phase relationship of the two circularly polarised states within the nanobeam waveguide. Here, the y direction the same as the x direction in figure 3.2. The phase is constant apart from very, very close to the centre, at which point is flips. Figure taken from [100] 89

3.4 **Birds-eye view of the circular polarisation (S3 parameter) of an infinite (left) and terminated (right) nanobeam waveguide** | The pattern of the terminated plot is caused by Fabry-Perót oscillations cause by the effective cavity introduced by the outcouplers of the device. Were the reflectivities of the boundaries between the waveguide and outcoupler 0, the plot would be similar to the infinite case. The black outlined areas are regions of chirality greater than 90%. Plots are courtesy of D. M Price, see ref [100]. 90

3.5 **Various light extraction devices from Sheffield** | Shallow-etch grating **(a)**, featuring theoretically high extraction efficiencies (60%) (X. Zhou 2018) and low back scattering. Design (b) is a modification of the standard double-annulus ring grating shown in (c). Part (d) is a tapered fibre, designed to couple to a second fibre which directly connected to single photon detectors. 92

3.6 **Dispersion of the standard W1 defect PhC and modifications to this from ref [121]** | The blue circled region of the W1 dispersion is the region of interest, with the light line (the dotted diagonal) to the left side of the dispersion bands. The colour contour plot on the right indicates the amount of chirality when altering the 2D parameter space of D1 and D2, as seen in the black cartoon. The heat map along the bottom simulates a circular electric dipole at the most chiral point for the best D1 and D2 parameters. 94

3.7 **Depiction and dispersion of the unmodified GPW** | (a): the unmodified crystal. (b): the GPW dispersion. The overlap in the dispersion between the two modes means that emitters within this spectral position can send light to either of these modes. Each mode has a different electric field distribution, and therefore even if the S3 Stokes' parameter is the same, the chirality will be highly perturbed by the mismatch of intensities. 97

3.8 **Waterfall QD PL emission transmission series of unmodified glide plane waveguides** | Each μPL trace is obtained by shining the outcoupler of one end of a device with high above-band laser power, and collecting at the other outcoupler, forming the transmission data. The band edge of the devices can be seen to change as the device number increases, as there is little-to-no intensity at the higher device numbers towards the longer wavelength section. The blue-highlighted region comprises large intensities around 870nm, which is the wetting layer excitation of the sample. Some devices showed very minimal transmission, and this is discussed further in the next section, and outlined by figure 3.10. 98

3.9 **Dispersion of a modified GPW, and the corresponding design.** | The original crossing point in the dispersion is lifted from un-modified glide plane. The row of smaller holes are the ones displaced. The altered sizes are discussed later in the text. Image from [123]. 99

3.10 **Dispersion of a W1 and a GPW side by side, and an FDTD simulation of the adjoined crystals.** | The slow light region of the GPW and a similarly indexed region of the W1 are marked. The horizontal lines reaching to the vertical axis of a/λ correspond to the upper W1 cut off and the GPW slow light region. Using the resulting parameters, a design is simulated on the bottom of the figure, which shows a circular dipole source reflected between the interfaces of the GPW and W1. Any transmission is essentially allowed by the tapering between the crystal varieties and the subsequent reduction of the efficacy of the simulation caused by the limited periodicity of the crystal. Band structures generated by C. O'Rourke in FDTD, bottom simulation performed by H. Siampour in FDTD. 100

3.11 **Scanning electron micrograph of a GPW design with a W1 PhC defect adapter** | Named design II, the size of the first row of holes remain unaltered relative to design I, which only lifts the dispersion's degeneracy as seen in figure 3.7 as this is a modification made to the later designs. The GPW pattern is adiabatically tapered to match the W1 periodicity, which has the same periodicity. The residue surrounding the nanobeam area in the W1 section is removed before diode bonding. 101

3.12 **Chiral QDs collected across different GPN devices** | 808nm laser light is directed onto the GPN from above, and the subsequent PL is collected at each outcoupler (Collect Right/Left - CR/CL) under a both a magnetic field and at 0T for reference. The chiralities are marked, and were calculated by studying the integrated areas under the curves and by entering the values into equation 3.2. The chiralities of the GPN are not as impressive here as they are in the GPW. This is both due to the band gap obfuscating the spectral availability of QDs, and the intrinsic chirality being less. 102

3.13 **Dispersion of the GPN (left) alongside the directionality (top right) and the Purcell profile (bottom right)** | The blue-circled area is the spectral region for which the two rightside diagrams are valid. The directionality is anti-symmetric about the central axis. The strongest field strengths (which directly correlate to the Purcell profile) occur either in the air holes or very close to the surface, both of which are essentially useless for embedded emitters. Dispersion simulation performed by H. Siampour in MPB. Purcell and directionality profile simulated by C. O'Rourke in FDTD. 103

3.14 **Chiral QDs collected across different GPN devices (bottom right)**| Data is collected at each outcoupler under a single magnetic field, and is also collected at 0T. The chiralities are marked, and were calculated by studying the integrated areas under the curves and by entering the values into equation 3.2. 104

3.15 **Summary of the devices mentioned in this chapter** | Red, blue and green refer to poor/undesired, moderate, and good/desirable properties respectively. A description of each design, alongside the amount of chirality, the Purcell enhancement and the β-factor is provided in that order in the third column. The strength of the GPW over the standard nanobeam and the GPN is size of the area for which the chirality is beyond 95%. Each design has either an SEM or a representative diagram of the devices in question. 106

4.1 **Principle of exciting an emitter and collecting light from outcouplers in a nanobeam waveguide** | This depiction describes either PL or resonant QD excitation for spin-to-path conversion. Incident light excites one of the QD spin states, as marked by the blue/red arrow and light is emitted in one direction or the other depending on the polarisation of the light associated with the QD spin, corresponding to blue or red, depending on what colour was used to excite the system. 109

4.2 **(a): QD PL and a Gaussian fit to the QD peak with extracted fit parameters of curve area and peak height, (b): μPL spectrum of a mildly chiral (split) pair of lines to demonstrate the importance of using the calculations presented in the text** | The vertical blue dashed line in **(a)** indicates exemplary boundaries where the summation of individual counts would take place for the calculation discussed in the text. The red and blue data are separate spectra collected from two exposures under the same conditions. By taking the appropriate ratios of the integrated areas, the calculated chirality for the data in **(b)** is C=-6%. Conversely, the chirality for merely taking the extracted peak height (labelled as H in **(a)**) is 20%. 110

4.3 **Comparison of experimental distribution of QDs in the GPW and NBWG** | Plotted on the left are data for the glide plane waveguide. Contrasts are obtained at various magnetic fields, from QDs ranging in emission wavelength from 870nm to 934nm, across a multitude of devices with slightly different fabrication parameters. The red curve over the top is a skewed distribution which indicates that 50% of QDs have a chiral contrast of at least 70%. The right hand side shows data collected for QDs within a nanobeam waveguide from [100]. 112

4.4 **Coarse FDTD simulation of electric field polarisation within the modified GPW, design III** | The colour map indicates the strength of the directionality ranging between 1 and -1 across the crystal. The white circles are etch holes, and no emitter can be found within them. Even when subtracting this area, 39% of the area should house > 90% chiralities. 113

4.5 **PL transmission along a standard suspended nanobeam waveguide.** | There is little spectral intensity dependence apart from shorter than 900nm, which is due to a spectral filter to remove the wetting layer PL. The brightness oscillations are due to Fabry-Perot interference due to the outcoupler reflections. The separation of the peaks (known as the free spectral range) allows for a calculation of the refractive index, as shown in equation 4.1. 114

4.6 **(a): μPL for a QD collected directly above it, and from either of the GPW device outcouplers. (b): Broadband collection μPL demonstrating the effectiveness of grating outcoupler collection** | One second exposures for all three collection regimes show the potential β-factor of the QDs within the nanobeam. From the single QD in **(a)**, there is very little intensity change between the outcouplers, and this QD could host any level of chirality. **(b)** shows that generally emission is way brighter when collected from an outcoupler, in red, compared to whent he light is collected from directly above the excitation location, in black. 115

4.7 **Symmetric (a) and asymmetric (b) chiral QD data** | Two QDs are present in (a), each split by a magnetic field of 2T. The data of (b) shows the QD emission collected above the waveguide in black. Red and blue show different chiral contrasts when collected at different outcouplers, even though the QD is the same. 116

4.8 **Contrast of elliptical emitters for an ellipticity magnitude of 0.1π** | A birds' eye view of the field in the nanobeam. The anti-symmetry between both plots are for $\pm 0.1\pi$. Importantly, there is no overlap between the two plots when they are overlaid. The result are seen in figure 4.9. 117

4.9 **Resultant (summed) phase plots of an elliptical emitter** | For a non-zero phase difference, this plot would be empty. The $\delta_{phase} = 0.1\pi$ produces ellipticities of 30%. 118

4.10 **Plot of the β-factor with respect to the lateral QD position within a waveguide. Simulations performed by H. Siampour** | Shown for two different wavelengths, the beta factor was calculated by measuring the fraction of total transmitted power along the waveguide, relative to the system input power, which is a known parameter of the simulation. The coloured plot shows the Purcell profile of the waveguide. The beta factors of emitters at different positions along the x-axis labelled 1 → 20 correspond the small black circles in the bottom left inset. 119

4.11 **Zeeman splitting vs. magnetic field** | A series of PL peaks are fitted, and the central positions are found for each of the plots. The linear relationship is generated by finding the difference between both components' fit. Consequently, the diamagnetic shift is eliminated, as it affects both components equally. The g-factor for this QD was 2.10±0.02. 120

5.1 **Lifetime measurements for bulk, outcoupler and nanobeam waveguide QDs** | Each data point is either from a high power PL ensemble, or low power single QD PL. The difference between bulk data and nanobeam data is minimal, demonstrating a very small average lifetime reduction of <0.1ns 125

5.2 **Experimental (a) and theoretical (b) dispersion diagrams of a device with emitters of un-enhanced lifetimes (c) away from the slow light region. Spectral locations shown in (d)**. | R and T in part **(a)** stands for the reflection and transmission of light from one outcoupler to another. Different applied voltages and magnetic fields (from 0V to 2.2V and -4.5T to +4.5T respectively) show the lack of explicit changes to the emitter lifetimes caused solely by the fields themselves. The legend in (c) shows the applied voltage and magnetic field for each of the series of lines. Three distinct QDs are featured. Pairs labelled I & II, III & IV and V & VI are iterations of the same three QDs under different voltages or magnetic fields. The QDs between (c) and (d) are labelled. They are located approximately in the black circled area of the dispersion diagram of (b). While the QDs are very close to the light line, their brightnesses are relatively dim when compared to other emitters in the crystal, and long exposures were used to obtain the lifetime plots shown in (d). Figures 5.12 and 5.13 show specific voltages and magnetic fields present for the record-breaking lifetime QD, for different emitters on the same sample. 127

5.3 **Glide Plane Nanobeam Transmission spectra for three devices with periods: $\mathbf{a_{11} = 258nm, a_{16} = 262nm}$ and $\mathbf{a_{21} = 258nm}$** | μPL transmission of various devices. Each device demonstrates a different onset for the beginning/end of the opacity window or pseudo-band edge. Moreover, the transparency window for devices 16 and 21 are visibly different in magnitude, with the red curve extending into longer wavelengths, owing to both the different hole sizes $r_{21} = 0.3a_{21} = 77nm; r_{11} = 0.28a_{11} = 72nm$ and $r_{16} = 0.28a_{16} = 73nm$ and periods. 129

5.4 **Glide plane nanobeam directional emission** | Colour-coded μPL for QDs collected: directly above the glide plane nanobeam (light blue) and above a grating outcoupler to measure the light coupled into the GPN (red). Presented also is the transmission spectrum (black), where the band gap (marked at 913nm and 928nm with grey lines) marks much lower intensities of coupled PL, as seen by the dimmer red lines relative to the blue lines across the full spectral window. The red and black curves show a similar dip in intensity within the band gap, whilst, as expected, the blue PL shows emission, as this light does not transmit through the crystal. 130

5.5 **Transmission for four devices of the full optimised GPW, with the glide plane centre and GPN adapter.** | Highlighted in grey are the slow light regions for each device, with the blue line indicating the centre of it. Red indicates the predicted band gaps for the glide plane nanobeam adapater, assuming an infinite number of 1D lattice holes. The differently highlighted regions show that the GPW slow light region need not be contested by the band gap of the GPN. Marked are designs 1 (a=250mn), 5 (a=254nm), 10 (a=258nm) and 11 (a=258nm). 132

5.6 **PL tuning map for a magnetically split QD line located in device 10, whose dispersion appears in figure 5.7** | Marked is the central wavelength before the magnetic field of 3T was applied, and the final wavelength after the same QD state is tuned to 5V. This shift of ~1.7nm is typical, but does not take place close to the slow light region of this device. 134

5.7 **Dispersion for the glide plane waveguide region of the device containing the $F_p = 15.1$ QD from table 5.8** | Left: Dispersion for the QD in figure 5.6. Both the dispersion and the group index (convertible to the lifetime enhancement) are plotted against the wavevector, k. The labelled points, 1 → 2 show the energy shift from the QD in figure 5.6. Right: Simulated dispersion, showing how the same energy shift magnitude could change the group index drastically. 135

5.8 **Table containing a series of slow light QDs with their chiralities (if applicable) marked.** | Devices labelled are in accordance with those seen in the SEM of figure 2.4, alongside the device's re-estimated cut-off regions. The wavelengths, lifetimes and chiralities of the selected QDs are presented in the same order. A full series of PL spectra, alongside the device's cut-off points are presented in the appendix. QDs with very little discernible directional contrast, or QDs with only one component appearing in the magnetic field spectra, are marked as ∼0% and > 99% respectively. 136

5.9 **Dispersion for the glide plane waveguide region of the device containing the $\mathbf{F_p = 15.1}$ featured in figure 5.11** | As the wavelength of the emitter is shifted within the glide plane, the detected lifetime gets shorter over the range demonstrated in figure 5.10. Labelled here are the light line cut-offs, with the upper band being well into the wetting layer emission region (∼880nm) and the lower cut-off near 980nm. Simulation by H. Siampour. 137

5.10 **μPL map for the QD featured in figure 5.11, device 11** | The right QD line experiences an energy shift of around 1.5nm due to the externally applied bias, under a CW excitation scheme. Further tuning is from the application of different powers from the pulse laser. The dotted lines show the three main voltages for which the lifetime is recorded. The specific experimental circumstances are outlined in the text. 138

5.11 **Lifetime exponential decay progression for the QD under above-band and phonon sideband excitation** | As the wavelength of the emitter is shifted within the glide plane, the perceived lifetime gets shorter over the range demonstrated in 5.10. The different conditions of study for each data point are explained in the text. Shown in the inset is a zoomed-in version of the three shortest lifetimes, with the Purcell enhancements labelled rather than the lifetimes as is in the main figure. 139

5.12 **Example ensemble PL (a) and individual QD lifetimes at applied external voltages (b)** | Highlighted in (a) is a typical PL spectrum used to obtain lifetime measurements for those produced in (b). A spectral filter is used to only obtain light present in the lines behind the yellow filter. Across the range 0.5V to 1.3V, no change in ensemble bulk lifetimes are observed, as expected for an electromagnetically unmodified environment. 141

5.13 **Example ensemble PL (left) and individual QD lifetimes at applied external voltages (right) for QDs in a suspended nanobeam** | Shown on the left are the ensemble spectra associated with the lifetime data points of the right. The individual μPL are shown (unlike in the case of figure 5.12) as they differ at the voltages shown. Only the QDs at 2V seem to differ in lifetime, but this could be attributed to additional short-lifetime QDs that appear in the spectrum. 142

6.1 **Spin Pumping of a charged exciton, with lifted degeneracy of the ground state** | The colours illustrate the energy differences indicated by the distances between the transitions, which are arrow marked. As in figure 1.3 of the introduction, the arrows represent carrier spins. The green transitions allow for the shelving of the carriers, which are normally pumped up and down the red and blue transitions, depending on the carrier spin. 147

6.2 **(a): p-i-n vs (b): p-i-ni-n** | Colour coded on the right are the doping profiles, positively doped by the p label in red, and negatively by the n in blue. "i" (grey) indicates neutral doping and contains the thin QD layer, as seen in (**a**). The p-i-ni-n has a smaller voltage across the QD region in the centre than the p-i-n. (a) from [137], (b) from [1]. 148

6.3 **PL map to find a charged exciton, and micro-photoluminescence of a magnetically split line under consideration for spin pumping** | The QD would be identified in the boxed region of the PL map. Linewidths are at least within the resolution limit of the highest order grating on the spectrometer (~9pm). This QD is the QD for which spin pumping failed, despite the obvious identification of a charged exciton. 150

6.4 **Voltage plateau for a QD in zero field (left) and a non-zero B field (right)** | Both images are experimental data, showing the success of spin pumping at the centre of the voltage plateau. A resonant laser is scanned across a range of 70μeV across zero detuning. Images from [138] 151

6.5 **RF voltage plateau along the diagonal of the full contour plot (shown in 6.4)** | The brightest RF curve along the plateau is shown on the left, and the brightest sections of the full diagonal profile is shown on the right. The Gaussian lineshape is expected for the diagonal plateau. The red data point is excluded from the fit. . . 153

6.6 **Spin pumping signature for a charged QD. Left is at the centre of the plateau, right is at the plateau edges.** | Signal intensity quickly drops as soon as a magnetic field is applied at the plateau centre, in accordance with the electron spin becoming shelved/initialised. The fitted Gaussian curves drop over 5x in integrated area between 0T and 0.1T. The right side of the 0.2T data could not be fit as there is no appreciable curve. No clear sign of signal decrease occurs for the plateau edge data, shown on the right, which maintain their magnitudes. 154

6.7 **(a): RF at zero magnetic field for a QD which did not experience spin-pumping. (b): Demonstration of RF failure through fields up to 0.5T** | (a): Sub-3pm RF at 0T, in the centre of this QD's plateau. (b): Spin pumping attempts at the centre of the plateau. The QD spectrally moves similarly to the one in figure 6.6, but there is no appreciable quenching of the RF intensity, even though the data is taken at the centre of the RF plateau. The central wavelength of each curve is marked explicitly to denote the differences in energy induced by the magnetic field. The broadening of the 0.5T curve is discussed in the main text. 155

A.1 **Second order correlation of the tuned QD from figure 5.11** | (a) shows the $g^2(0)$ when the QD is tuned to the shortest wavelength, seen in (b). When convolved with the detector response, the $g^2(0)=0.11$. The $g^2(0)$ without deconvolution when the QD is at the longer wavelength is shown in (c), with a value of 0.16. This proves the single photon nature of the emitter. 167

A.2 Two spectra are presented for Device 1, in red (filtered) and black. The blue line indicates the slow light position, and the grey shading indicates a 10nm window either side of it. Lifetimes of QDs are arrow marked. 168

A.3 The blue line indicates the slow light position, and the grey shading indicates a 10nm window either side of it. Lifetimes of QDs are arrow marked. 169

Chapter 1

Introduction and Background

The last few decades have seen an emergence in nanofabricated technologies with a particular focus on the generation [2–5], control and moderated interaction [6–8], storage [9–12] and detection [13–15] of quantum information. There has been a paradigm shift in the direction of scientific advancement to follow the inspiration of the late Richard Feynman, whose seminal lecture [16] outlined the necessity of quantum computers for simulating quantum systems. Of the myriad of ways in which quantum information can be handled, one of the most promising categories is on-chip, photonic computation. In 2000, David P. DiVincenzo set out a famous list of requirements [17] that any hardware desiring to fulfil basic quantum information protocols should follow, and it will be discussed later in this chapter how the work presented in this thesis fulfils those criteria.

A variety of platforms have been proposed over the years to realise the hardware requirements of the DiVincenzo criteria, each having a plethora of advantages and disadvantages for carrying out quantum computing, quantum metrology and quantum cryptography. The III-V semiconductor platform has seen widespread implementation as a quantum network technology, with the ability to host emitters [18] as well as becoming more easily integrable with detectors.

The ultimate goal of the III-V quantum technology space is to develop a system whereby the production, manipulation and detection of qubits can take place on a single chip, ideally using light as the mobile information carrier.

However, photon-photon interaction probabilities are zero by all relevant definitions [19], with even pair production events in particle physics being governed by vacuum fluctuations of virtual charges. To bypass this weakness, matter-based elements are embedded within the on-chip network in order to introduce a far stronger light-matter interaction. In this research area, quantum dots are by far the most popular candidate as an interaction mediator for the transported light. The on-chip distribution of information is of vital importance if one wishes to deterministically influence and moderate qubit interaction [20], but performing this on-chip is difficult without highly-accurate emitter placement. One of the more popular techniques of controlling the flow of light within the semiconductor platform is with the use of photonic crystal waveguides, whose behaviour hybridises the benefits of cavity enhancements as well as efficient photon transport.

In order to ensure photons are transported in a desired direction, the photonic crystal environment can be tailored to introduce regions where the polarisation state (or spin angular momentum) is linked to the direction of emission, via a mechanism known as spin-momentum locking [21, 22]. This concept has been extensively demonstrated for atomic physics, where circularly polarised light incident on a series of cold atoms leads to almost perfect unidirectional emission from the evanescent fields leaking into a nanofibre next to the trapped atoms [23, 24]. For the III-V platform, few styles of photonic crystal design allow for efficient directional emission as well as maintaining the benefits of the popular W1 (defect) photonic cystal crystal waveguide. This thesis presents the design and experimental demonstration of a series of photonic crystals known to have a *glide plane* symmetry, which allows for efficient chiral transport with few drawbacks. Additionally, an efficient adapter that allows effective transmission of light from such glide plane structures to suspended nanobeam waveguides is presented, both as part of an integrated architecture and on its own.

1.1 Thesis Outline

This introductory chapter will provide discussion for the motivation of quantum information processing, followed by a modestly detailed explanation of the use of semiconductors in photonics. Basic information about the primary sources of single photons in this work (the quantum dot - QD) will be presented, followed by the assimilation of these sources into semiconductor devices. As a summary to these two sections, the DiVincenzo criteria will be presented, with a discussion of how QDs integrated into semiconductor architectures provide one successful avenue which fulfils the five ("plus two") criteria that are presented in his paper. Finally, the importance of chirality will be briefly introduced.

Chapter 2 will outline the experimental procedures used in this thesis. It will begin with a description of the growth of III-V Indium-Gallium-Arsenide (InGaAs) QDs, followed by the design and execution of the lithographic, dry, and wet etching, as well as depositional mechanisms used to generate electrical contacts and the photonic structures themselves. The following subsections will detail the methods used to perform the different measurements that took place over the course of this research, including: the application of external electric and magnetic fields; different laser excitation methods such as (quasi-) resonant, pulsed and CW non-resonant; and the different detection/collection schemes such as micro-photoluminescence (μPL) for time-correlated spectroscopy.

Chapter 3 will introduce the main scope of this work: Optimisation of Chirality in Nanophotonic Structures. Starting with fundamentals of light confined to structures whose size is the order of the wavelength of light used, a narrative will be presented that details how the benefits of different types of photonic structures have been hybridised to develop four styles of *Glide Plane* photonic crystal waveguides. Individual discussions of each type of structure will be presented, with simulation of band structures and various figures of merit.

Chapter 4 will present an experimental study of the structures described in chapter 3. It begins with a description of the principles of directional readout, and an empirically-driven discussion of the probing of excitonic states of QDs inside various photonic devices. This chapter will also present an empirical study of the chiral areas possessed by optimised glide plane devices.

In line with the postulates of chapter 3, chapter 5 will present a specific experimental study of one of the species of glide plane waveguide (GPW). Here, the demonstration of tuning the Purcell factor experienced by integrated emitters is presented in the novel context of highly chiral devices, and the results of a record-breaking enhancement for a QD within a passive structure is shown.

In chapter 6, preliminary work will be presented for the case of initialisable emitters inside nanophotonic structures. A QD inside a nanobeam waveguide is presented within a p-i-n diode, with a demonstration of spin initalisation, thought to be only possible within a p-i-n-i-n type layering.

Chapter 7 will provide an outlook for future project direction for each of the individual avenues presented.

1.2 Quantum Information Processing and Semiconductor Photonics

At the turn of the century, a concept for scalable quantum information processing was proposed by Knill, Laflamme and Milburn in 2001 [25]. What became known as the KLM scheme, the ideas presented in their paper can be described as a protocol whereby linear optics, with simple projective measurements, provides a complete avenue for scalable quantum computing [26, 27]. With the inclusion of methods to integrate error correction, the KLM scheme was a driving force for QIP technologies, as it was then deemed possible to not require strong nonlinear interaction of multiple optical modes. With such a scheme, linear optical quantum computing (LOQC) should be possible within the on-chip platform, especially with enough workable units (ancilla) to perform error corrections to achieve perfect QIP, provided that the quantum memories embedded within the network have reasonable lifetimes.

Photons possess the most promising attributes as a flying qubit, and are deemed as attractive candidates for a plethora of reasons. One such reason is the ease of generation, such as those generated through spontaneous parametric down conversion (SPDC)[28, 29], nitrogen vacancy (NV) centres in diamond [30, 31], or quantum dots [32]. In principle, photons are readily able to be entangled if they are generated at the same time; whether this is through frequency entanglement from processes such as spontaneous four wave mixing (SWFM) [33–35] or the biexciton cascade [20], polarisation entanglement (as can be achieved in SPDC [29, 36]), or on-chip which-path entanglement [37]. It has also been shown that time-bin entanglement is possible for two temporally separated photons to be entangled if their indistinguishabilities can be maintained [38, 39]. Additionally, photons possess strong anti-decoherence properties over long time scales due to their weak photon-photon interaction probabilities.

The strong anti-decoherence properties championed by photons is also the fundamental weakness. Their intrinsic self-shielding of information that they carry from external deleterious effects implies interaction strengths of zero with one another. This means that entanglement is difficult to impose from two separate photon sources through mere free space optical manipulation. Even in the cases of SPDC and SFWM, for example, large powers (i.e. input laser photon numbers) are required to generate a sufficient number of single photons in the output for satisfactory processing. In order to overcome this weakness, semiconductor-based architectures are used, in the context of a light-matter interaction, which enhance the ability to generate (entangled) photons with a much better input/output photon efficiency.

The semiconductor platform most provides access to develop compact architectures which can demonstrate on-chip, photon-based QIP. A variety of materials can be put forward for the use of optical processing, such as non-linear crystals (BBO, KDP and $LiNbO_3$) or diamond (with colour centres provided by implanting group-IV elements). The most robust material to interface QIP, however, is the semiconductor platform. The most commonly used semiconductor material across all markets is

Silicon. With this in mind, it is also a very active competitor as a research material in the world of quantum logic networks and photon routing. Silicon is cheap, accessibly manufacturable, and has a transparency window (1.55μm) that matches what has developed into the telecomms market. With these properties, silicon-based architectures see plenty of application as waveguides, grating couplers [40], directional couplers [41, 42] and more [43]. However, silicon-based circuits do not have readily available single photon sources, and lack the ability for efficient radiative emission in general due to the material's indirect band-gap. There have been many attempts in order to align the practical uses of silicon with single photon emitters, such as placing III-V material with an embedded (InAs) QD atop a silicon nitride waveguide [44], or instead a colloidal (CdSe) QD.

Even cutting-edge hybrid systems (with the SPSs being non-silicon based) do not match the efficiencies of complete III-V (non-silicon based) systems, which are the featured light source and guiding material in this thesis. While these systems are still only a few years old and thus in an early research and development stage, implementing colloidal dots into semiconductor networks is proving a difficult challenge to achieve efficient results, as blinking and spectral wandering drastically hinder the coherence of emitted photons. This disadvantage goes further, in that sequentially emitted photons can be largely distinguishable, as well as photons which are temporally and numeratively well-separated. By contrast, quantum dots as single photon sources prove very stable, showing indistinguishabilities between photons that are 150 emission events apart [39]. Quantum dots as emitters is discussed in the next section.

1.3 Quantum Dots as Single-photon Emitters

There are a variety of potential sources for both the static and flying qubit; such as trapped ions/atoms [45, 46], nuclear spins [47] and Cooper-pair boxes [48, 49] (or charge qubits). However, quantum dots are often hailed as the most promising single photon source and static information holders, matched (and arguably superseded) only by defect centres in diamond, such as nitrogen or silicon vacancies. Offering more than a capacity of strong state purity and anti-bunched emission, QDs have a surplus of advantages for the SPS of choice. QD emission can be triggered electrically [50], spectrally tuned and have their static qubit (excitonic) state fully controlled with optical pulses [51]. The advantage over using diamond as a single photon source relies on the simplicity of on-chip integration of the QDs inside inorganic semiconductor materials, a promise of scalability through (un)registered random growth or site-controlled growth, and a more easily achieved state purity due to narrower linewidths in QDs (though this does require a lot of fine-tuning of growth parameters). The growth process of self-assembled QDs is described in the next chapter in detail. Moreover, QDs posses the capacity of being subjected to cavity enhancements both in waveguide and vertically-emissive settings (such as an H1 cavity).

The QDs discussed in this thesis are Stranski-Krastanov (SK), III-V InGaAs dots. The direct-gap nature of III-V In(Ga)As QDs allows for strong, bright emission. Another type of QD is the colloidal quantum dot, whose atomic-like properties can match those of the SK dots in likeness, but not to such a prominent extent. Specifically, although colloidal QDs show characteristic emission per QD due to some carrier confinement even at room temperature, and can be easily integrated into a variety of physical systems due to their specific structure, the linewidths provided do not usually approach those achievable by SK QDs [52], and the colloidal QDs are more subject to the possibility of large carrier occupancies at higher excitation powers resulting in unwanted cascaded emission [53]. Additionally, colloidal emitters suffer from strong line broadening which can suggest strong dephasing, and spectral blinking, whereby charges migrate or non-radiatively recombine at rates comparable to the photoluminescence.

1.4 Quantum Dot Energy Level Structure

The QD has a discrete density of states (DoS) within the semicondcutor environment, differing to those of the three-dimensional (3D) bulk semiconductor material, the 2D planar quantum well, and the 1D nanowire. This is depicted in figure 1.1. Considered zero-dimensional, with no kinetic component to the energies of confined carriers inside the material, the confinement provided by the QD in all three dimensions results in a discretised emission spectrum when studied under a variety of illumination conditions. Often regarded as “artificial atoms,” the individual spectral lines associated with the capture and subsequent recombination of charges inside

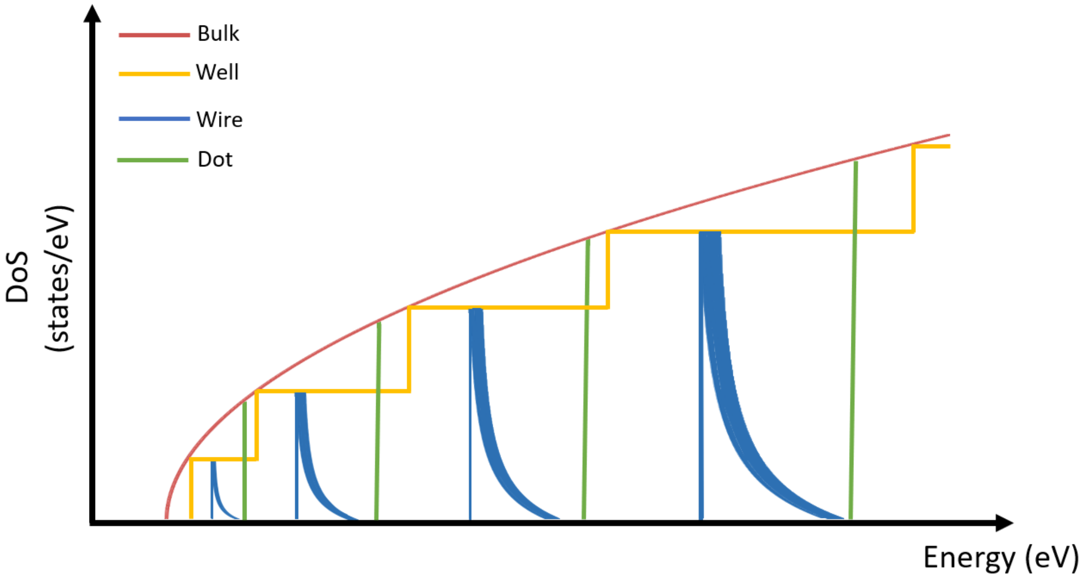

Figure 1.1: **Density of states for the four different dimensions of degrees of freedom** | Each level of confinement, is colour-coded, with the 3D bulk obeying a parabolic function, the 2D well obeying a step function, the 1D wire obeying an inverse energy relation, and the 0D the quantum dot, which sees a series of mono-energetic states available. The exact locations of these curves are not necessarily important, but it is important to note that all energies are bounded by the free energy of the 0D confinement. Excitonic effects and further quantum confinement effects push the energies further, with the first excited QD state starting above all of the others.

the QD can be mapped to a scheme of shell-filling, similar to atomic orbitals whose angular momenta come from the properties of the semiconductor platform.

Within the semiconductor material, excited electrons occupy the conduction band with an s-type wavefunction (due to the atomic orbitals inside the material) and the resultant holes occupy the valence band with a p-type wavefunction, with each band separated by an energetically-inaccessible region called a band gap.

Associated with these energy positions inside the semiconductor, the s- and p- carrier orbitals have respective angular momentum values of $l = 0$ and $l = 1$. The $l = 0$ state carries only the sub-state $m_l = 0$ but the $l = 1$ state carries the two sub-states of $m_l = -1$ and $m_l = 1$ [1]. The electron and hole carry a *spin* of $s = 1/2$ (with $m_s = \pm 1/2$) which, when combined with the angular momentum states, provides a number of total angular momentum projections: $m_j = -3/2, -1/2, +1/2, +3/2$ for the $l = 1$ state, and $m_j = \pm 1/2$ for the $l = 0$.

The $m_j = \pm 1/2$ projections for the $l = 1$ contribution refer to the split-off band, which is usually ignored in this work due to the large energy offset between itself and the energy locations for the (usually degenerate, for bulk systems with no strain) heavy- and light- hole bands. The heavy hole and light hole bands, pertaining to the remaining $\pm 3/2$ (of the $l = 1$ state) and $\pm 1/2$ (of the $l = 0$) sub-states respectively, also see a splitting due to confinement asymmetries between the in-plane (X/Y) and growth (Z) directions, which arise during the growth process of most QDs, even though they are symmetric at the Γ point in bulk semiconductor materials. The resulting picture, as shown in figure 1.2, is one where electrons are occupying the conduction band and only the heavy hole states in the valence band are the carrier states of concern. Since the split-off states are not considered, the only states for consideration are the light and heavy holes. Thus, the picture becomes that of the four $m_j = \pm 3/2$ (heavy hole) and $\pm 1/2$ (light hole) states. The circumstances can be simplified even further consideration of the via the interaction between single photons.

---

[1] The m_l=0 substate does not exist in the QD due to confinement asymmetries induced by the vertical confinement, breaking the perfect spherical symmetry.

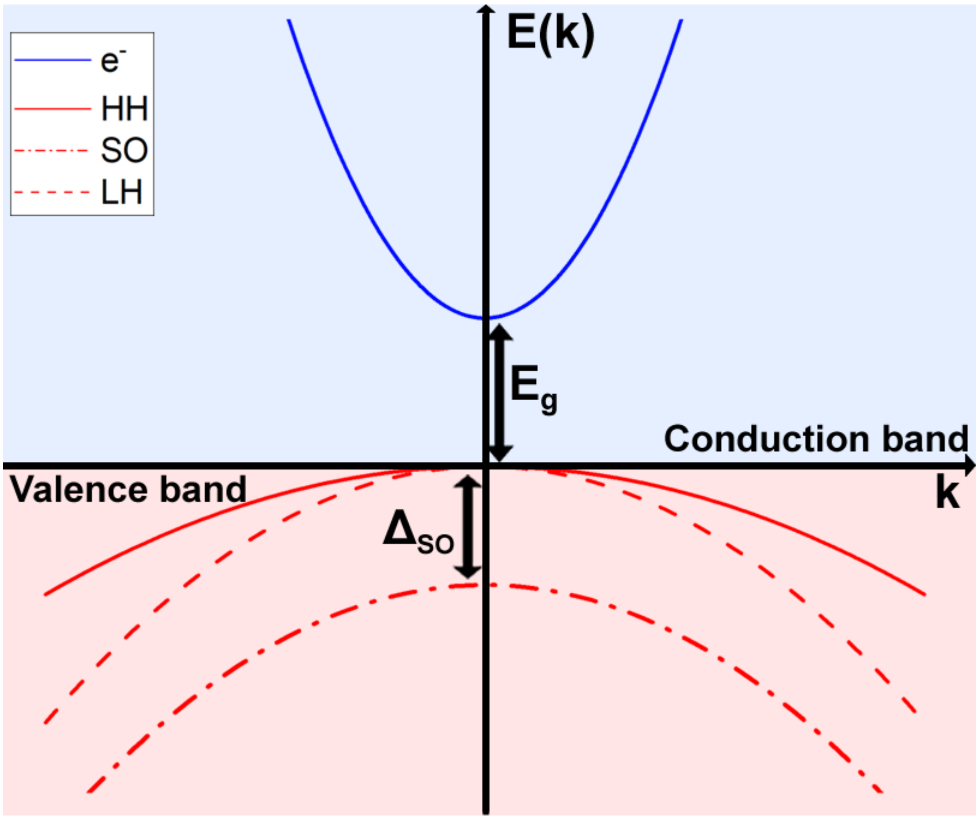

Figure 1.2: **Carrier band diagram for direct-gap bulk semiconductors** | At zero crystal strain, the light (dashed red) and heavy (solid red) holes are degenerate. The split off (SO - dot/dash line) band exists at zero strain because of the spin-orbit coupling. The parabolic shape is only an approximation for small k values [54, 55]

Usual considerations of a quantum dot only include up to four carriers inside at any one time, each carrier being in the first excited state, abiding by rules similar to standard atomic shell filling, whereby each type of carrier exists in spin (up/down) pairs. Further carriers would require larger energies to occupy “higher” shells, beyond the first excited states present for the electron and holes. Carriers quickly relax into the ground states through phonon relaxation processes. In the simplest case, the QD is occupied by a single electron and single (heavy) hole, each with a random alignment of their spins (ignoring the case where specific spins are generated through exciting with circularly polarised light, as phonon relaxations should preserve spin).

Excluding the energy from any Coulombic interaction (and thus eliminating the exchange interaction responsible for a fine structure splitting), one can consider the ideal case of circular emission. Here, the angular momentum carried by the circular polarisation of the photon originates from the total angular momentum of the excitonic complex inside the QD, but only for the two states whose combined angular momentum is ±1. The sub-states of the heavy hole ($m_{j,H} = -3/2$, and $3/2$) combine with the sub-states of the electron ($m_{j,e} = -1/2$ and $1/2$) to form the excitonic angular momentum states of $m_{ex} = -2, -1, 1,$ and 2. Since the photon only has unity angular momentum, only the $m_{ex} = \pm 1$ exciton sub-states can couple to the photon field. These are known as bright excitons.

The $m_{ex} = 2$ sub-states are known as dark exctions, since they cannot traditionally recombine through interaction with the light field. Although this effect is not studied in detail in this thesis, confinement asymmetries can cause state mixing between the light and dark excitons allowing these so-called optically forbidden transitions to take place. The resulting emission from the neutral exciton, X^0, has a linear polarisation (which can become circular when a magnetic field is applied and the Zeeman energies are larger than the intermixing energies), having some impact on the chiral effects studied in this thesis. Following the neutral exciton, the QD state with three carriers is considered. In this circumstance, either an additional electron (to form the negative trion, X^-) or an additional hole (to form the positive trion, X^+) occupies the QD along with the initial exciton. The duplicate carriers form an up-down spin pair, with the Pauli exclusion principle preventing the same spin for the same energy between the charge pair, and the lone electron or hole possesses a random spin. Upon recombination, the same momentum conservation rules apply, only in the charged cases, a lone spin (of $1/2$ or $3/2$) is left behind. Many directions of work utilise the lone electron spin or the lone hole spin stored within the QD, with different advantages for each. A simple level diagram is shown in figure 1.3 which shows the neutral and trion sates.

The final QD state often considered is the biexciton state, XX. The ground state consists of a fully-occupied s-shell of two electrons and two holes. Similar to the neutral QD, no net spin is present in the QD at any time, but recombination of suitable (optically allowed) e-h pairs results in the usual emission of linearly (cross)

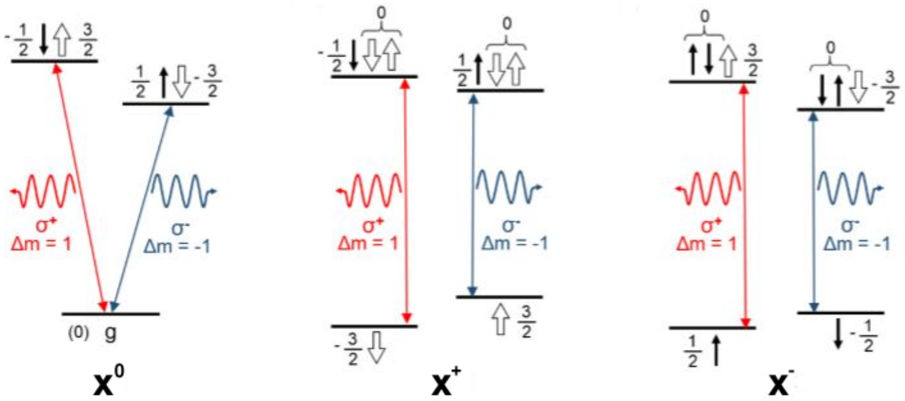

Figure 1.3: **Level diagram for the neutral X^0 and singly-charged exciton states $X^{+/-}$** | A magnetic field splits all three states, lifting the degeneracy of the spin ground states of the charged exciton, and overcoming the exchange splitting from the neutral exciton to restore the circular polarisation of the transitions. Circularly polarised photons carry the momentum between excited and ground states.

polarised photons. If the two transitions are symmetrically coupled to any waveguide or free space mode (i.e. the two linear polarisations have equal probability of being emitted in the same direction), these two photos are entangled. This is to say that their which-path information erasure can result in the entanglement of the cascading emission of the biexciton state to the ground (empty) state of the QD. P-shell (or higher) excitations of the biexciton are not discussed in this thesis.

1.5 On-chip Integration of Single Photon Emitters

The quantum dots presented in this thesis are randomly grown, Stranski-Krastanov (SK) QDs [56]. Such emitters are robust to small changes in temperature (a few K, up to around 10K where their coherence properties begin to falter [57], with linewidths almost unusable at 50K [58]) and thermal cycling and can maintain their emissive properties over long periods of time. One of the most useful features, however, is the ability for QDs to be integrated easily into semiconductor structures for a variety of benefits.

Non-semiconductor sources of single photons (e.g. SPDC), amongst other issues, suffer from the disadvantage of usually having a large surface footprint, as well as not being as on-demand in their emission, with only a few exceptions, such as electrically-driven emission of SiC or diamond colour centres [59]. Other architectures, such as the on-chip integration of an single photon source on a $LiNbO_3$ waveguide [60], require hybridising with the semiconductor platform. Moreover, many non-semiconductor sources require single phonon non-linearities, and therefore require large amounts of input power to produce viable numbers of single photons [61] Therefore, the production of a fully-functional quantum information processor may require large working areas and many copies of multiple physical components in macroscopic experimental setups (e.g. mirrors), which often require constant monitoring. In principle, on-chip integrated emitters provide microscopic platforms, which have shown much promise in the way of on-demand source production, tuneability, a platform for state manipulation and, subsequently, entanglement. Moreover, the architectures surrounding these sources (QDs) offer more than passive operations such as guiding and routing, but allow for cavity enhancement (Purcell enhancement) to to shorten emitter lifetimes and effectively overcome decoherence processes. Additionally, specific architectures allow for basic QIP requirements such as arbitrary phase shifts to optical paths [62] (through the application of heat, for example) as well as allowing designs for beam splitters, interferometers or directional couplers.

1.5.1 The DiVincenzo Criteria

The DiVincenzo criteria [17] are a collection of five (plus two) criteria which lay a foundational series of requirements for anyone desiring to produce a gate-based QIP system. Whilst there have been expansions to the criteria below to more generally include other paradigms such as cluster state manipulation in global control systems, universal gate circuit models, or measurement-based computing, the original criteria are still satisfactory for many facets of quantum information processing. Importantly, each criterion can be mapped to the favourable characteristics presented by the semiconductor, on-chip platform with integrated QDs. The interplay between QDs and different photonic architectures can, in principle, easily satisfy the following criteria.

The DiVincenzo criteria can be summarised as the following:

1. A scalable physical system with well characterized qubits
2. The ability to initialize the state of the qubits to a simple fiducial state, such as $|000...\rangle$
3. Long, relevant, decoherence times; much longer than the gate operation time
4. A "universal" set of quantum gates
5. A qubit-specific measurement capability

with the "plus two" requirements being:

1. The ability to interconvert stationary and flying qubits
2. The ability to faithfully transmit flying qubits between specified locations

Scalability, as one of the most important of all the criteria here, portrays an image of arrays of sources and devices to manipulate the states of the source. In the example of integrated QDs, a series of (possibly connected) etched devices can be imagined. While devices can be reproduced with repeatable efficacy, ensuring sources are contained within each device location is currently non-trivial. For quantum dots, whose first populated state can be considered as a two level system, and hence are "well-characterised," the first challenge/criterion is simultaneously easily solvable and yet difficult to effectively achieve if one wishes to utilise the best source quality. Currently, the best QD production relies on the random SK growth process, in which the locations, the energy distributions and spectral widths of the dots are randomly distributed. This randomness is inherently unscalable, whereby patterned arrays of photonic structures will not contain identical QDs in ideal locations. There are a few solutions currently within the scope of III-V photonics that aim to control the two most important things a QD needs to control over in the QIP space: its position in the device and the emission wavelength.

One avenue is to register the locations of QDs [63, 64]. By marking (through high-precision direct imaging or dead-reckoning through intensity optimisation) the locations of QDs relative to a series of alignment markers, it is possible to fabricate photonic structures deterministically to 10nm accuracy around the registered emitter locations. This has been performed to generate devices with emitters which sit at ideal locations (to experimental error, which can be up to 30nm) inside a photonic structure to promote certain interactions [65] (such as superradiant emission or Purcell enhancement).

Site-control of quantum dots has seen much interest over the years as a means to deterministically encourage QD growth in specified locations. Naturally, an array of QDs in specific locations allows simple device etching around these sites. However, site-control technology is not as mature as SK random growth in terms of the individual emitter quality. Such dots suffer from natural line broadening under cryogenic conditions due to patterning imperfections or the presence of impurities [66]. Additionally, multiple QDs can form at the specified locations which can introduce unfavourable strain effects, further increasing the already-broad spectral lineshapes, as well as potentially generating two photons if the second QD is optically active. It can be said, therefore, that the two best options are: register the QD location using SK QDs and fabricate the devices around them, or, allow the site-control scheme to fully develop and fabricate photonic structures based on the known arrays of emitters. However, site-control growth still has to achieve control over the emission wavelength as well as a reduction in the linewdith of the devices.

Quantum dots, as spin-based qubits, happily fulfil the second criterion as they are very easily initialisable to predictable states. A common initialisation process is achieved via spin pumping, which can be performed through a variety of means, either on lone QDs in bulk, or QDs integrated into a photonic device. Spin pumping through weakly-allowed transitions is covered in chapter 6. In addition to being easily initalisable, QD states have been shown to be easily manipulable across the whole Bloch sphere, through means such as electron spin resonance (ESR) and ultrafast optical pulses. Full coherent control of an exciton state inside the QD has been shown to be possible [67–69]. Given that it has been shown that one only needs one- and two- qubit logic gates (the QD states) to achieve full expression of all unitary operations on large numbers of bits, QDs can be said to satisfy the fourth of the DiVincenzo criteria.

Thus far, quantum dots have been described as potentially scalable, readily initialisable, and manipulable as parts of gates. However, a QD is only manipulable if the information is stored for long enough for an operation to carried out on the pure state. Decoherence affects all quantum systems, and works to wash away the purity of quantum states. In semiconductors, a variety of sources for decoherence are present such as phonon relaxations and charge noise from the environment. Importantly, the conversion of the pure state into the mixed state from environmental interactions poses an upper bound to many things. Information storage time being limited provides a cap on the number of operations that could be applied, but also imposes limitations on the time that is available for a qubit operation to take place at all after initialisation. In the semiconductor platform, the intrinsic decoherence times vary depending on the specific qubit of choice. There are three fundamental timescales when considering the coherence of a qubit: T_1, T_2 and ${T_2}^*$. Equation 1.1 describes the relationship between them [70].

$$\frac{1}{T_2} = \frac{1}{2T_1} + \frac{1}{{T_2}^*} \tag{1.1}$$

T_1 is associated with a particular type of state decoherence, represented by the population of a state, or the leakage of a state's energy to the environment. In the case of a neutral exciton, for example, T_1 represents a decay constant parametrising the recombination of the e-h pair, i.e. the collapse of $|1\rangle$ to $|0\rangle$. The parameter T_2, known as the transverse decoherence time, phase decoherence time, or even coherence time is a time constant that describes the state's ability to remain coherent, without losing its purity to an external environment. T_2 is a function of the lifetime of the state, T_1 and $T_2{}^*$ (describing pure dephasing, a particular type of decoherence). Pure dephasing describes the external interactions of the QD state (or spin) with the environment through interactions such as nuclear hyperfine interactions with the spin of single electrons and acoustic phonon interactions, and does not explicitly rely on changes in state population.

The final "plus two" requirements of the DiVincenzo criteria are much more specific to the work presented in this thesis, by their reference to the engineering of a quantum network, rather than the fundamental physics. In essence, these two requirements describe the transport of information, manifesting as the conversion of photons to static qubits (e.g. excitons, single electron spins) and the transport of photons throughout the network, whether this is towards detectors or towards other static qubit sites. The primary form of transportation for flying qubits in this work is through nanoscale photonic confinement. The designs featured in this work ensure that not only is the light-matter interaction enhanced, but that the light also travels in desired directions for deterministic guiding. Deterministic transmission or guiding is crucial for on-chip networks to function properly.

1.6 The Importance of Chirality

With the demonstration that QDs integrated into semiconductor photonic structures can satisfy a complete check list for QIP, another concept is presented here which heavily advances some of the particular criteria presented in the previous section.

Outside of the world of quantum optics and photonics, chirality refers to a system's handedness, insofar that an object or shape is considered chiral if the mirror image of the item about any plane is not superimposable upon the original. An often-considered example in chemistry is a chiral molecule, such as a tetrahedral carbon (with four different chemical groups/elements bonded to the central carbon atom). As can be seen in 1.4, when the mirror image of the molecule is taken, no rotation of either version of the molecule can provide a perfect overlap of the two. Such molecules are known as enantiomers.

In the context of quantum optics, chirality manifests itself through the time-reversal symmetry of a transversely-confined electric field, whereby the direction of the light propagation can explicitly depend on the spin of the photonic mode within a waveguide setting [71]. A deeper explanation regarding the origin of chirality via the electromagnetic wave confinement in nanophotonic structures will be provided in chapter 3. Importantly, the intrinsic link between the propagation direction and the spin angular momentum of a confined photon enables complete control of the routing of flying qubits within a network. This directional control, in principle, allows for deterministic routing of information from one static qubit site (such as a QD) to another. Such an emitter which has chiral properties, is said to be chirally coupled to the waveguide.

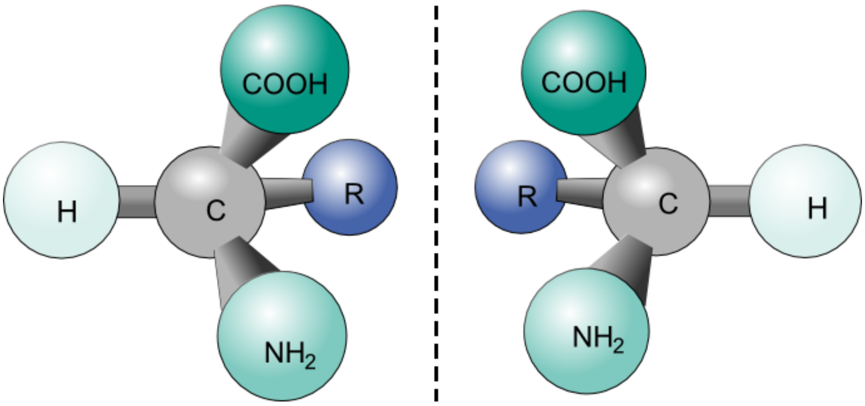

Figure 1.4: **Chiral molecular enantiomer of an amino acid** | This amino acid has a chiral structure, as the reflection about the central dotted line means that the mirror image cannot be aligned with the original image. Choosing any of the individual bonds as an overlap point causes a misalignment in at least one of the other bonds.

The imposed directionality not only allows for complete control in terms of the flow of light within a network, but also allows for interesting physics unique to the chiral setting. For example, the case of two chirally coupled emitters, a cascade of emission can result in the interesting case of superradiance, but allowing for the generation of unique quantum dimers [72]. Moreover, chirally integrated emitters can act as single photon switches, whereby photonic absorption can be directionally dependent, extending to the possibility of redirecting light off-chip at the location of the emitter if certain requirements can be met. It is even possible for single emitters to impart a phase shift to single photons that are resonantly coupled to a chiral emitter, in both a cavity setting [73] (which has been successfully demonstrated) and the waveguide setting [74].

1.7 Enhancement of Light-Matter Interactions

As discussed in subsection 1.2, the interaction strength of two photons being zero summons a necessity of a mediator to ensure interaction beyond the entangling inseparability of the Hong-Ou-Mandel effect. In all of this work, a quantum emitter (QD) is considered inside a waveguiding structure. This principle can be explained in the regime of weak cavity coupling, where light may travel inside the cavity with only small resonances between the allowed energies of lifting the cavity's band gap and the emitter's emission energy. Relevant incarnations of a weakly-coupled cavity in III-V systems exist as the 1D photonic crystal, such as the W1 defect photonic crystal. This crystal is discussed in more detail in chapter 3, but the basics of the photonic crystal are discussed here.

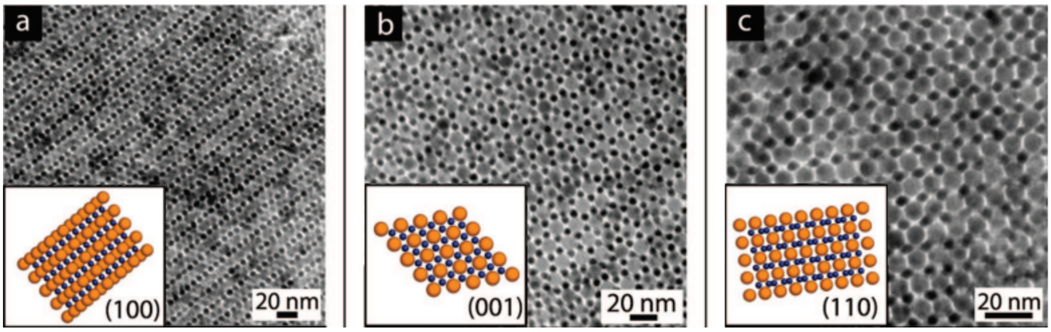

Figure 1.5: **Transmission electron microscopy of a binary super lattice viewed from different crystallographic planes** | Each viewing plane is presented in the inset of the various TEMs. The periodic nature of the CaF_2-style structure is clearly present in all three images. Images from [75].

1.7.1 Photonic Crystals

In condensed matter physics, a crystal is considered to be a material whose basic building block constituents are placed in a periodic manner, such as atoms arranged in solid metals. On a nanoscopic scale, the atomic arrangement can be mapped either through crystallographic methods [76] or through scanning electron microscopy (SEM) [77]. Figure 1.5 shows SEM images of an AB_2 binary superlattice when viewed from different crystal plane directions. In solid state physics, this periodicity summons very useful physics for the on-chip platform, allowing for the generation of cavities and passive structures like waveguides. Generally, the photonic crystal is the periodic arrangement of (dielectric) material in any number of the three dimensions. The existence of this arrangement generates a range of energies which light cannot posses within the crystal. This inaccessible region is known as the photonic band gap, and it is analogous to the electronic band gap in semiconductor materials. In order to appreciate the benefits of basic photonic crystal concepts, the one-dimensional photonic crystal is the simplest crystal to consider, and a depiction is presented in figure 1.6. A single row of holes (of size **d** and periodicity **a**) is etched within the material, with the exception that one hole is missing from the etching pattern, leaving a gap of marked size **S**. Figure 1.6 shows how the removal of a random hole within a (semi-)infinite crystal allows for the existence of photons within one spectral range. This particular example represents a photonic crystal cavity, where an emitter may only emit light into the crystal if its emission energy matches the small region where the band gap is lifted. Light may not propagate along the length of the crystal as the etched holes continue to act as a filter, with a restored bandgap.

Light generated within the cavity, or the crystal waveguide, interacts with the photonic environment depending on the level of coupling between the emitter and the cavity. There are two regimes considered in the cases of the different coupling strengths: strong and weak coupling .

Strong Coupling - Cavity Quantum Electrodynamics (cQED)

The interaction between an emitter and a cavity is often characterised by a few parameters associated with the properties of the emitter and the cavity. Namely, a

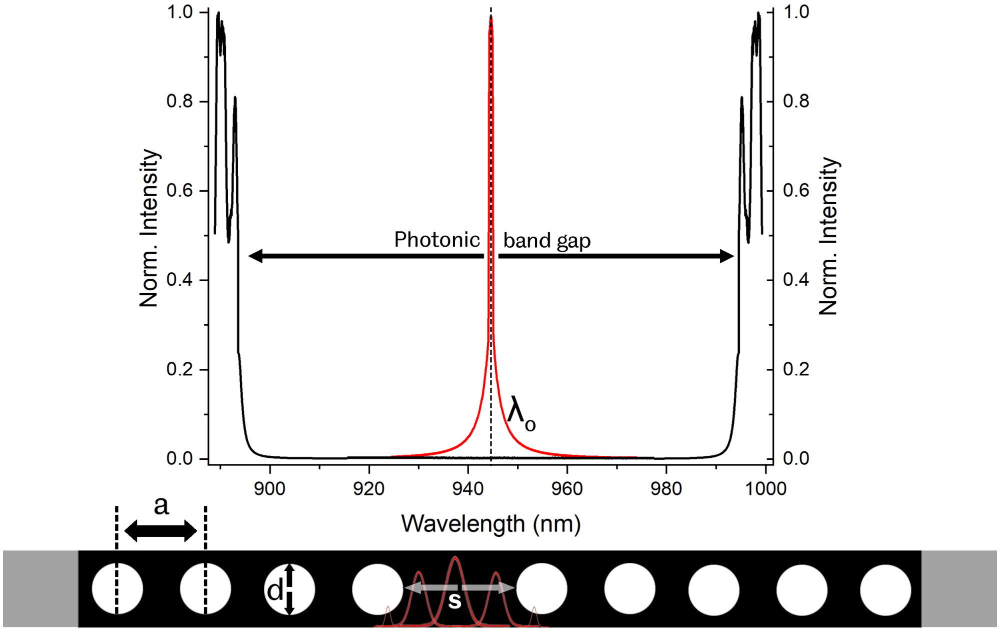

Figure 1.6: **1D photonic crystal cavity with a single hole defect, and the corresponding transmission band structure, showing a photonic band gap and the allowed mode at wavelength λ_0** | The 1D crystal has a period, a, of hole sizes, d. S is the cavity's main region. Transmitted light drops to effectively zero intensity at a particular wavelength, depending on the periodicity and the size of the holes. The allowed mode (red curve) of the photonic crystal, because of the defect, would be a single, dirac delta in principle, but unavoidable hole shape and period imperfections allow for a broadening of this mode. The size of the gap, **s** determines the spectral position of the cavity (allowed) mode.

coupling strength g_{sc}, the emission rate of the emitter inside the cavity, Γ, a rate of leakage of the cavity mode (which has a volume, V) into the external environment, κ, where the cavity has resonance, ω_0, and a spectral width of $\Delta\omega$. In the strong coupling regime, the coupling rate, g_{sc} is said to $\gg (\Gamma, \kappa)$. A figure of merit describing the effectiveness of the cavity is known as the quality factor, which relates the spectral width and its central frequency thusly: $Q = \frac{\omega_0}{\Delta\omega}$. The extrapolation of this expression implies the most optimum cavity is of exceedingly narrow spectral width. For the solid state platform, achievable confinements can be between visible (∼450nm [78]) wavelengths and the mid-IR telecomms 1.55μm [79] range, with some cavities achieving a theoretical Q of 1800 at 1562nm [80] for the silicon platform, and Q up to 11,000 for a SiN platform at slightly longer wavelengths [81]. It is possible, even, to drastically advance the quality factor to values of the order of 10^5, for III-V systems at 930nm [82].

Strong coupling, in the context of cavity work, explains a relative paradigm whereby an emitter and the surrounding cavity are strongly interlinked. The dynamics of a simplistic system describes the coherent interplay between the populations of the solid state two level system and photons within the cavity. Such conditions form polaritons, a hybridised quasi-state of matter beholding the bosonic nature of the photon in certain conditions (such as forming a Bose-Einstein condensate [83, 84]), with the fermionic capacity for Pauli exclusion (blocking) in another regime, and maintaining the ability for strong interactions with light [85]. In cavity quantum electrodynamics (cQED), the physics describing the interaction between a two level system and the cavity is covered mostly by the Jaynes-Cummings ladder [86]. In this system, an overall Hamiltonian is derived by proposing the consideration of three physical components:

- the energy of the electromagnetic field within the cavity - each photon emitted into the cavity provides additional energy to the Hamiltonian
- the energy of the two level system - the excited state of the qubit contributes one quantum of energy, which may differ depending on the inclusion of the third term
- the interaction between the cavity and the two level system - this is quantified by the parameter g_{sc}

The combination of all three components manifest in the Jaynes-Cummings Hamiltonian,

$$H_{JC} = \omega_{Cav}\sigma_{+}\sigma_{-} + \omega_{2LS}a^{\dagger}a + g(a^{\dagger}\sigma_{-} + a\sigma_{+}) \tag{1.2}$$

where ω_{2LS}, ω_{Cav} represent the energies of the qubit or cavity photon respectively. The $a^{\dagger}$ and a terms represent the creation and annihilation operators for the photons, and the σ_{+} and σ_{-} terms are the raising and lowering operators for the full ladder system. The strong coupling regime is only of relevant consideration for cavities which confine light strongly over a small volume. For the work featured in this thesis, the more relevant regime is weak coupling, seen below.

1.7.2 The Purcell Effect - Weak Coupling

Opposite to the case for strong coupling, interactions between the cavity and the emitter are not as prevalent, and cavity leakage dominates the system, providing the opposite condition of: $g_{sc} \ll (\Gamma, \kappa)$. In these systems, the quality factor divided by the mode volume is less of an indicator as to the functionality of the coupling between the emitter and the cavity. Instead, the primary method of characterising the enhancement is not through the consideration of polaritonic hybrids, but instead through a parameter known as the Purcell factor. The Purcell effect describes the enhanced spontaneous emission rate relative to the brightness of the emitter outside of the enhancing environment. In the context of cavities, a Purcell enhancement of an emitter weakly coupled to a cavity mode which contains an electromagnetic wave, with a vacuum wavelength, λ, inside a material of refractive index, n, which restricts the wave to a volume, V_{eff} with a resonator quality factor, Q, can be expressed as is in equation 1.3.

$$F_p = \left(\frac{3}{4\pi^2}\right)\left(\frac{\lambda}{n}\right)^3\left(\frac{Q}{V_{eff}}\right) \tag{1.3}$$

The formulation of this equation is more appropriate to an emitter coupled to a 0D cavity-like environment. When light is able to transmit along the longitudinal axis of the defect, the parameters are somewhat different. Passive structures, like the W1 defect PhC, or even a suspended nanobeam waveguide should be investigated under a different perspective. For example, one should consider the interplay between the quality factor and the waveguiding properties of the system, as an infinitely large quality factor leads to perfect confinement and thus no energy flow at all. This is to say that the quality factor is a representative measure of the energy losses in the emitter's locale. If the purpose of a 2D crystal is to allow for the transmission of light, a compromise is needed to ensure that the crystal has broadband operation while still providing enhancement effects.

The concept for photonic confinement in two dimensions is very similar, whereby a linear defect (such as removing a row of holes in a triangular lattice) to the crystal shape results in a continuous allowed mode (rather than a sharp peak within the photonic band gap) with a spectrum capped by two boundaries. Such a spectrum creates an environment capable of transmitting wavelengths which the cavity or waveguide may permit, meaning that the system can act as a spectral filter, suppressing unwanted energies in an on-chip architecture. Section 5.3 will specifically detail how the spectral location of the emitter can change the effective the spontaneous emission rate.

A more intuitive iteration of equation 1.3 is presented in equation 1.4, as seen in reference [87].

$$F_p = \left(\frac{3\pi c^2 a}{\sqrt{\epsilon_r}}\right)\left(\frac{|\mathbf{e}_{k_\omega} \cdot \hat{\mathbf{n}}|^2}{\omega_d^2}\right)(n_g(\omega)) \tag{1.4}$$

The mode is confined to a photonic crystal of period a, and relative permittivity ϵ_r, and experiences a relative (wavelength-dependent) slow-down factor which alters the group velocity to a speed v_g, from the vacuum speed of light, c. The emitter releasing the wave packet, which has a Bloch mode $e_{k,\omega}$ of frequency ω_d, has a dipole vector pointed along the direction of the unit vector $\hat{\mathbf{n}}$.

The insight of this equation can be seen when studying Fermi's golden rule. Traditionally, Fermi's golden rule applies to a state which can potentially couple to a pseudo-continuum of states [88, 89]. Therefore, while having no apparent relevance to a normal static emitter sitting in a cavity that merely supports ideally one frequency, the coupling of such an emitter to the broadband range of available photonic states with a PhC waveguide more faithfully matches the intention of the golden rule. Physically, the golden rule describes the transition rate between two quantum states (like the ground and the excited state of a two level system), and it is a function of the density of states of the continuum and a (modulus square of a) matrix element representing the interaction strength between the initial and final states of the QD inside the waveguide, encoding within a single-photon interaction probability, which can translate as the beta factor [2].

---

[2] The beta factor is described in section 3.1 of chapter 3, but can be summarised as the probability a photon is generated inside a valid waveguide mode when the emitter de-excites. See eqn. 1.9

Fermi's golden rule is presented in equation 1.5, depicting a generic two level system, with initial (ground) state $\langle i|$, and final (excited) state $|f\rangle$, perturbed by an external Hamiltonain, $\mathcal{H}'$ (which could be an excited waveguide mode, or simple vacuum fluctuations). The density of states, $\rho(E_f)$, for a waveguide, relates to the dispersion of the waveguide and the mode profile of the electric field within. For a larger field intensity at certain locations within the waveguide, the density of states is also larger.

$$\Gamma_{if} = \frac{2\pi}{\hbar} \left|\langle i|\mathcal{H}'|f\rangle\right|^2 \rho(E_f) \tag{1.5}$$

It is possible to generate an expression for the spontaneous emission rate of an emitter in a waveguide by using the Purcell enhancement equation (eqn 1.4) and the standard expression for the spontaneous emission rate of an emitter in free space. N. Takahiro finds this expression to be:

$$\Gamma_{sp,free} = \frac{4\omega^3|\mu|^2}{3\hbar c^3} \tag{1.6}$$

By using this expression, and multiplying it with the expression for the Purcell enhancement, one arrives with:

$$\Gamma_{\text{sp, WG}} = \frac{4\pi a}{\hbar c\sqrt{\epsilon_r}} |\mu|^2 \left|\mathbf{e}_{\mathbf{k},\omega} \cdot \hat{\mathbf{n}}\right|^2 \omega_d \, n_g(\omega_d) \tag{1.7}$$

where μ represents the dipole moment of the emitter (when it was in free space) and n$_g$ represents the refractive index as a function of ω_d. By combining the dipole moment magnitude and the unit vector of this dipole, and writing the expression in terms of equation 1.5, an expression for the spontaneous emission rate in a waveguide is provided:

$$\Gamma_{sp,WG} = \frac{2\pi}{\hbar} \left|\mathbf{e}_{\mathbf{k},\omega} \cdot \mu\right|^2 \left(\frac{2}{c} \frac{a}{\sqrt{\epsilon_r}}\right) \omega_d \, n_g(\omega_d) \tag{1.8}$$

In this format, the density of states encapsulates constants: 2/c, $a/\sqrt{\epsilon_r}$, a factor that often appears in dispersion engineering encapsulating the hole size and the material of which the crystal is comprised, and an expression relating to the emission frequency and the crystal's dispersion. The expression of $|\mathbf{e}_{\mathbf{k},\omega} \cdot \mu|^2$ can be seen to reflect the transition rate, as it directly represents the coupling of the excited state of the emitter and the continuum of states represented by the waveguide Bloch modes.

1.7.3 Waveguide Coupling - The Beta Factor

The beta factor, β, describes the coupling strength of an emitter to the desired guided mode of the waveguide. β is defined as:

$$\beta = \frac{\gamma}{\gamma + \Gamma_{loss}} \tag{1.9}$$

where γ refers to the emission rate of photons into the desired waveguide modes, and Γ_{loss} represents leakage of the emission into undesired modes. The losses represented by Γ_{loss} mainly refer to QD emission that does not couple to the waveguide at all, often seen as light emitted directly above the QD. For ideal QIP application, this is undesirable, but experimentally it is very useful in order to deduce the location of a QD along the length of the device if it is not known beforehand, as would be the case in a registration scheme. Γ_{loss} can also account for undesired mode coupling from contributions from QD recombination into the "dark" exciton states.

There are a few ways of experimentally measuring the β factor of an emitter within a waveguide. One method is through attempting to physically measure the ratios of light emitted vertically out of a photonic crystal directly above the emitter and the light leaving through output ports on the device. This method can be performed non-resonantly, and it is therefore more experimentally accessible.

A second method to measuring the β factor is through single photon scattering measurements. The consideration of a two level system within a waveguide is the simplest, summoning the physics of the input-output formalism, as described in detail in [90]. Figure 1.7 depicts this system, with an input photon which has a probability of being transmitted, reflected, or totally redirected out of the waveguide mode. The important result, as outlined in [91], [92] and the supplementary of [93] (eqn. S20, setting $\beta_d = 1$ and $\tilde{\gamma}$ to 0), is that the transmission is dependant on the beta factor, as outlined by equation 1.10, showing how the transmission, T, depends on the beta factor, β, the detuning between the transition energy $\hbar\omega$ and an input photon, and the radiative emission rate, Γ.

$$T(\omega) = \left| 1 - \frac{\beta}{1 - i(\Delta E(\omega)/\Gamma)} \right|^2 \tag{1.10}$$

The importance of this expression rests in the directly-calculable relation between the transmission and the beta factor. For a resonant interaction, with a very short lifetime (as characterised by a large Γ), the transmission tends to 0 for a unity β. The intuition, therefore, is that single photons are reflected from a perfectly-coupled emitter in a normal, non-chiral waveguide. The functional form of this expression becomes more complicated when considering the dynamics of the emitter's energy and weak cavity behaviour described by the Fano effect which arises from interface reflections.

This method is not explored within this thesis for a few reasons, but the final expression, including parameters such as dephasing times, spectral wandering, and even directionality can be summoned. D. Hurst demonstrates this in both [92] and [93].

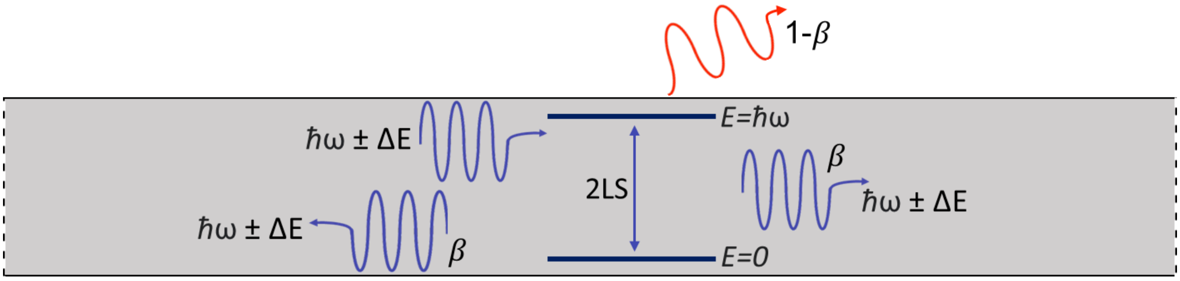

Figure 1.7: **A waveguide coupled to a 2LS depicting the consequence of a β factor** | A single photon propagating along the waveguide, from the left, interacts with the two level system, whose resonant energy is $\hbar\omega$. Light is either, in principle, reflected, or transmitted, or lost from the waveguide through the factor of 1-β. The reflection or transmission should occur with the rate of β. The addition of $\pm\Delta$E accounts for the possibility of off-resonant interactions between the light and the emitter.

As a final note on this second process, it is important to note that, as explored in [94], a perfectly chiral emitter presents perfect transmission of single photons, if the input laser is weak enough to include only very small contributions of higher photons numbers in its coherent field. Without deep knowledge of parameters at comparable significant figures, it can be difficult to experimentally determine which attributes of the emitter are contributing to the transmitted intensity, without being able to directly measure the phase. Directly measuring the phase is speculated in the further work chapter of this thesis, but has been performed in other systems, such as the one which appears in ref [95].

Chapter 2

Sample Fabrication and Experimental Methods

This chapter will describe the process behind the fabrication of the devices used in this research. First, the basic process of the wafer design will be described for the p-i-n style of layering, which will follow a description of the specific pattern designs that give rise to the relevant physics studied in this thesis. This will follow an explanation for the growth of quantum dots used in this experiment, before coming back to a more detailed explanation of the specific wafer growth relevant to this work.

After the discussion of fabrication, a description and explanation of the experimental set-up(s) used to analyse the fabricated devices will be given for each of the types of experiments that were performed. Namely, these types will be split into resonant and non-resonant schemes, even though both categories share many similarities owing to the use of the same optical table and cryogenic chamber. Simulation data will be included in chapter 3.6, where the nature of the specific devices and their architectures used in this work are explained.

All wafers used were grown by E. Clarke et al at Sheffield's III-V centre, and the fabrication and SEM was managed by B. Royall (LDSD), R. Dost (LDSD) or P. Haines (III-V centre). I was personally present for most of the post-growth fabrication of the wafers used in chapters 4 and 5.

2.1 Growth of III-V InGaAs QDs on (Al)GaAs wafers

The heterostructures featured within this work are grown with the purpose of gaining electrical control of quantum dots. This is achieved by growing a QD layer between two doped regions of GaAs which comprise a p- contact and an n- contact. Here, an explanation of the growth process for quantum dots is provided, along with a brief detail of the generation of the p-i-n heterostructure. Another expansion of the p-i-n, known as the p-i-n-i-n is discussed later in section 6.2 of chapter 6, as there are particular advantages to that design, even though it was not fabricated in Sheffield. Molecular beam epitaxy (MBE) was used for all samples discussed. Figure 2.1 depicts a layering structure for one the devices used in these experiments, ideally comprising a p-i-n.

The general structures are always similar, featuring a layer of undoped GaAs, surrounding a narrow InAs layer (where the QDs form) sandwiched by a top cap of p- doped GaAs and a bottom layer of n- doped GaAs. Both the doped layers eventu-

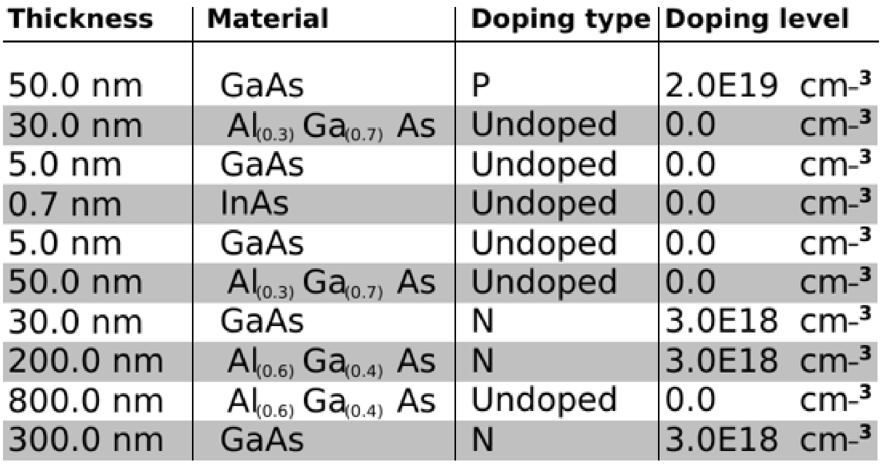

Thickness	Material	Doping type	Doping level
50.0 nm	GaAs	P	2.0E19 cm^{-3}
30.0 nm	$Al_{(0.3)}Ga_{(0.7)}As$	Undoped	0.0 cm^{-3}
5.0 nm	GaAs	Undoped	0.0 cm^{-3}
0.7 nm	InAs	Undoped	0.0 cm^{-3}
5.0 nm	GaAs	Undoped	0.0 cm^{-3}
50.0 nm	$Al_{(0.3)}Ga_{(0.7)}As$	Undoped	0.0 cm^{-3}
30.0 nm	GaAs	N	3.0E18 cm^{-3}
200.0 nm	$Al_{(0.6)}Ga_{(0.4)}As$	N	3.0E18 cm^{-3}
800.0 nm	$Al_{(0.6)}Ga_{(0.4)}As$	Undoped	0.0 cm^{-3}
300.0 nm	GaAs	N	3.0E18 cm^{-3}

Figure 2.1: **Layering of p-i-n heterostructure wafer** | Doping is achieved for the p- and n- layers by Beryllium and Silicon doping respectively. The QD layer is the 0.7nm InAs layer, and the top p- and bottom n- layers are connected to Ti/Au contacts.

ally see a gold/nickel coverage for subsequent electrical contacting towards the end of the fabrication process. All molecular deposition is performed in an ultra high vacuum environment unlike Metal Organic Vapour Phase Epitaxy - MOVPE [96] - or Metal Organic Chemical Vapour Deposition - MOCVD - which rely on higher pressure environments inside a chemical reaction chamber rather than molecular adsorption.

MBE relies on the sublimation of pure elements stored within isolated chambers or cells. Heated cells eject the pure material (e.g. Gallium) as a "beam" onto a substrate surface (also heated), and the combination of different elements produces a monolithic, epitaxial growth of the desired compound (e.g. Gallium Arsenide). The low temperature, low pressure environment of MBE is necessary to ensure the highest levels of material purity. Quantum Dots are grown (for this work) using the Stranski-Krastanov method by utilising the minimisation of strain energy generated when InAs molecules meet a layer of GaAs.

During the epitaxial deposition of the InAs, strain energy is accumulated due to the $\sim 7\%$ mismatch in lattice constants between InAs (6.0583Å) and GaAs (5.653Å) [97]. Eventually, the system naturally seeks to minimise this strain energy and does so via the formation of QD islands, described by the Asaro-Tiller-Grinfield instability [98]. As more InAs is deposited on the GaAs surface, a build of up strain energy eventually maximises to a corresponding critical thickness, at which point the QDs form as small islands across the surface of the substrate. This is depicted in figure 2.2. The nucleated islands sit atop a thin layer of InAs, known as the wetting layer (WL), which effectively acts as a quantum well. During this growth process, the InAs QDs are capped with another layer of GaAs to preserve the optical quality

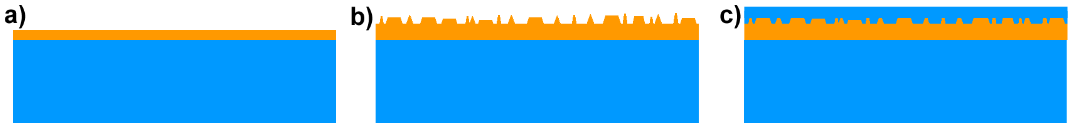

Figure 2.2: **QD Island formation method** | Deposition of InAs (yellow) creates a strain mismatch. After a certain amount of material has been deposited in stage (a), stage (b) island formation occurs. The InAs QDs are topped with more (blue) GaAs as seen in (c), which does admix with the InAs slightly.

of the QDs, and to improve optical confinement by having a thicker material layer between the surface and the QD layer. However, the resulting admixture of GaAs and pure InAs can influence more volatile properties of QD physics, such as nuclear spin interactions [99].

The result is a series of randomly positioned, hemispherical QDs of a potential diameter between 5nm and 30nm (and a height that is usually at least half of the diameter) with an emission range between 850nm and 1000nm. Figure shows a distribution of QD energies for a QD wafer used in the work presented in this thesis. 2.3

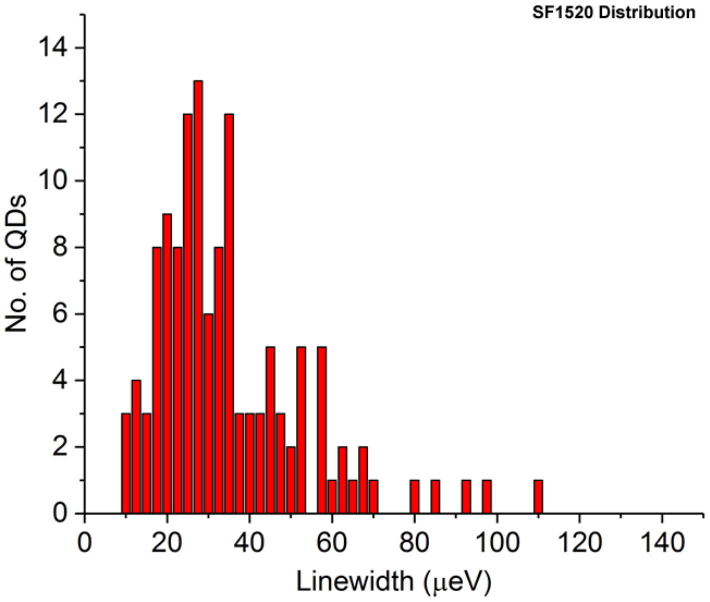

Figure 2.3: **Linewidth distribution of random but bright QDs on a sample** | A sample denoted "SF1520." A diode contact is fabricated without nanophotonic devices to study individual QDs. Low power micro-photoluminescence is used to collect these individual QD lines. A skewed normal distribution provides a 34.8μeV mean over the 128 QD lines studied.

2.2 Device Fabrication on Monolithic Heterostructures

This section will illustrate the full layered structure of a typical "sample" used in this thesis, and will move on to explaining how the photonic devices are finalised, terminating with the metallic deposition for electrical contacting.

In this work, a smooth layer of 200nm GaAs provides the base for the wafer structure. On top of this is an $Al_{(0.6)}Ga_{(0.4)}As$ sacrificial layer of 1.2μm. The importance of this layer arrives during the etching process, discussed later in this section. Atop the $Al_{(0.6)}Ga_{(0.4)}As$ layer sits a series of GaAs layers (including the InAs QD layer, which is comparatively very thin) that effectively make up a p-i-n structure. The purpose of this structure is explained in detail in section 2.5. The p-i-n is comprised of an n- doped $Al_{(0.6)}Ga_{(0.4)}As$ layer, with an additional n-doped GaAs layer. An undoped (or intrinsic) GaAs layer sits directly on top of the n-doped GaAs to serve as the growth plane for the InAs QDs. The QDs are then capped by an additional intrinsic GaAs layer, before being topped with a p-doped GaAs layer. p- and n- doping is achieved by introducing Beryllium and Silicon to the GaAs respectively. The doped GaAs regions allow for electrical control across the sandwiched QD layer, but metallic contacts must be added for this to be possible.

In order to create electrical contacts for QDs, the devices are placed within diode mesas. The fabrication of these electrical contact structures can begin their etching before or after the photonic devices are started, but the diodes need to be finished before the underetch of the photonic devices. This is necessary because the photonic devices are suspended and risk damaging if the finalisation steps of the diode are not first completed. While both etching processes of generating the photonic devices (minus the wet etch step) and generating the diode mesas are similar, the different size scales involved results in slightly different approaches.

The etching of diodes is performed via photolithography. Relative to electron beam lithography (EBL), photolithography is a rapid, coarse process that uses UV light to imprint a pattern into the substrate. For the diodes, solvent-cleaned samples are spin-coated with a drop-cast photoresist (SPR-350). Rapid rotation and application of moderate heat (<100°C) ensures evaporation of residual solvent particulates and a uniform deposition of the photoresist layer. The sample is then placed underneath a pre-manufactured, patterned mask, designed to only transmit UV light through desired regions.

After exposure, the sample is placed in developer (MF26a). The photoresist that has been exposed to the UV is dissolved, and the sample now has a “mask” of photoresist covering regions that one wishes to preserve.

The unprotected areas are either wet etched or dry etched with diluted acid (usually hydrogen peroxide and sulphuric acid, diluted with water) or an inductively coupled plasma (ICP) respectively. In both cases, the SPR350 resist is etched away as well as the exposed semiconductor surface, but at a lesser rate such that the approximate removal of the mask results in an etch depth down to the n-doped layers. Any residual mask is chemically removed. This completed etch is the first stage of the mesa, without the metallic contacts. An additional step is required to generate the horseshoe contacts. This step requires another deposition of SPR350 that is also aided by a secondary resist, PMGI.

The larger solubility of PMGI compared to exposed SPR350 results in an overhang of the SPR350 above the PMGI. The cavity generated underneath the overhang aids in the final step of diode generation which is metallic deposition. While it is described below, this process occurs last, after the creation of the photonic devices.

Metallic deposition is achieved by placing the sample under pure metallic (elemental) coils. A large current is passed through the coils which causes molecules of the metal to evaporate radially outwards (in an otherwise vacuum) and towards the sample. In this work, a combination of nickel and gold are used. A thin, 20nm layer of nickel is deposited to allow for better adhesion of the (much thicker) 200nm layer of gold which serves as the actual diode contact. Without the nickel, the gold risks being lifted off along with the photoresist in the cleaning stages. Whilst not as

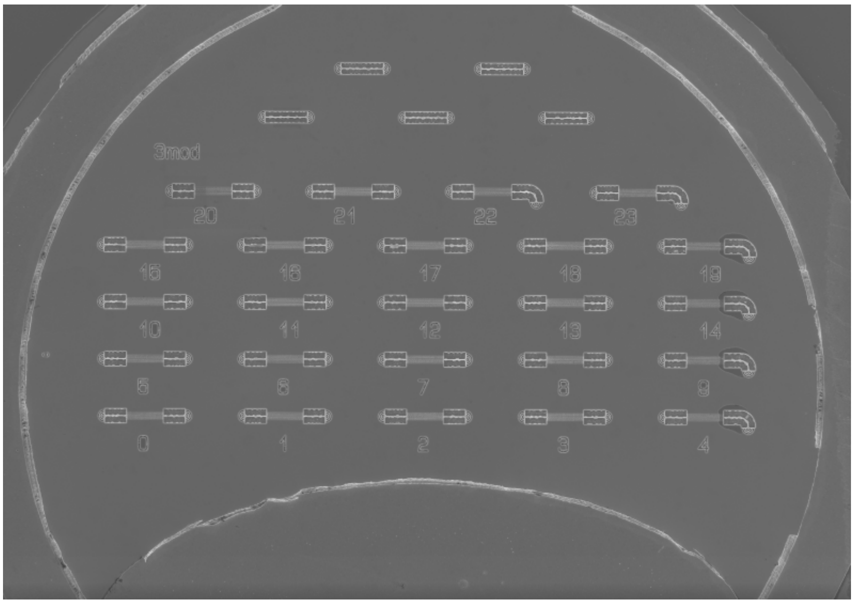

Figure 2.4: **SEM of 24 devices + 5 nanobeam waveguides** | The horseshoe gold contact is the elevated surface surrounding the numbered devices. This image is before the 3-point cleaning stage, which takes place before the wire contact bonding.

conductive as other metals, gold is chosen (in place of copper, for example) due to its lower intrinsic reactivity with external contaminants such as oxygen. Once the metals have been deposited, the finalisation of photoresist lift-off can take place. The overhang of the SPR350 over the PMGI ensures that a flat layer of the metal is deposited, rather than experiencing a build-up of deposition in the corner between the p-GaAs and the SPR350. Dissolving the photoresist lifts off the metal contact everywhere the resist is, leaving behind the horseshoe imprint, shown in figure 2.4.

The photonic patterning begins similarly to the diode etching, and is depicted in figure 2.5. Despite the similarity, PhC etching requires precision of tens of nanometres, rather than the many 100s of nanometer precision that photochemical etching can provide, and therefore electron beam lithography is performed. The process begins by coating the sample with a layer of SiO_2 via plasma-enhanced chemical vapour deposition (PECVD). Atop this layer sits the electron beam resist, CSAR62, which is applied via the spin coating method. E-beam lithography is performed on the mask, exposing a pattern in accordance with a Graphics Database System II (GDSII, or GDS) file.

GDS files direct the EBL process using a computer-generated design which details pattern profiles. The exposure to the electron beam is always modified from experimental design (e.g. PhC hole size) to account for undesired electron scattering and secondary electron generation in the proximity of other selected locations on the resist. This process is known as proximity correction, which allows for a better patterning fidelity by appropriately editing the doses used to generate smaller and larger holes. The exposure to the EBL alters the chemical bonding of the resist and makes exposed regions less robust to chemical developers.

The exposure process is lengthy, especially when compared to the diode photo-exposure, often taking more than ten hours to successfully etch an array of designs with different parameters. The parameters (such as overall dose and target hole sizes) are varied for a range of needs. The main purpose is to ensure that any imperfection in fabrication that may bring the operational wavelengths of the device away from the designed range is covered by another device instead, but the alterations also serve the purpose of generating devices which operate in different wavelength regions to

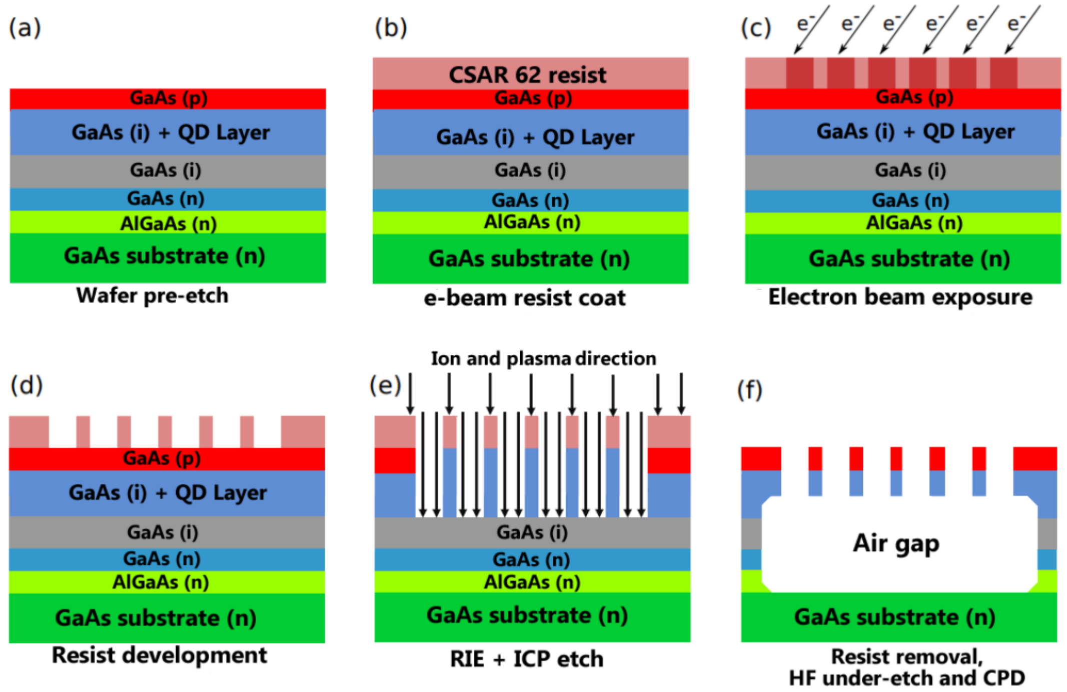
(a)
GaAs (p)
GaAs (i) + QD Layer
GaAs (i)
GaAs (n)
AlGaAs (n)
GaAs substrate (n)
Wafer pre-etch
(b)
CSAR 62 resist
GaAs (p)
GaAs (i) + QD Layer
GaAs (i)
GaAs (n)
AlGaAs (n)
GaAs substrate (n)
e-beam resist coat
(c)
e⁻ e⁻ e⁻ e⁻ e⁻ e⁻
GaAs (p)
GaAs (i) + QD Layer
GaAs (i)
GaAs (n)
AlGaAs (n)
GaAs substrate (n)
Electron beam exposure
(d)
GaAs (p)
GaAs (i) + QD Layer
GaAs (i)
GaAs (n)
AlGaAs (n)
GaAs substrate (n)
Resist development
(e)
Ion and plasma direction
GaAs (i)
GaAs (n)
AlGaAs (n)
GaAs substrate (n)
RIE + ICP etch
(f)
Air gap
GaAs substrate (n)
Resist removal,
HF under-etch and CPD

Figure 2.5: **Cross section of the photonic device etching stages** | An electron beam resist first coats the grown p-i-n wafer. This resist is then exposed to the EBL. This exposed resist is then developed, allowing for the RIE and ICP to quickly lift up the GaAs material, as is seen in **(e)**. Step **(f)** encompasses the processes of figure 2.6 but represents the end goal. The etching steps are described in detail in the text.

access the entire QD substrate emission range. After exposure, the sample is developed such that the exposed pattern on the e-beam resist is etched away, leaving behind a surface mask of CSAR62, and therefore an exposed surface of SiO_2.

Reactive ion etching (RIE) is performed on the sample which etches away at the SiO_2 only, until the first GaAs layer is reached. Following this, an ICP deep etch is performed into the sample layers, similar to the deep etch used to generate the diode mesas. The dry-etch ICP allows for very steep ($< 4°$ angle), anisotropic etch down to the surface of the AlGaAs (sacrificial) layer. The SiO_2 layer is then removed, as is any remaining CSAR62, with a water-diluted acid mix. Left behind is what is shown in the penultimate panel of figure 2.5, where the base pattern of the nanophotonic structures is imprinted onto the surface, etched down to the surface of the n-GaAs layer. The final step of this process is the HF underetch and the critical point dry (CPD).

In order to generate the suspended structures it is necessary to perform an underetch of the photonic patterns. Without this underetch, the principal mechanism of total internal reflection (TIR) of the generated light would not be present to guide the light

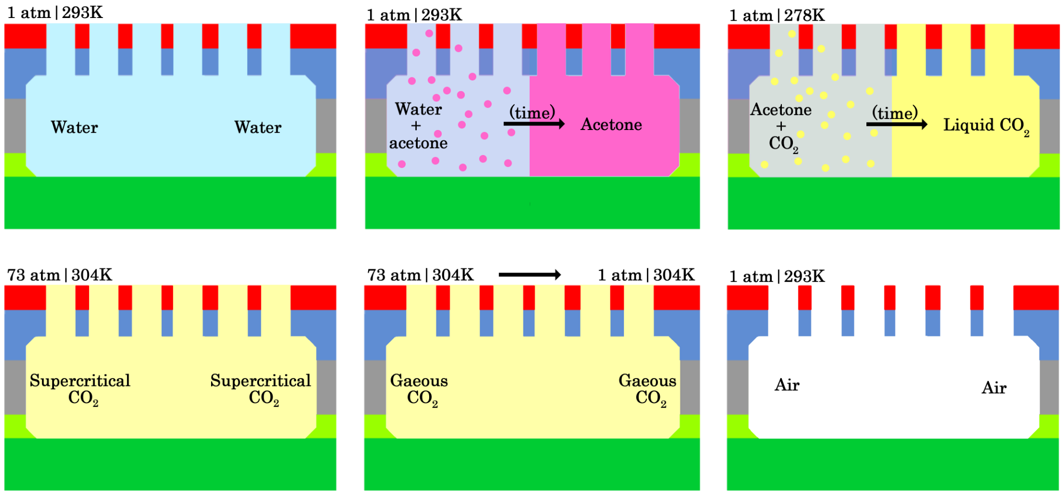
1 atm | 293K
Water
Water
1 atm | 293K
Water + acetone
(time)
Acetone
1 atm | 278K
Acetone + CO_2
(time)
Liquid CO_2
73 atm | 304K
Supercritical CO_2
Supercritical CO_2
73 atm | 304K
1 atm | 304K
Gaseous CO_2
Gaseous CO_2
1 atm | 293K
Air
Air

Figure 2.6: **Cross section of nanophotonic devices undergoing the critical point drying process** | Deionised water, used to wash away the HF to halt overetching, is eventually replaced by air through the CPD process. Similar to the main etching process, details are provided in the text. Each stage is depicted in the order progressing left to right, first along the top row and then the second row in the same fashion. Each stage involves a chemical in a thermodynamic state that is miscible with the contents already present.

along the length of the waveguiding structures. In order to perform an underetch, a multi-stage process is used. This process is depicted in figure 2.6. The process begins by using a lightly-diluted mix of hydrofluoric acid (HF) and water, which eats away at the $Al_{(0.6)}Ga_{(0.4)}As$ layer. This wet etch works because the etch rate of the $Al_{(0.6)}Ga_{(0.4)}As$ is 10^5 times faster than the etch rate of the GaAs layers. To avoid excessive underetch, the HF is removed by rinsing the sample in de-ionised (DI) water. However, the sample cannot be removed from the water due to the water's strong surface tension effects on the length scales of the individual devices. If the sample is removed, the evaporating water can tear any feature of the devices.

To circumvent sample tearing, the sample undergoes a process called a critical point dry (CPD). The CPD involves the use of acetone and liquid CO_2, across a variety of pressures (with small temperature variations) in order to remove the water from the system.

Acetone is added to the submerged sample, because acetone is miscible with water. A constant supply of acetone eventually removes all water from the system, which is maintained at 293K and standard atmospheric pressure (1atm). Now that the water has been removed, liquid CO_2 is introduced to the system, which has to be increased to over 50atm to maintain the liquid phase of the CO_2. As the acetone replaced the water, the liquid CO_2 replaces the acetone until pure liquid CO_2 is submerging the sample. The pressure and temperature of the system are increased to 73atm and 304K respectively, whereat the liquid CO_2 enters a supercritical phase. This phase allows transition to either liquid or gas through fine tuning the temperature and pressure parameters. A reduction in the pressure, whilst maintaining the 304K temperature, causes the supercritical fluid to undergo a continuous phase transition without ever needing to cross a phase boundary. The transition ensures that the liquid CO_2 does not have any surface tension that could damage the sample. Finally, the system is cooled and the previously supercritical fluid becomes a gas, which can be vented from the sample, leaving the suspended devices dry. Once the CPD is completed, the sample is ready to undergo bonding and mounting. First, the

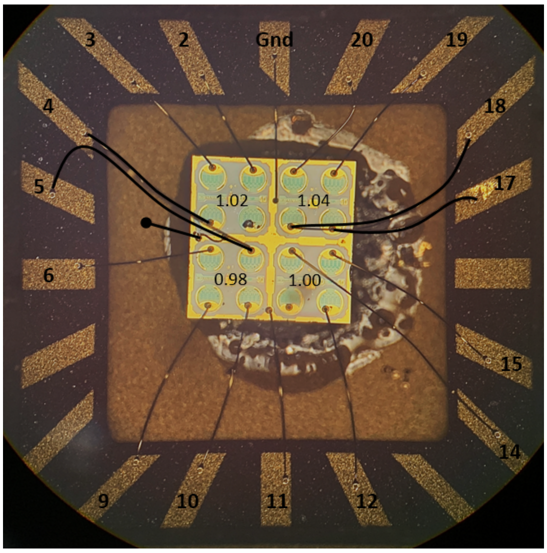

Figure 2.7: **Optical image of a final bonded chip, mounted on a non-magnetic ceramic carrier** | Each external, gold-painted pin is exclusively connected to individual diodes, except the ground pin, which has multiple contact points to prevent overall contact failure (as it is common to all diodes). These pins are labelled GND and 2 → 20. Glue sticks the wafer to the carrier to maintain alignment once placed into the cryostat, and to prevent further tension on the small gold wires. The different decimal values pasted across the arrays of horseshoes indicate the different EBL doses, generating different true values of etched hole sizes.

sample is mounted onto a square ceramic chip, approximately 1cm in dimension, as shown in figure 2.7. The ceramic chip is used to avoid interaction with external magnetic and electric fields which will be applied once the sample is placed into a cryostat. The individual processed diodes (along with two grounding connectors) are then connected through a gold wire bonder to the external chip-holder bond pads. This allows individual external biases to be applied to each fabricated diode. The diodes' electrical properties are always tested before the mounted ceramic chip is loaded into the experimental set-up. The contacts for the sample are not thermally annealed, as it was not deemed necessary to remove surface contaminants. However, one suggestion may be to perform annealing to remove such adhesives, allowing for more reliable diode behaviour.

Shown in figure 2.8 are IV curves for the sixteen different diodes that are present in the work described in chapter five. These curves provide some indication as to the functionality of the diodes in terms of the "turn on" voltage, which is usually marked as the voltage whereby the exponential current response to the applied voltage is appreciably distinguishable from noise. A typical diode has a turn on voltage at 0.5V at room temperature. At cryogenic temperatures (4K) the usual turn on is around 1V for a typical p-i-n, but the turn-on voltages for these diodes are slightly higher, as seen in figure 2.8 (which also shows room temperature IV curves, already higher than 0.5V), and is also seen in figure 7.3 of ref [100].

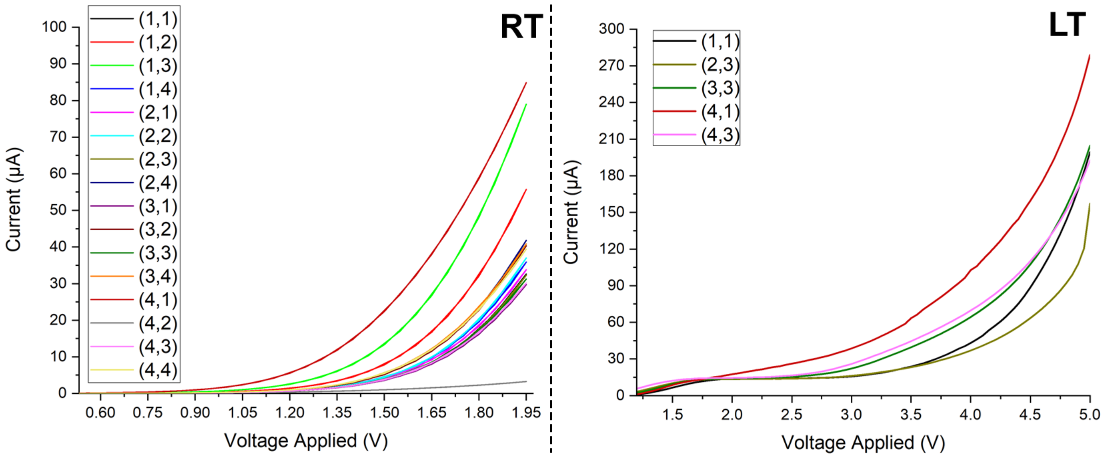

Figure 2.8: **Room temperature (RT) and cryogenic temperature (LT) IV characteristics for the diodes used in chapter 6** | The coordinate labels are defined relative to the matrix of diodes shown in figure 2.7, with the bottom left being (1,1) and the top right being (4,4). Only five pins are available in the cryostat for low temperature study. Diodes are chosen based on their design, SEM quality and electrical response. The colours marked on the LT plot are the same as in the RT plot. The low voltage behaviour (in the LT graph) of the low temperature plot is likely not due to the full diode behaviour, and is probably a contact resistance that accidentally forms from contracting material.

2.3 Experimental Set-Up, Cryogenics and Sources of External Fields

The work presented in this thesis features the sample fabricated via the steps described in the previous section, mounted in a bath cryostat for the duration of all experiments. A bath cryostat offers a mechanically stable platform to reduce vibrational effects which could reduce optical alignment, while also offering reliable temperature control for long periods of time. A depiction of the bath cryostat is presented in figure 2.9. A piezoelectric stage capable of laterally translating and vertically displacing the sample mount allows for fine control of the alignment of incident light across the sample surface. The cryostat chamber consists of a sealed tube filled with helium gas in which wires allowing for electrical control (for diode bias application and piezoelectric stage adjustment) run towards the sample mount. As an inert gas which retains its gaseous properties at cryogenic pressures and low pressures, helium inside the insert allows thermal conductivity between the liquid helium that surrounds the cryostat insert and the sample itself. A glass window at the top of the insert allows optical access which is moderated by two achromatic doublet lenses (f=400mm) to increase the field of view, and an objective lens (f=8mm, 0.55NA), allowing focussing of input light down to spot sizes of $1\mu\text{m}^2$ across a wide variety of wavelengths. The z stage of the piezoelectric stack allows for changes in focus for the objective lens. This can be monitored either by an infrared camera placed on the optical breadboard placed above the bath cryotstat and the mounted tube, or by monitoring the intensity of emission of a QD or a bulk measurement.

The optical breadboard on top of the cryostat mount allows for multiple optical excitation paths with tuneable polarisation and intensity, and also collection of emitted light. A 50:50 beam splitter directly above the glass window allows the input power towards the sample to be monitored.

A superconducting magnet capable of reaching magnetic field strengths of ±5T is placed around the piezo-stack housing as a coil. So long as the magnet is submerged in liquid helium to remain cold, the magnetic field can be maintained indefinitely with no additional external power supply. This is known as a persistent switch, and therefore changing the magnetic field by even 0.5T is a process that can take more than a minute as changes require a persistent switch heater (PSH). The coil is aligned in such a way as to provide magnetic fields in the Faraday geometry.

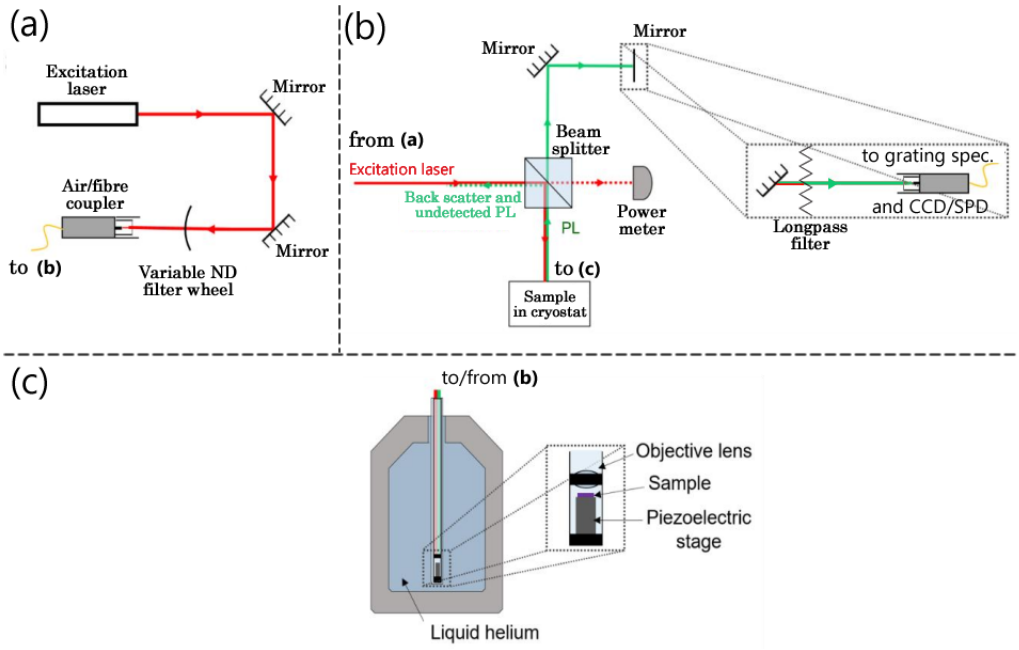
(a)
Excitation laser
Mirror
Air/fibre coupler
Mirror
to (b)
Variable ND filter wheel
(b)
Mirror
Mirror
from (a)
Excitation laser
Beam splitter
Back scatter and undetected PL
Power meter
PL
to (c)
Sample in cryostat
to grating spec.
and CCD/SPD
Longpass filter
(c)
to/from (b)
Objective lens
Sample
Piezoelectric stage
Liquid helium

Figure 2.9: **Experimental set-up used for probing samples discussed in chapters 4-6. Some components, such as polarisers, aren't shown as they do not appear in all experiments** | The excitation laser of segment (a) is either a non-resonant diode laser, a tuneable CW/pulsed laser, or a white light laser. Through the variable ND filter wheel, laser light can enter segment (b) with a user-defined power. Segment (b) depicts how light from (a) is passed towards the sample, (c), dictated by the red beam. The beam splitter is 50/50 to gauge how much power is directed to the sample. The green PL leaves the sample and is sent to the detection region.

2.4 Spectroscopy, Single Photon Measurements and Time-Correlated Measurements

The geometry of the bath cryostat allows for a series of experimental procedures to take place with the use of more external equipment. One method of optical investigation is spectroscopy in the form of μPL (photoluminescence performed on micron scales). This is performed with the assistance of a grating spectrometer and a charged coupled device (CCD) camera LN_2 cooled to 153K. Usually an external diode laser operating at 808nm is used for the μPL scheme because it is an “above-band” laser. The use of this laser is considered as non-resonant spectroscopy. This is further discussed in the next section. Different optical access points on the breadboard allow for resonant or quasi-resonant spectroscopy.

Diagrammatically the experimental procedure of applying non-resonant and resonant light are fundamentally similar, where the main difference is the wavelength of laser light, which, for the (quasi-)resonant schemes, is considered as “below-band.” The specific details of the measurement mean that incident laser wavelengths can differ between an energy resonant with a QD currently under study (e.g. $880nm < \lambda < 920nm$) which scales to shorter wavelengths by up to a few nm for the quasi-resonant case.

In the resonant case, usually a spectrometer and CCD combination is only used as a means to ensure laser light is being properly rejected. This is usually done with cross polarisation schemes, whereby a polariser sets the polarisation of the input resonant laser, and another polariser is used in the collection path to reject the same light. A signal is obtained despite the cross-polarisation because of the details of the photonic device, which alters the polarisation state of the incident light. Scattered light which does not couple to the device nominally maintains its initial polarisation and is subsequently rejected by the second polariser. Resonant schemes often involve single photon counting or time resolved/correlated measurements such as emitter lifetime, first/second order correlation coefficients ($g^{(1/2)}$) or Hanbury

Brown and Twiss (HBT) measurements. Such measurements can be performed with single photon detectors such as an avalanche photo diode (APD) or superconducting nanowire detectors (SNSPDs) and are assisted with a single photon counting module (SPCM) or counting card which interprets electronic data sent from the APD or SNSPD. See the appendix for an HBT measurement of the fastest QD from chapter 5. Additionally, these experiments can be further assisted either by optical (spectral) filters on the breadboard or the grating spectrometer to ensure only the signal of interest is collected. Single mode, polarisation-maintaining fibres are used to send light between the lasers, breadboard and detectors, with air-fibre couplers to collimate the light in and out of the fibre.

2.4.1 Resonant and Non-resonant Spectroscopy

Non-resonant (NR) spectroscopy, in the form of μPL is a highly useful technique used to identify and characterise not only single QDs but also the behaviour of nanophotonic devices through high power transmission schemes. NR spectroscopy is the simpler to experimentally achieve compared to resonant spectroscopy. The experimental ease relies on the fundamental mechanism of light generation. This mechanism is far less sensitive to laser focus, power and QD charge population, as well as not requiring proper polarisation rejection, as stray laser light can be rejected by a filters such as dichroics. In a wafer without doped layers, a non-resonant laser incident on the sample generates charges within the semiconductor material (GaAs) by being above the band gap of the material. The generated electrons and holes fall into the QD potential trap whereby they become an exciton. Excitonic recombination occurs at the characteristic QD energy and the spectral position and linewdith are recorded. This process allows for multiple QDs to be studied simultaneously using the spectrometer/CCD system.

A good QD candidate often demonstrates intensities of 10kHz/μW beneath the saturation limit, and ideally has a resolution-linewidth of around 14μeV using an 1800 lines/mm grating in the spectrometer. In reality, the μPL linewidth is much narrower, but the measurement is limited by the spectroscopic method, as the diffraction is limited by the spacing between each slit on the grating, in accordance with the diffraction equation $\lambda = dsin\theta_m$, for an incident wavelength, λ, onto the grating with line spacing d (such that 1/d is the grating or lines/mm), producing a pattern consisting of orders marked by m, each at an angle θ_m.

Measurement of narrower linewidths relies on resonant spectroscopy. Unlike in NR spectroscopy, resonant spectroscopy relies on direct generation of charges inside the QD. Since the incident laser is not above the band gap, the laser does not generate a multitude of charges in the local area of the emitter. The result of this is an exciton generated inside the QD with minimal environmental interaction in the form of spectral wandering - a consequence of the quantum-confined Stark effect (QCSE). The QCSE will be discussed in section 2.5. The lack of extra environmental interaction results in a narrower linewdith of the QD than in the NR case. Resonant measurements can occur at much lower powers than in the NR scheme for the same number of emitted counts due to the direct nature of QD population. Resonant measurements are often used for investigating individual QDs at one time, rather than measuring a multitude of QDs as one would in PL. Resonant measurements, unlike μPL measurements, therefore go beyond basic optical studies involving brightness and linewidth, and extends into time-dependent measurements.

In order to study individual quantum dots on a time-dependent basis, a different excitation scheme is used. Instead of continuous wave excitation where the population time of the QD is uncertain, a pulsed scheme allows for more detailed temporal studies of a QD such as the lifetime of the state (important for photonic crystal effects, discussed in chapter three). Pulsed lasers have regular spacings between individual pulses, with short temporal widths (known as pulse duration) on the picosecond time scale. Additionally, an adjustable pulse area (e.g. π-pulses) allows for qubit control [101–103]. The next subsection discusses the use of pulsed lasers for temporal measurements of single photon emission.

2.4.2 Single Photon Measurements and Time-Correlated Measurements

In chapters five and six, work is presented on time-dependent measurements for single-emitter lifetime and spin pumping respectively. The work in chapter five includes focus on the use of quasi-resonant pulsed lasers and temporal correlation between the pulsed laser and emitted light, whilst chapter six explores the application of single photon detection in a resonant setting. Chapter five discusses quantum dot lifetimes. The lifetime of a QD is a measure of the timescales in which an exciton recombines within the dot. Each population cycle summons a probability that the charges recombine after a "random" time, with each time instant governed by probability laws.

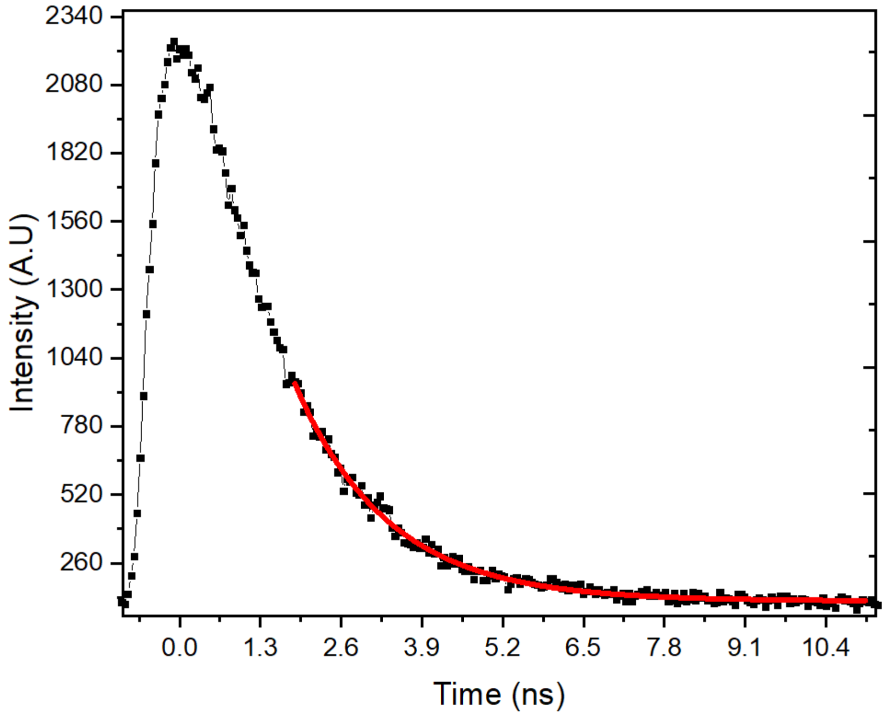

Figure 2.10: **Example QD lifetime data of a QD integrated in a nanobeam waveguide** | Each datum represents one in a series of time-resolved PL measurements resulting from pumping a QD with a laser pulse. The QD is more likely to emit at shorter lifetimes, and the probability is governed by the lifetime of the emitter. The bottom half of the data set is fitted with an exponential decay (in red) to avoid fitting a convolution of the detector response. Knowing the temporal detector response to the pulse excitation laser allows the fitting of a convolution, but this is mitigated by fitting the lower half of the curve.

The probability curve is exponential, and the lifetime, τ, is the exponential decay constant that characterises the frequency with which the emitters recombine at any particular time after population. A typical InAs QD in bulk (without any influence of a nanophotonic structure) has a lifetime of around 1ns. Typical lifetime data is shown in figure 2.10. In lifetime experiments, the QD is populated many times and the statistical curve is built up in the figure. This measurement provides an upper limit to the number of photons per unit time that can be collected from the emitter. The concept of exciton lifetime is important for chapter five as part of the designed structures rely on an engineered decrease of emitter lifetime, or the increase of emitter brightnesses.

For lifetime measurements above 400ps (i.e. non-resonant or some quasi-measurement scenarios), APDs can be used as the detector. A pulsed laser of repetition rate $12.5(\mathrm{ns})^{-1}$ is used to excite the QD region. The pulse also strikes a photodiode which is used for heralding the counts for the APD. The QD emission is identified from standard μPL using a CW above-band laser. The grating spectrometer is then used to filter the QD line of interest using the side-port exit. The other port is directed towards the CCD, which is not used directly for lifetime experiments. Light from the side port is sent to the APD, which is connected to a photon counting card along with the heralding photodiode. The time difference between the photodiode and APD signal is marked, and the lifetime spectrum is built up after billions of recombination events.

2.5 External Fields

The application of external electromagnetic fields is very important for a variety of reasons. In experiments described in chapters 4-6, static electric and magnetic fields are applied to the samples (often in tandem.) Such external fields allow for energetic tuning of QD states, as well as polarisation control, population stability and QD charging [104]. The individual effects of each field are described in the following subsections.

2.5.1 Electric Fields and The DC Stark Effect

Due to the implementation of the p-i-n diode, an electric field, without further modification to the experiment, is permanently applied across the QD layer. Similar to atomic interaction with external electric fields, occupants of quantum dots experience energy perturbations described by the quantum confined Stark effect (QCSE). The individual charges each experience interactions with the electric field to reduce their energies, decreasing the energy of the exciton state inside the QD, red-shifting the photon energy upon recombination. The functional form of the energy shift is provided by equation 2.1:

$$-\Delta E = -\Delta E(F) = \mu F + \alpha F^2 \tag{2.1}$$

describing a change in energy, ΔE, for an applied electric field, F. μ is the permanent dipole moment of the exciton and α is the electric polarisability. The applied field can cause the conduction and valence bands in the system to tilt (sometimes referred to as bending), eventually allowing the individual charges to tunnel in and out of the QD towards the appropriate doped layers. This tilting redshifts the transition relative to a QD surrounded by intrinsic semiconductor material. The diode mesas and the electrical contact allow for external biases to be applied to these systems, either allowing for reverse biasing (whereby the built-in potential is enhanced) or forward biasing, which reduces the tunnelling barrier between the QD and the p- or n- contacts, allowing for deterministic charging due to the Coulomb blockade, and population stability inside the QD. Since the application of electric field is achieved by applying an external voltage (bias) to the devices, future reference of any applied electric field will refer to applied bias or voltage.

Within the stability region of the QD, the exciton can experience wavelength shifts up to 1.5nm. This total value is a result of the Stark shift alongside the energy jump caused by the state shift caused by a tunnelling charge in accordance with the Coulomb blockade. The wavelength shift amount differs from dot to dot, and is grouped in differences further between individual diodes, some of which provide nearly no shift at all to the exciton lines, though this is less likely to do with the dots themselves, and likely to be an artefact of fabrication issues with the doped layers. Figure 2.11 shows the result of a μPL illumination on an unetched location on one of the samples. It can be seen that a series of lines remain stable, but become brighter through the application of external bias, whereby the lines blueshift. The blueshift comes from the forward bias scheme, where the external bias works to eventually neutralise the built-in potential, and effectively reduce the amount of redshift due to the QCSE. At a certain voltage, the lines appear to disappear and reappear at different energies, all with a similar spectral shift. This shift is attributed to single electron charging, as the system eventually approaches the flat band regime. This tuning is useful in this work for spectrally moving emitters closer to, or further away from, the crossing points of the glide plane waveguides' dispersion discussed in the next chapter. Charging of the QD allows for the creation of charged exction states. As described in section 1.4, the single electron charging allows for coupling between the photon polarisation and a QD spin.

In addition to energetic tuning, the reduction of a built-in potential allows for a more stable environment for the emitters. The application of external voltage ensures that any nearby charge traps, caused by interstitials in the crystal, for example, are saturated and hence neutralised by carriers (which are now not pulled towards to the doped layers). Any carriers captured by the a defect have a low tunnelling probability for low crystal temperatures. The saturation of defects from unwanted carriers shields the quantum dots from any spurious fields which could change the exciton state energy.

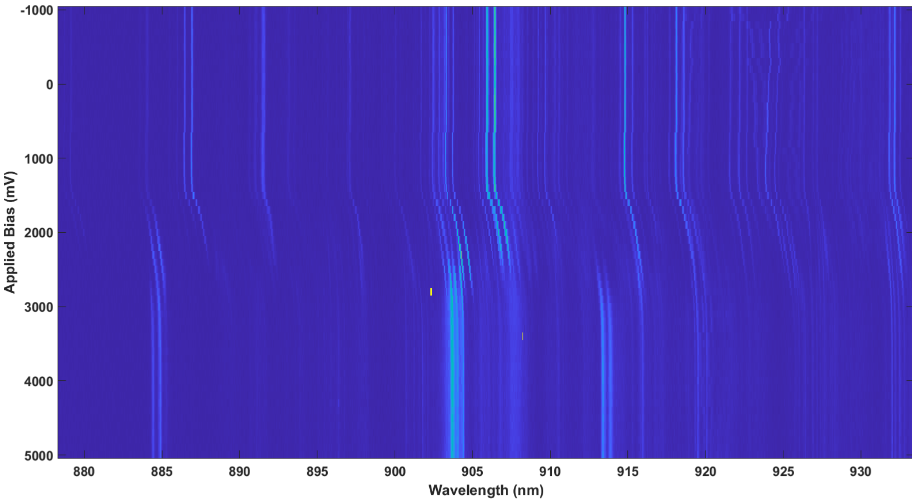

(a) **PL tuning map of QDs under a B field** | This spectrum is obtained with 4W of non-resonant, 808nm incident power. Around 1.5nm of tuning is present for QDs which do not uniquely experience charging. The Coulomb blockade begins at around 2.5V.

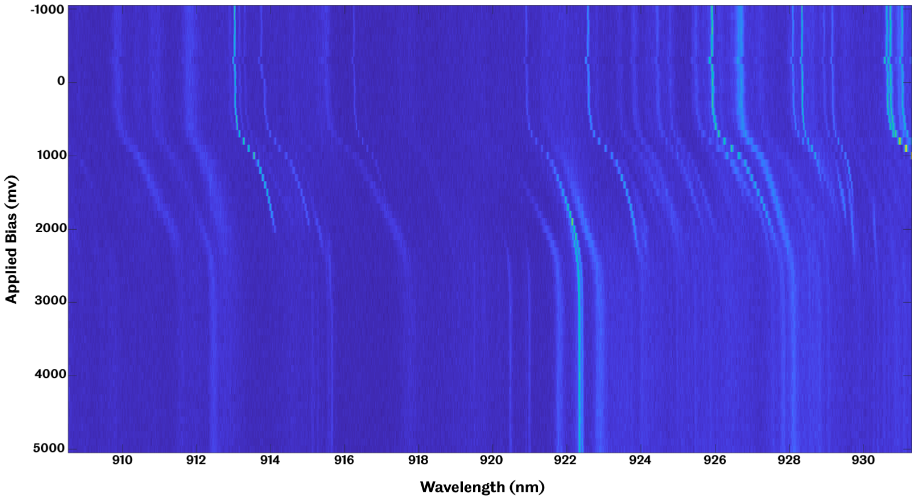

(b) **A PL map taken under similar experimental conditions on a different diode, with zero B field.** | The single electron charging behaves similarly for this diode as it does above. Here, the "turn-on" voltage is around 0.7V, with a similar tuning range of 1.5nm.

Figure 2.11: Photoluminescence is obtained under a 1s exposure of 4W of applied laser power at 808nm. At each voltage step between -1000mV and 5000mV, a PL spectrum is taken. The bright spots are cosmic rays. The doublets of lines are because of the magnetic field's effects. The tuning range begins at a similar location to the current (turn-on) response, around 1.5V. Around 1.5nm of tuning is applied to the QD lines over a 1V range, after which the intensity remains the same. Eventually, carriers can tunnel directly from the p- and n- contacts to directly produce electroluminescence, though the effects are not obvious here. Some QDs do not appear to charge, but many do. The reason is unclear.

2.5.2 Magnetic Fields

Magnetic fields are crucial for this research area of chiral semiconductor photonics. Chapter 3 will discuss the origin of chirality in nanophotonic devices. There are two potential geometries in which a magnetic field can be applied to a QD system. Any arbitrary field vector can be described as a combination of the two perpendicular configurations, which are known as Voigt and Faraday. These two configurations (geometries) feature a magnetic field applied along the plane of the QD growth axis, or perpendicular to the plane of the growth axis respectively. The Faraday geometry is present whenever a field is applied in the work presented in this thesis, and is provided by a solenoid inside the bath cryostat, as described in section 2.3. The Voigt geometry is not used here, but the physical effects of emitters under the influence of a Voigt field are relevant and interesting.

As discussed in the introduction, the QD states for consideration are the bright exciton states: the neutral and the charged exciton. For the neutral exciton, under zero magnetic field, the unperturbed state is one where recombination of the e-h pair produces circularly polarised light, with the polarisation reflecting the two possible ($|\uparrow\Uparrow\rangle$ and $|\downarrow\Downarrow\rangle$) spin combinations. These polarisations are degenerate in energy, which, does not permit the distinguishability of the two spin states from which the photon was created. This degeneracy is problematic because the majority of detection relies on light scattering from grating outcouplers attached to the ends of the photonic devices, which modify the polarisation state of the photon that reached them. This is to say, a left circularly polarised photon and a right circularly polarised photon could strike either end of the photonic device, and it would not be possible to determine which photon was which because of the polarisation “deletion” posed by the outcoupler.

For the neutral exciton (at B=0), however, the excited state degeneracy is broken due to the anisotropic exchange interaction of the electron and hole, producing a non-degenerate pair of states whose spins couple to the horizontal and vertical polarisation states of an emitted photon. This would be sufficiently ideal for polarisation

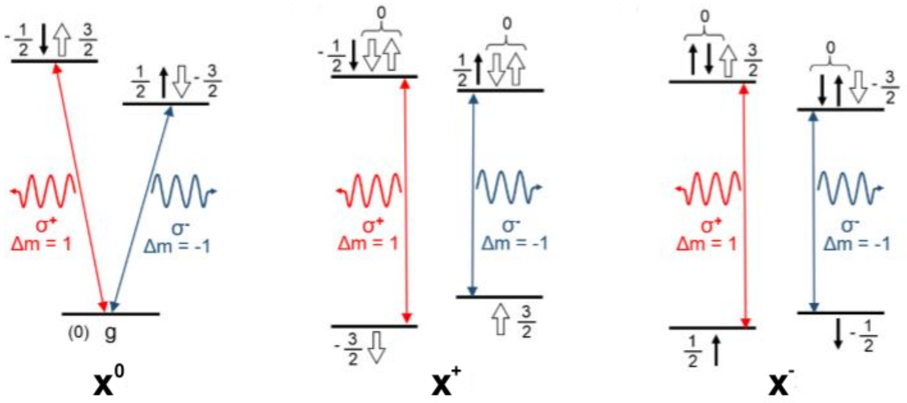

Figure 2.12: **Neutral, positively, and negatively charged exciton states** | These states are under a magnetic field to lift the degeneracy of the ground states of the charged species. The B field also overcomes the FSS and restores the circularity of the neutral exciton recombination paths.

distinguishability, but not only are the devices under study are optimised for circular polarisations, which couple both linear polarisations equally, but the grating out-coupler patterns are designed such that the emission from either side of the device is identical.

Similar to the neutral exciton unperturbed states, the charged exciton spin states ($|\uparrow\downarrow\Uparrow\rangle$ and $|\uparrow\downarrow\Downarrow\rangle$) are a pair of energetically degenerate circularly polarised photons, giving rise to the same identification problem. In order to solve this, an applied magnetic field generates a Zeeman splitting of the two exction species owing to the spins of the carriers. The geometry of the applied field affects the polarisation states differently but the energy splitting is present for both Voigt and Zeeman configurations. A Voigt field causes the bright and dark exciton species of the same symmetry to intermix, allowing for coherent optical spin control of lone charges in the two trion species since all transitions are optically allowed. The neutral exciton does not gain a circular polarisation under the Voigt configuration, but does experience multiple energy splittings, revealing four transition energies. The Faraday geometry is much simpler in terms of the effects on the polarisation states of the three exciton species. Figure 2.12 is shown in chapter 1's introduction, but is included again here as a reminder. It shows the optically allowed transitions of the neutral and charged exciton in a non-zero Faraday magnetic field. The Zeeman energy has to be large enough to overcome the fine structure of the neutral QD to fully circularise the transitions. It can be seen that all relevant states become circularly polarised *and* spectrally distinct, allowing for the energy of the transition to be the marker for the polarisation state. The energy shift for each state is represented in equation 2.2:

$$\Delta E_{Zeeman} = g_{ex}\mu_B B + \gamma B^2 \tag{2.2}$$

where g_{ex} is the exciton g-factor, μ_B is the Bohr magneton and B is the magnitude of the magnetic field. The exciton g factor is the cumulative g factors for the individual carriers inside the QD, and is a measure of the coupling strength to the magnetic field. QD state g factors depend on a variety of parameters such as size, shape [105, 106] and strain. They can be manipulated to have their magnetic responses changed via external influences such as strain [107]. Neutral exciton g-factors can be measured to be up to magnitudes of over 2 [108] (the free electron g-factor is around -2), with the majority of the g-factor coming from the hole inside the dot [109]. γ represents the diamagnetic shift the exciton experiences. This quadratic shift becomes more prominent at higher magnetic fields, but does not act to split the exciton state through the Zeeman interaction, which is purely described by the $g_{ex}\mu_B B$ term.

Chapter 3

Optimisation of Chiral Behaviour Inside Nanophotonic Structures

The deterministic routing of flying qubits is an essential feature for information control on-chip. Ensuring that light is faithfully guided in the desired direction from the emitter is a challenge that first relies on the emitter coupling to the waveguiding structure. A variety of nanophotonic structures exist for the purposes of guiding light, each with their own specialist role. This chapter will present a breakdown of some of the most common III-V architectures that have been used to guide light and host light-matter interactions, leading to an introduction of the glide-symmetric designs which are a large focus of this thesis. This chapter will re-introduce chirality (expanding on section 1.6) in the context of confined electromagnetic fields, presenting a parameter known as the directional beta factor. The origins of chirality are shown through the Maxwell equations, and the experimental capabilities of both old and new nanophotonic devices to house chiral behaviour are discussed.

3.1 Introduction to Nanophotonic Devices and Chirality

On-chip confinement and capture of light (both classically and quantum mechanically) is a rapidly maturing field of study, with many successful implementations of devices designed to guide, re-route and filter a broad spectrum of light. The manipulation of light is possible not just for multiple designs, but also for a range of materials. Materials such as gallium arsenide and silicon nitride have been used to produce ridge waveguides [44], which are a popular means of guiding light, where the ease of fabrication allows for promising scalability, but often at the expense of competitive beta factors, which is a parameter introduced in chapter 1. Figure 3.1 shows a variety of nanophotonic devices such as waveguides, resonators and beam splitters. In this chapter, only waveguides are relevant.

A more recent attempt to control the flow of light is through the world of topological photonics. A resulting plethora of topological photonic crystals, such as valley-Hall and spin-Hall PhCs [110], have novel mechanisms which offer impressive defences to fabrication imperfections and sharp turns in the confining waveguiding structure,

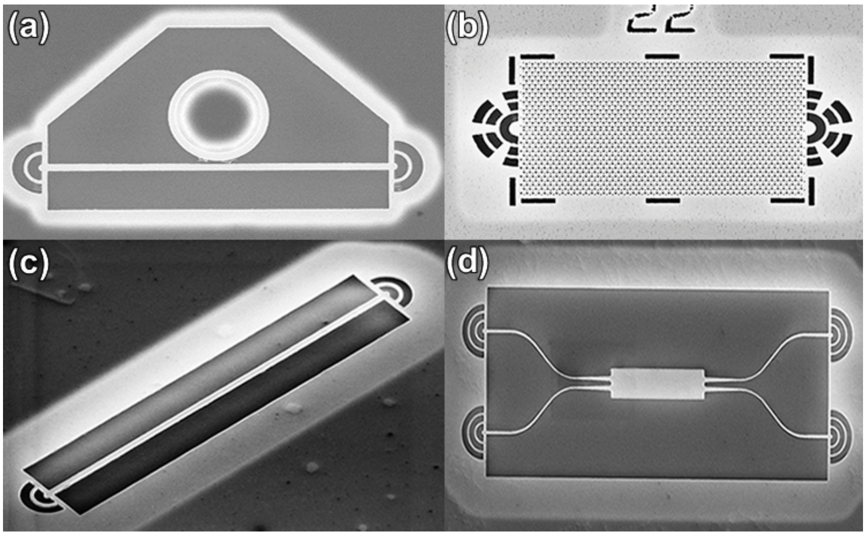

Figure 3.1: **Series of scanning electron micrographs of various nanophotonic designs** | (a): a ring resonator of radius 2μm and 350nm width; (b): quantum valley-hall [111] topological waveguide; (c): standard nanobeam waveguide; (d): multi-mode interferometer (MMI) splitter.

but these advantages are met with low β-factors [112], and large charge surface noise to embedded emitters due to the proximity of the emitter location and air holes. Current research is aimed at exploring the trade-off between these losses and the unique defences (known as topological protection) such crystals provide.

It is clear that an optimised waveguide should possess a strong beta factor, allow for broadband operation for transmission of different photon energies, and, in this work specifically, offer large spin-coupled directionality, otherwise known as chirality. Taking the β-factor as it was defined in the introduction, it is possible to observe a directional β-factor for a position in a waveguide which does not induce coherent reflections due to perfect scattering. The β-factor can also be refined further to include a directional component, whereby the emission rate, γ, is split into left and right components, yielding:

$$\beta_{L/R} = \frac{\gamma_{L/R}}{\gamma_L + \gamma_R + \Gamma} \tag{3.1}$$

which can describe asymmetric coupling due to non-reciprocal emission. The directional β-factor presents an insight into chirality, where highly chiral emitters will demonstrate nearly unity values for $\beta_{L/R}$ so long as Γ remains small. For no losses, and a perfect chiral emitter, $\gamma_L \ or \ \gamma_R$ is 1 (with the other being zero) under the consideration of a single spin state under a corresponding direction. Following this logic, a perfect non-chiral system hosts values of $\gamma_L \ and \ \gamma_R$ as 0.5. Since the losses normally cannot be measured, a different method is employed to define directional contrast (or chirality). This is governed by:

$$C_{L/R} = \frac{I_{L/R}^{\sigma+/-} - I_{L/R}^{\sigma-/+}}{I_{L/R}^{\sigma+/-} + I_{L/R}^{\sigma-/+}} \tag{3.2}$$

where an intensity, I, is measured for either of the $\sigma^{+/-}$ components. The L/R subscript refers to the light collected at either the left or right device output (such as a grating outcoupler or a fibre end). As an example, a perfectly chiral QD measured at the left outcoupler will see a left contrast, C_L of $(I^{\sigma-} - 0)/(I^{\sigma-} + 0) =$

$(I^{\sigma-})/(I^{\sigma-}) = 1$. This presumes that only left circularly polarised light travels towards the left outcoupler. The choice of polarisation for this example is arbitrary and makes no difference to the result in principle. In this definition, studying the chirality of the other transition (by observing the right outcoupler) produces a contrast of -1, but this result is fundamentally the same: only one exciton transition can be seen from one outcoupler at any time for a chiral emitter.

3.2 Origin of Chirality

In electromagnetism, chirality is a natural consequence of the confinement of light by matching the wavelength of the light to the size scales of the confining material. As a specific example, the nanobeam waveguide dimensions studied at Sheffield (often kept at this size as a reference for nanophotonic structures) are 183nm thick and 270nm wide. Simulation shows that single mode operation of the nanobeam can support wavelengths up to and a little above 1000nm, depending on the acceptable levels of transmission, as longer and longer wavelengths beyond the point of single mode operation simply introduce more losses and the volume of the wave is insufficiently confined. Unlike free space propagation, the confinement allows for the introduction of a longitudinal component of the electric field within the waveguide, which is usually not considered in free space wave propagation.

A propagating wave inside a waveguide sees internal reflection from the guiding structure (such as total internal reflection caused by real refractive index contrast), and the reflecting waves (which are also travelling forwards) must contain a component along the direction of travel, a principle satisfied by the boundary conditions of the waveguide. A special feature of the longitudinal component of the field is that the phase difference between it and the transverse components within the waveguide is constant. This constant phase difference magnitude between the two orthogonal components (transverse and longitudinal) is $\pi/2$, and is essentially uniform along the width of the confining geometries used for chiral applications, and is a consequence of the consideration of the longitudinal field within the waveguide.

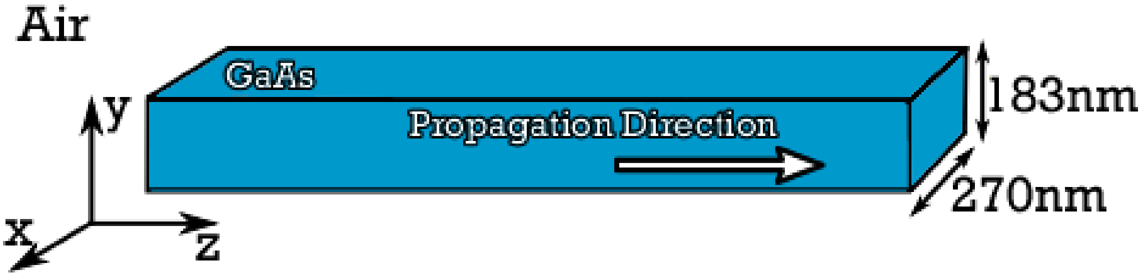

Figure 3.2: **Layout of a rectangular nanobeam waveguide, clad in air** | The dimensional size of 183 x 270 nm reflect the nanobeams which appear on the diodes present for the work in chapter 5. The axes are specified such that the z axis is the longitudinal direction, and the x-z plane is normal to the growth axis, along y. The InAs layer of QDs is at the middle of the height, 91.5nm along the y-axis.

The general representation of a an electric field is presented in equation 3.3, for a vector electric field amplitude $E_0(x, y)$, travelling in the z direction, having angular frequency ω. The general modes of the waveguide are not strictly TE or TM, insofar that they carry an electric and magnetic field in the direction of propagation, and are known as TEM in a general sense. See figure 3.2. Without too much loss of generality, $\mathbf{E_0}$ is not considered a function of ω, as it varies slowly relative to the intensity changes in space. In addition to this, the electric field in the $\hat{y}$ direction won't be considered as an integrated emitter will be idealised to produce a field only in the (x,z) plane. Subsequently, the $\mathbf{E}$ field is presented:

$$\mathbf{E(x, y, z)} = \mathbf{E_0}(x, z)e^{i(kz-\omega t)} = (\mathbf{E_x}, \mathbf{0}, \mathbf{E_z})e^{i(kz-\omega t)} \tag{3.3}$$

In free space, a travelling transverse wave is usually considered to have zero electric field component in the direction of travel, and exists only in an x-y plane. The confinement of the electromagnetic field and the subsequent introduction of a longitudinal field (which slowly varies over the z direction), produces an interesting result when considering the local (differential) Gauss law in equation 3.4.

$$\nabla \cdot \mathbf{E} = \frac{\rho}{\epsilon} = 0 \tag{3.4}$$

which, when taking equation 3.3 into account, implies that

$$\frac{\partial}{\partial x} E_x e^{i(kz-\omega t)} + \frac{\partial}{\partial y} E_y e^{i(kz-\omega t)} + \frac{\partial}{\partial z} E_z e^{i(kz-\omega t)} = 0 \tag{3.5}$$

By considering the slow variation of the field intensity across z (i.e. sending, $\frac{\partial}{\partial z}E(z)$) to zero, the resulting equation is:

$$-ik\mathbf{E_0}(z) = \partial_x \mathbf{E_0}(x) + \partial_y \mathbf{E_0}(y) \tag{3.6}$$

where $\mathbf{E_0}(x/y)$ refer to the individual $\hat{\mathbf{x}}$ and $\hat{\mathbf{y}}$ components of $\mathbf{E_0}(x, y, z)$. $\partial_{x,y}$ are condensed partial differential operators with respect to their subscripts. This equation effectively describes the relationship between the electric field in the direction of propagation relative to the electric field intensity in the cross section of the waveguide. The imaginary unit factor, i represents a 90 degree phase relationship between the sum of the changes in the electric field in the plane of travel and the longitudinal (z) component. This phase relationship between the z component and the in-plane components is effectively constant in magnitude across the width of the confining structure. A full derivation of the individual electric (E) and magnetic (H) fields for a dipole emitting into a ridge waveguide is provided in Coles' thesis (pp.119-122) ([113]). In this approach, the two curl equations from Maxwell's equations can have the generalised propagating mode inserted into them (equation 3.5) to reveal six component equations for $H_{x,y,z}$ and $E_{x,y,z}$ with respect to the three partial derivatives $\partial_x, \partial_y, \partial_z$. When the electric field in the longitudinal direction is considered to be constant, i.e. $\frac{\partial}{\partial z}$=0, a dipole in the (x,z) plane will result in the relation:

$$-ik\mathbf{E_0}(z) = \partial_x \mathbf{E_0}(x) \tag{3.7}$$

whose imaginary unit implies the $\pi/2$ phase shift between the two linear fields, which, when combined, produce an elliptical polarisation.

The intensity of the two electric fields components differ based on the lateral (x) position in accordance figure 2b from [63], which also shows the phase difference between the (constant) transverse and longitudinal components. The phase differences is seen in figure 3.3. The only exception is in the centre of the structure, where a sign flip of the phase difference between $\pi/2$ and $-\pi/2$ must cross the boundary over 0. The superposition of the two electric field modes produces an overall electric field with an elliptical polarisation in general. Within the regions where the phase difference is constant, the degree of ellipticity changes only in accordance with the relative intensity of the two components. Towards the centre, the ellipticity is small, due to the larger difference between the magnitude of the two electric fields. This disparity becomes smaller as the chiral regions are approached, at which point the intensities of the two fields match exactly. Both of the intensities change as the confinement profile is different for each oscillation direction. The polarisation profile caused by the addition of the two electric fields can be found in simulation by injecting waveguide modes or by placing electric dipoles (representing the exciton states) into a device of choice. All simulation performed for this work was carried out in Lumerical. Lumerical is a finite-difference time-domain (FDTD) solver which works to numerically calculate different electric and magnetic fields in certain directions at the vertices of a 3D rendered mesh.

The calculations are performed numerically by “solving” Maxwell’s equations, with the final results being measured through a series of monitors which can be placed

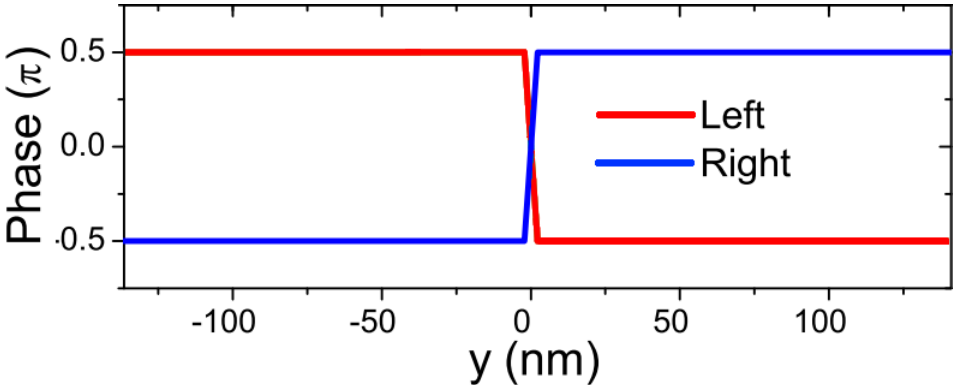

Figure 3.3: **Phase between the z and y components** | Phase relationship of the two circularly polarised states within the nanobeam waveguide. Here, the y direction the same as the x direction in figure 3.2. The phase is constant apart from very, very close to the centre, at which point is flips. Figure taken from [100]

at any location in the simulation to measure the incident power or simply the raw electric or magnetic field components.

Multiple styles of simulation are performed to characterise a device. Such simulations can measure the overall transmission of broadband light through a device, model the potential chiral behaviour of a design, or study the intensity of the electric field across the device. The band structures of the devices can also be investigated using MIT Photonic Bands (MPB), a software package specifically designed for finding "band structures, dispersion relations and electromagnetic modes of periodic dielectric structures." MPB was used to generate the dispersion curves shown in chapters 3 and 5, whereas Lumerical's FDTD was used to produce the rest of the simulated images, such as the electric field map in figure 3.4.

By injecting a mode into the device, the polarisation profile of the waveguide can be accessed, and a so-called polarisation map can be produced, which shows the a 2D colour intensity map of circular (or linear) polarisation. Such an example is shown in figure 3.4, which depicts a nanobeam injected with a broadband (100nm-wide) mode source. For the infinite nanobeam case, a clear progression from circular to linear polarisation can be seen, from the centre to the sides, with the largest chirality

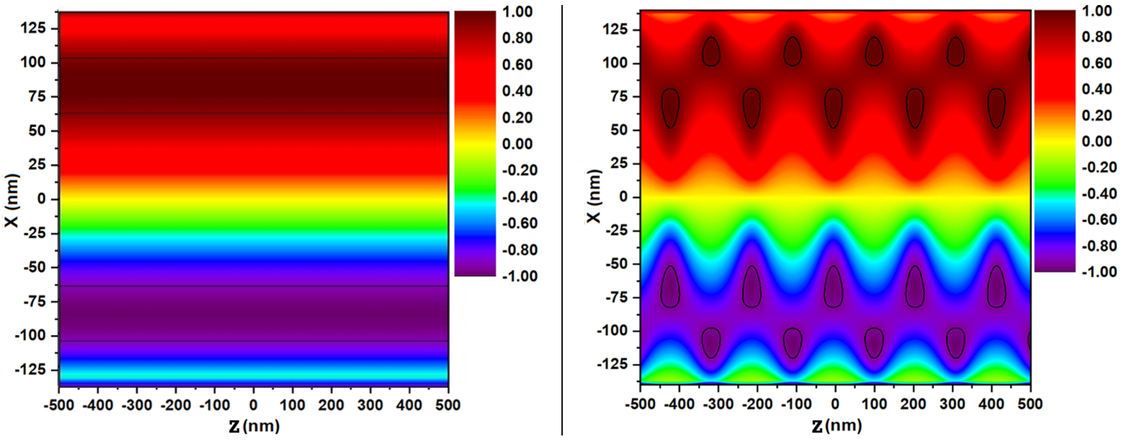

Figure 3.4: **Birds-eye view of the circular polarisation (S3 parameter) of an infinite (left) and terminated (right) nanobeam waveguide** | The pattern of the terminated plot is caused by Fabry-Perót oscillations cause by the effective cavity introduced by the outcouplers of the device. Were the reflectivities of the boundaries between the waveguide and outcoupler 0, the plot would be similar to the infinite case. The black outlined areas are regions of chirality greater than 90%. Plots are courtesy of D. M Price, see ref [100].

attainable being at approximately 3/4 the way from the centre to the nanobeam sidewalls. In any device, the location at which the chirality is maximised is named a "chiral point." It should be noted that exciting the waveguide from the other direction produces the same result except the polarisations are flipped. When these two simulations are combined, the desired result that opposing polarisations travel in opposite directions is revealed.

3.3 The Nanobeam Waveguide (NBWG)

One of the simplest methods to guide light on chip is the suspended nanobeam waveguide (NBWG), or simply nanobeam. Such nanobeams are one of the easiest photonic structures to fabricate (compared to other suspended structures) by having no need for complicated proximity corrections in the EBL stage due to the simple axial symmetry of the structure. Furthermore, because the NBWG confines light only through refractive index contrast, there is no need for additional surrounding semiconductor material like the photonic crystal architectures, meaning HF acid underetches are easier to perform.

The nanobeam hosts a series of benefits for (chiral) on-chip photon routing by having no particularly complicated or intrinsically chiral geometry. Care must be taken to ensure the waveguide is of the appropriate width and height, finding the balance between a single-mode behaviour and reliable β-factors. A regular NBWG provides a minimum β-factor of around 70% (for circularly polarised light), moderate chiral areas, whereby 34% of the nanobeam area allows for chiralities greater than 80%, and 14% of the area provides chiralities above 90%. Discussed later, this is drastically higher than the chirality of the W1 photonic crystal, and also over half the impressive chiral statistics of the modified glide plane designs presented in section 3.5. Suspended nanobeams are universal in their on-chip network application, insofar that they can be coupled to a variety of specialist structures such as the W1 defect photonic crystal (see below), structures with a glide plane geometry and even topological structures, albeit with a few modifications to enforce better mode and group velocity mismatch. Additionally, the nanobeam mode shape couples to a variety of grating outcouplers to send (bring) light off (on) chip. A series of designs are shown in figure 3.5, but the ones used in this work are the double-ring gratings featured in part (c). The shallow etch gratings featured in (a) are better than the double ring gratings, insofar that their back reflections are dramatically reduced [114] and their throughput is estimated at 60% but their fabrication principles are not as well-established as older designs.

Coles et al., [63] discusses the results of a chirally-coupled quantum dot within a suspended nanobeam waveguide structure. The principle of coupling is the same as the discussion in the above section (3.2), whereby a local circular polarisation of the waveguide $\mathbf{E} = \mathbf{E_x} + i\mathbf{E_z}$ perfectly maps the emission of a dipole oriented in the growth plane of QDs, whose (spin) quantum states are described as $|\psi\rangle = \alpha\,|x\rangle + i\beta\,|y\rangle$.

One of the more important facets of the waveguide architecture is the ability to control a noisy environment and subsequent behaviour of an embedded QD, which

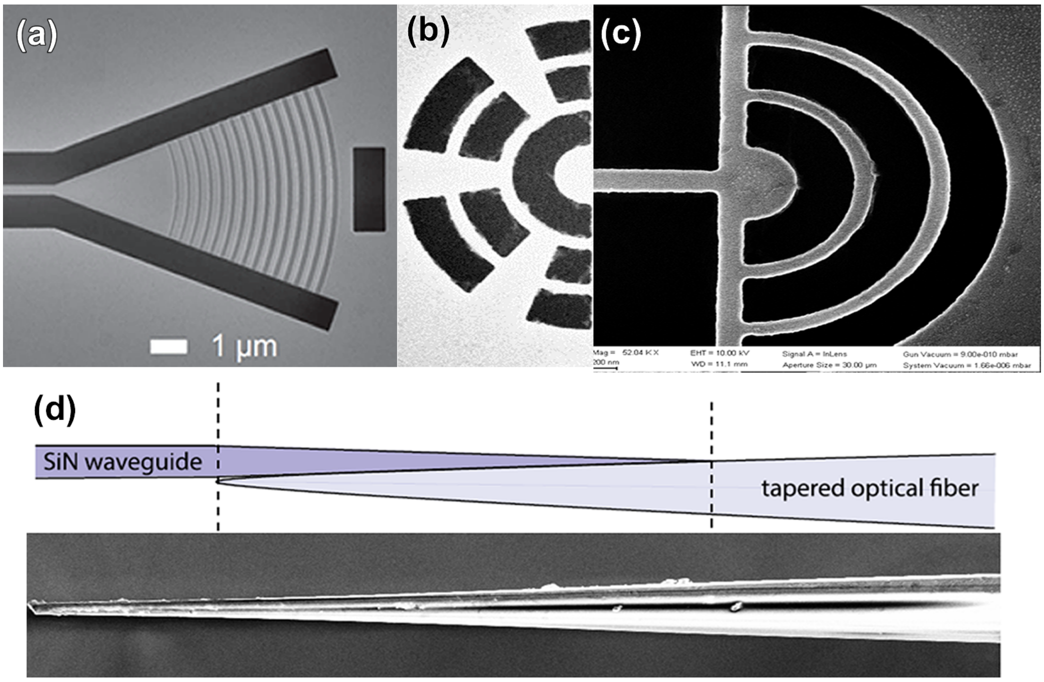

Figure 3.5: **Various light extraction devices from Sheffield** | Shallow-etch grating **(a)**, featuring theoretically high extraction efficiencies (60%) (X. Zhou 2018) and low back scattering. Design (b) is a modification of the standard double-annulus ring grating shown in (c). Part (d) is a tapered fibre, designed to couple to a second fibre which directly connected to single photon detectors.

is a generally considered more difficult in the suspended waveguide setting when compared to a QD in bulk system. This is often because the electrical control can be mediated in bulk QDs through construction of a Schottky diode device layering, whereas nanophotonics require a generic p-i-n format. However, spin control has been achieved in quantum dots embedded in the nanobeam in a p-i-n-i-n diode [1], whereby optical spin pumping allowed the embedded emitter to act as a single photon switch, providing control over the absorption and transmission of resonantly guided light, mediated by the QD's spin state. This principle is discussed further in chapter 6.

3.4 The W1 (defect) Photonic Crystal Waveguide (PhCWG)

Photonic crystals were first presented in work by E. Yablonovitch in the latter half of the 1980's. Initially, the purpose of this work was to suppress leakage of unwanted frequencies of light within lasers [115]. The first paper on the matter was in 1987 [116], which posited theoretical work on the forbidden propagation of optical modes. In 1989, [117], an experimental paper was published, involving a 3D crystal with mm-sized holes to suppress microwave wavelengths. Since then, photonic crystals have evolved exponentially, with a relevant branch of the research field being not just the suppression of unwanted modes, but selective enhancement of others. Such an example of this crystal is the W1 defect waveguide. The W1 photonic crystal waveguide is a fundamental structure of the on-chip nanophotonic world that has been studied and used throughout for over two decades. The potential slow-light, mode volume reduction (and thus potential for Purcell enhancement near the Brillouin zone (BZ) edge) makes the W1 a strong candidate for controlling (and enhancing) the emission of QDs embedded within. Such emission enhancement from slow light effects and mode volume reduction is encompassed by the Purcell factor [118].

Recently, a quantum dot coupled to a non-chiral mode of a W1 has been shown to demonstrate strong non-linear photon interactions which splits a scattered laser field into a (transmitted) bunched component and an (anti-bunched) reflected component [119]. Although the transmission window of the standard W1 is relatively broadband (<50nm), the slow light region sitting towards the very edge of the transmission window makes the more useful features of the W1 redundant in the context of spectral availability. By having such a spectrally narrow slow light region, the only benefits of the W1 rely on the β-factor. A series of modifications that the W1 can experience are presented in ref [120], all of which alter the symmetry of the crystal. In the context of spin-based directionality, traditional W1 defect photonic crystal waveguides (PhCWs) do not show large chiral areas. This is worsened by the fact that electric field intensity distribution only shows a modest overlap within these chiral areas. The consequence of this is that the W1 has a small probability to host chirally coupled emitters. Furthermore, the W1 chiral areas shrink to very small values, and altogether disappear very close to the band edge due to the generation of standing waves from the linear combination of the two travelling waves which exist due to reflections at band edge. There have been attempts to enhance the

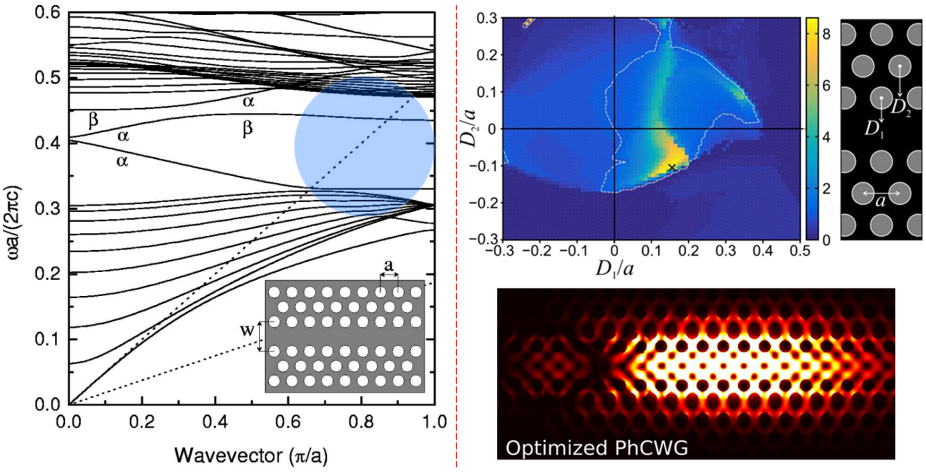

Figure 3.6: **Dispersion of the standard W1 defect PhC and modifications to this from ref [121]** | The blue circled region of the W1 dispersion is the region of interest, with the light line (the dotted diagonal) to the left side of the dispersion bands. The colour contour plot on the right indicates the amount of chirality when altering the 2D parameter space of D1 and D2, as seen in the black cartoon. The heat map along the bottom simulates a circular electric dipole at the most chiral point for the best D1 and D2 parameters.

chirality of W1 PhCs by modifying some of the parameters.

Ref [121] investigates a series of alterations that can be made to the W1 PhC in order to enhance the chirality and the overlap with the Purcell profile. In order to do this, changes in the lateral positions of the first and second rows of holes, along with alterations of the periodicity, can modify the crystal in order to generate chiral areas with larger local density of optical states (LDOS). Simulations have shown that it is possible to enhance the chiral areas (yield) to produce a theoretical maximum of 33% of the areas having chiralities above 90%. However, at the regions where the Purcell profile is greatest, the yield falls down to 15%, as the authors note. The unmodified W1 sees only 1.5% of its usable area with chiralities over 80%, and only 0.8% of the waveguiding area has chiralities above 90% (at ∼902nm). Therefore, modifications to the W1 to optimise for chiral effects are relatively impressive compared to the unmodified W1, but are still not as promising as the optimised glide plane structures discussed below. The authors also point out that such optimised W1s causes a flattening of the dispersion curve, increasing the spectral width of the slow light region, but this comes at the cost of breaching into multi-moding within the waveguide which is not ideal. Without these modifications, the W1 is all but useless for chiral integrated photonics.

3.5 The Glide Plane Waveguide (GPW)

The best design for a photonic crystal is one that demonstrates a variety of benefits. Ideally, a good photonic crystal should simultaneously support broadband transmission, with high LDOS (thus large Purcell factors), near-unity β-factors and the extra benefit of demonstrating strong chirality for circular dipoles (to which quantum dots can be approximated [122]). The optimised glide plane waveguide successfully demonstrates all of these criteria, and also allows for tapering[1] which can transform the modes of the glide plane to those of the NBWG mode. This is usually gradual and smooth along a linear gradient of adjustments to the PhC holes. Tapering between crystals usually changes the refractive index as slowly as possible to ensure the dispersion speeds of light are as close to one another as possible when the light crosses the ”boundary.”

---

[1] Tapering, in the context of adjoining two styles of crystal, refers to gradual adjustments to one crystal's hole size and/or period such that it eventually matches the pattern (and period) of a second crystal.

In this section, three iterations of the glide plane geometry are considered. First, the standard glide plane waveguide is discussed, including a brief mention of its origin, and areas in which the basic design can be improved. Such modifications form the topic subsection 3.5.2, which details the modified glide plane waveguide. The individual changes made to the standard GPW are presented along with results of theoretical simulation and some experimentally acquired chiral data. Finally, a completely novel structure is presented: the glide plane nanobeam (GPN). The properties of the GPN will be presented such as the dispersion diagrams and experimental transmission profiles from broadband QD (ensemble) emission.

3.5.1 The Standard GPW

The basic glide plane waveguide is constructed by taking the W1 waveguide and translating the holes of one side of the waveguide in the longitudinal direction (along the length of the W1’s central axis) by half a crystal period, to produce a glide-symmetric architecture. Figure 3.7 shows an SEM of an unmodified GPW alongside the band diagram for it. This is the GPW with no modifications, and it was first generated for GaAs in 2015 [123] (2011 saw a study of the glide plane geometry, but not in the context of integrated emitters [96]). In the original proposal, the glide plane section has a constant hole size across the full width of the crystal, along with a constant period. The GPW pattern is slowly tapered into a regular W1 to mitigate losses due to index and mode shape mismatch of the unmodified GPW and the NBWG terminators. A series of unmodified GPW designs were fabricated with the following details.

A central glide-plane symmetric crystal is adjoined and tapered to a W1 defect PhC. These W1 sections are connected to a broadened nanobeam waveguide, which nar-

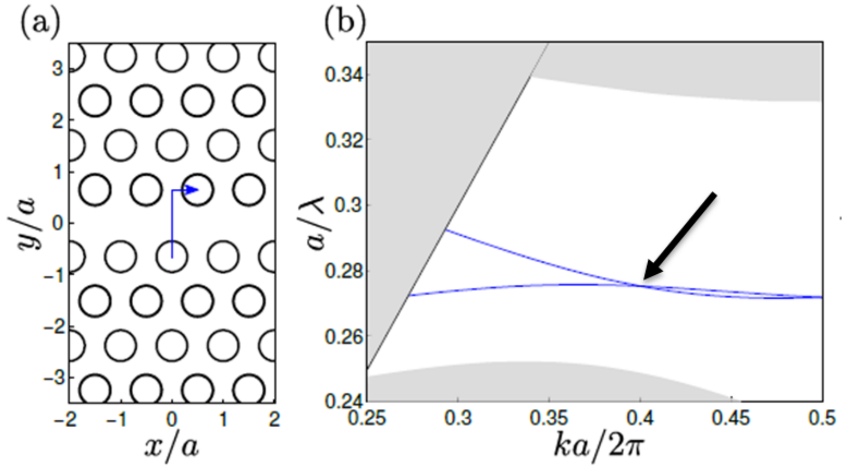

Figure 3.7: **Depiction and dispersion of the unmodified GPW** | (a): the unmodified crystal. (b): the GPW dispersion. The overlap in the dispersion between the two modes means that emitters within this spectral position can send light to either of these modes. Each mode has a different electric field distribution, and therefore even if the S3 Stokes' parameter is the same, the chirality will be highly perturbed by the mismatch of intensities.

rows down to a regular nanobeam size, all terminated by grating outcouplers. Hole sizes are altered across the series of devices in 2nm increments from a (target) diameter of 94nm to 146nm, which shifts the operational wavelengths of the crystal, and pushes it (upwards) towards the light line. Figure 3.8 shows a series of transmission spectra for a collection of unmodified GPW devices. The spectra are generated by exciting the grating outcoupler at one end of the device with a high power, above-band laser. Ensemble emission from a wide variety of (power-broadened) quantum dots is produced at one outcoupler and is scattered in all possible directions. Some of this ensemble emission travels along the device, through the GPW and beyond any interfaces of any two types of guiding element (e.g. the NBWG and W1) towards the other grating outcoupler. Light is subsequently scattered from the outcoupler towards the collection lenses in the setup, and a spectrometer records the transmitted spectrum. Different devices with slightly different parameters will have different transmission spectra (as discussed in section 2.2).

Unlike the W1, the "band edge" of the GPW is not in close spectral proximity to the slow light region. Such a cut off of the GPW transmission is where the light line on the dispersion diagram cuts the allowed modes of the glide plane defect modes

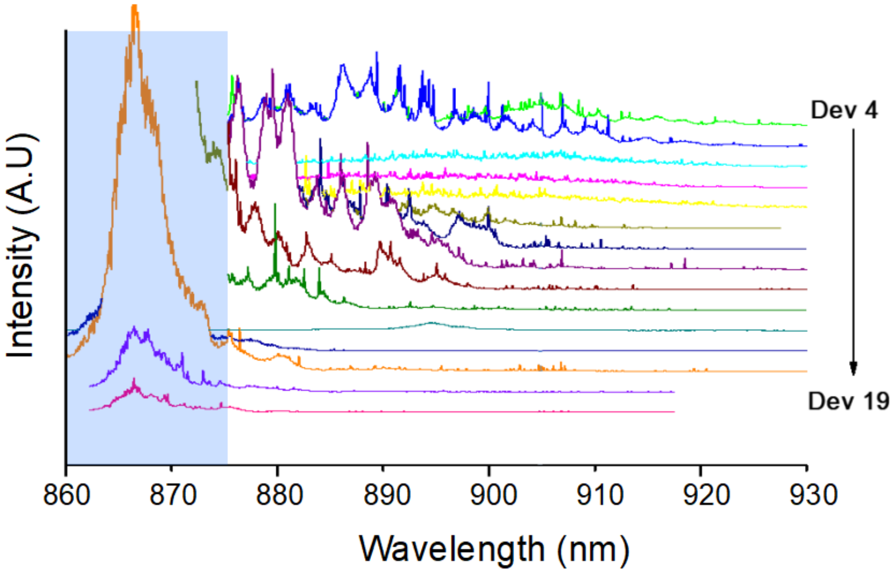

Figure 3.8: **Waterfall QD PL emission transmission series of unmodified glide plane waveguides** | Each μPL trace is obtained by shining the outcoupler of one end of a device with high above-band laser power, and collecting at the other outcoupler, forming the transmission data. The band edge of the devices can be seen to change as the device number increases, as there is little-to-no intensity at the higher device numbers towards the longer wavelength section. The blue-highlighted region comprises large intensities around 870nm, which is the wetting layer excitation of the sample. Some devices showed very minimal transmission, and this is discussed further in the next section, and outlined by figure 3.10.

represented by the two lines which overlap at the edge of the Brillouin zone, as seen in figure 3.9. The cut-offs for figure 3.8 are likely originating from the W1 band gap, which moves as the device parameters change from (as marked) device 4 to device 19, but may also be due to a large dispersion mismatch between the W1 and the corresponding GPW, as these two curves do not change similarly between parameter changes. The dispersion diagram of the unmodified glide plane reveals the potential problems with the design. Firstly, the crossing of the two modes towards the slow light region causes multi-moding to occur. The individual modes have different electric field profiles within the waveguide. While both of them may be inherently chiral, the combination of the two modes destroys any resemblance of useful circularity as the two field profiles are unique and do not overlap favourably. In order to overcome this, following the work presented in ref [123], a series of adjustments are made to the hole sizes and the hole periods, as discussed in section 3.5.2.

3.5.2 Modifications to the GPW

Three modified GPW designs have been considered for this work. Though three variations were designed, the majority of testing involved the second and third (final) iteration of edits to the GPW structure. Additionally, a separate style of device known as a glide plane nanobeam (GPN) is discussed in the next subsection, importantly as part of an adapter for the final GPW design. The first design involves a modification that is made to restore the desired directionality by lifting the mode degeneracy. This is performed by adjusting the lateral location of the holes. The resultant dispersion plot is shown in figure 3.9, where it can be seen that both modes are separate apart from the slow light edge where they theoretically meet at a perfectly flat point, known as the crossing point. At this crossing point, the group velocity of light is theoretically zero providing a technically infinite Purcell factor. In reality, imperfections to crystal fabrication, along with a finite size dispersion simulations presuppose infinite periodicity) provide a finite Purcell factor. With the current GPW designs, theoretical Purcell factors of up to 30 are calculated. The slow light region is designed to be aligned with the upper part of the lower dispersion curve of the W1. Alongside this basic modification, the GPW is slowly tapered into a standard W1 pattern by ensuring that the dispersion curves

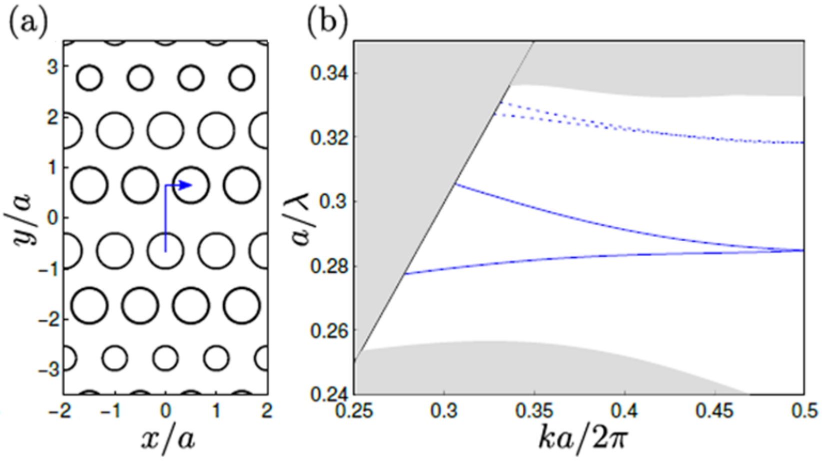

Figure 3.9: **Dispersion of a modified GPW, and the corresponding design.** | The original crossing point in the dispersion is lifted from un-modified glide plane. The row of smaller holes are the ones displaced. The altered sizes are discussed later in the text. Image from [123].

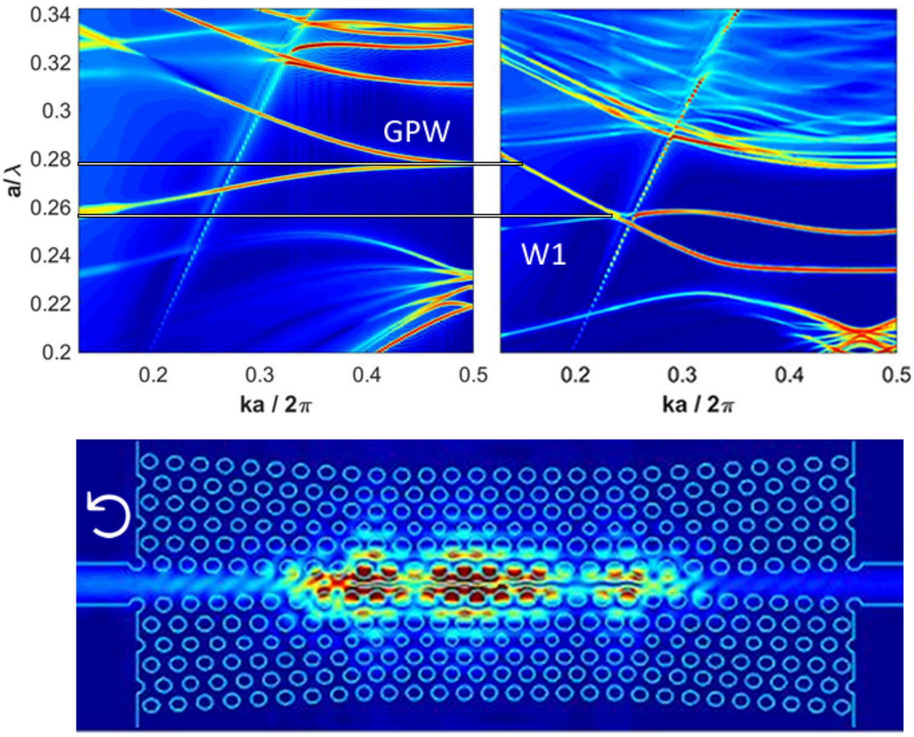

Figure 3.10: **Dispersion of a W1 and a GPW side by side, and an FDTD simulation of the adjoined crystals.** | The slow light region of the GPW and a similarly indexed region of the W1 are marked. The horizontal lines reaching to the vertical axis of a/λ correspond to the upper W1 cut off and the GPW slow light region. Using the resulting parameters, a design is simulated on the bottom of the figure, which shows a circular dipole source reflected between the interfaces of the GPW and W1. Any transmission is essentially allowed by the tapering between the crystal varieties and the subsequent reduction of the efficacy of the simulation caused by the limited periodicity of the crystal. Band structures generated by C. O'Rourke in FDTD, bottom simulation performed by H. Siampour in FDTD.

of both types of crystal energetically match as well as possible. Not only must care be taken to ensure that the slow light region of the GPW does not sit within the band gap (i.e. between the dispersion curves) of the W1, but one must also ensure that the gradients of both crystals are similar to avoid reflections at interfaces. The W1 is then adjoined into a broadened nanobeam to maximise adiabatic coupling, terminated by grating outcouplers.

Without consideration, arbitrary connections of W1 and GPW dispersions can result in a complete lack of spectral overlap between the dispersions. The importance is outlined in 3.10, where a mistaken wafer thickness altered the necessary period and hole sizes from the implemented design. Below the two (misaligned) dispersions, a simulation is shown of a left circularly polarised source at a chiral point of a

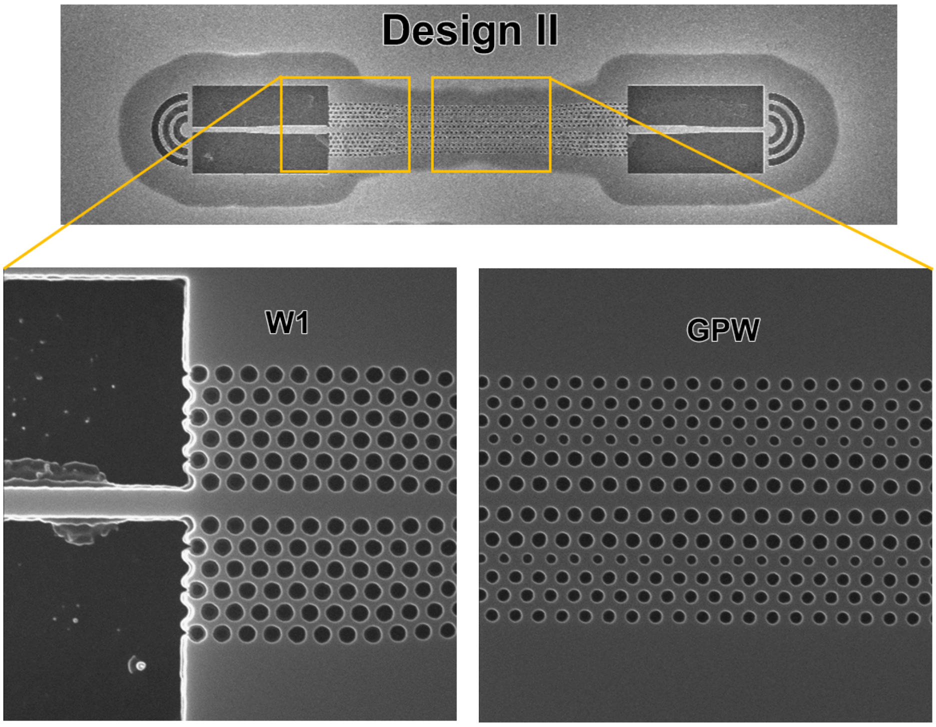

Figure 3.11: **Scanning electron micrograph of a GPW design with a W1 PhC defect adapter** | Named design II, the size of the first row of holes remain unaltered relative to design I, which only lifts the dispersion's degeneracy as seen in figure 3.7 as this is a modification made to the later designs. The GPW pattern is adiabatically tapered to match the W1 periodicity, which has the same periodicity. The residue surrounding the nanobeam area in the W1 section is removed before diode bonding.

modified glide plane waveguide. Because the dispersions are not mode matched, light is reflected to create unwanted cavity-like effects.

A small modification to the first design is employed to produce further improvements. As well as laterally displacing the etched holes for lifting the degeneracy of the dispersion curves, the hole sizes are also adjusted. By increasing the size of some of the rows of holes, an even greater potential Purcell factor can be achieved by adjusting the mode volume (to the diffraction limit) of the waveguide. This design features the same tapering into the W1 as before. This second design in shown in figure 3.11. Some chiral QD data is presented for this design, although it was not studied thoroughly beyond this point. The data is shown in figure 3.12, which shows a series of chirally-coupled QDs at 3T, all at different energies, from a variety of devices. Non-chiral QDs were present, they are just not shown. The third design features a fully optimised glide plane waveguide that does not feature a W1. Shown next to a schematic the second design is design 3, which features a central glide plane geometry, which is coupled first into a secondary GPW which acts as another mediator for the glide plane nanobeam adapter. With all three elements, the benefits of the modified GPW device are met with an efficient adapter to ensure the light effectively couples into the terminated nanobeams. Of the photonic crystal section (between the two interfaces of the GPN and the NBWG), 16% of the length is made up of GPN, and 20% is the altered GPW adapater. This leaves 44% of potential crystal space within which a QD could be found. It is in this style of design that large Purcell enhancements have been achieved for both chiral and non-chiral QDs, with efficiently extracted photons .

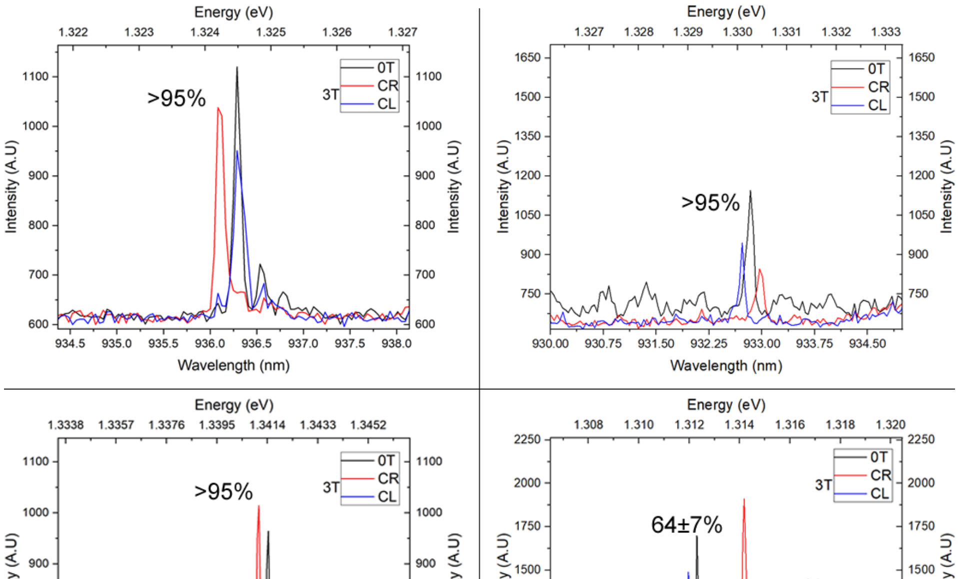

Figure 3.12: **Chiral QDs collected across different GPN devices** | 808nm laser light is directed onto the GPN from above, and the subsequent PL is collected at each outcoupler (Collect Right/Left - CR/CL) under a both a magnetic field and at 0T for reference. The chiralities are marked, and were calculated by studying the integrated areas under the curves and by entering the values into equation 3.2. The chiralities of the GPN are not as impressive here as they are in the GPW. This is both due to the band gap obfuscating the spectral availability of QDs, and the intrinsic chirality being less.

3.5.3 The Glide Plane Nanobeam (GPN)

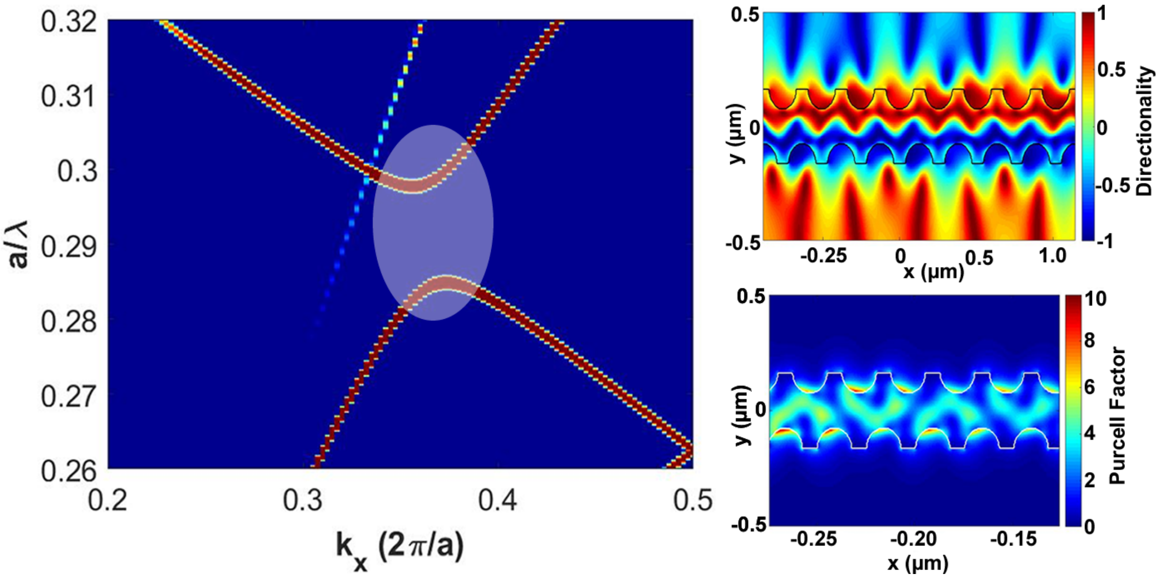

Figure 3.13: **Dispersion of the GPN (left) alongside the directionality (top right) and the Purcell profile (bottom right)** | The blue-circled area is the spectral region for which the two rightside diagrams are valid. The directionality is anti-symmetric about the central axis. The strongest field strengths (which directly correlate to the Purcell profile) occur either in the air holes or very close to the surface, both of which are essentially useless for embedded emitters. Dispersion simulation performed by H. Siampour in MPB. Purcell and directionality profile simulated by C. O'Rourke in FDTD.

The glide plane nanobeam is a design motivated from the tapering used in design 3, described in the previous section. The principle of the design is simple, and is described as a nanobeam waveguide, perforated or serrated with a glide plane geometry. The design has a hole radius that is 35% of the period, and the device is terminated by standard nanobeams and grating outcouplers. The motivation of study for this device was to investigate the behaviour of the GPW adapter in an isolated setting. Transmission measurements were performed to experimentally study the band gap of the device, in tandem with a basic characterisation studies of the achievable chiralities of the design. A map of directionality[2] along with the band structure is presented in figure 3.13. It can be seen that the GPN band structure differs from the regular GPW insofar that two modes do not meet at a slow light region. The GPN is more analogous to the W1, with a band gap and a slow light region near this location. Results of experimental transmission measurements using the same method described for the GPW studies are provided in figure 5.3 of chapter 5.

---

[2] Directionality, chirality and the degree of circular polarisation are effectively the same metric here. An emitter which only sends one handedness of circular polarisation uniquely along one direction is said to have a chirality, directionality and S3 parameter of unity.
Chirality, in general, refers to a wider, spin-dependent interaction with the mode polarisation

In many devices, a clear "band edge" is seen, with some devices exhibiting a clear opaque spectral window. All devices should show such an extinction region, where light is scattered from the crystal, but often this region is beyond the detection capabilities of the silicon detectors used in this work, or it is beyond the emission range of the QD ensemble. It was possible to identify multiple chirally coupled QDs within the device, with a distribution of narrow linewidths. Figure 3.14 shows some preliminary data of QDs with varying chiralities across different spectral regions. Unlike the case for the modified GPWs, transmission measurements were not used to reverse-engineer the band structure of each fabricated device on the sample, and

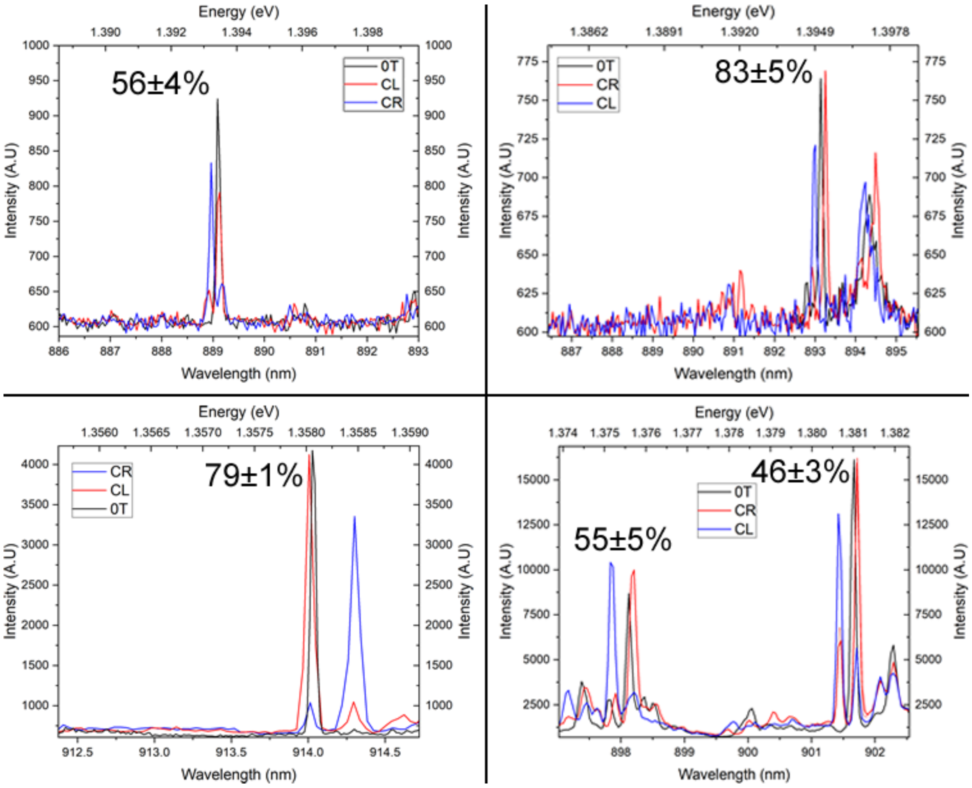

Figure 3.14: **Chiral QDs collected across different GPN devices (bottom right)**| Data is collected at each outcoupler under a single magnetic field, and is also collected at 0T. The chiralities are marked, and were calculated by studying the integrated areas under the curves and by entering the values into equation 3.2.

so slow light regions were not identified to faithfully study the possible Purcell enhancements through shortened lifetimes. More directional emission is presented in section 5.2 of chapter 5.

3.6 Discussion

From the summary table presented in figure 3.15, the benefits of the glide plane waveguide variants are clear: a modified GPW promises a high β, broadband Purcell-enhancing with strong chirality. Furthermore, with the use of appropriate GPW and GPN adapters, GPW modes can be coupled almost adiabatically into a standard nanobeam waveguide, which can act as a universal transport system for on-chip guided light. No passive device currently developed, such as a topological photonic crystal presented by Mehrabad et al [111], the modified W1 PhC presented by [121], or any general passive device, manages to capture all three main features of the large $C_{L/R}$, β and the broadband availability of slow light. The glide plane waveguide, in the next chapter, shows improvements on the chiralities provided by previous studies of nanobeam waveguides, and in chapter five is presented alongside record-breaking Purcell enhancements of a QD in a waveguide structure.

Waveguide/Device design	**Description**	**Advantages/Disadvantages**	**Schematic/SEM**
Standard nanobeam	**Suspended, air-clad nanobeam waveguide**	- Good chirality (34% >90%) - Vanishing Purcell - Low Beta (70% at C-point)	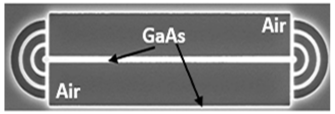
W1 PhC	**Row of holes removed from 2D photonic crystal**	- Very low chirality (0.8% >90%) - Moderate Purcell (~3) - Near unity Beta (99%)	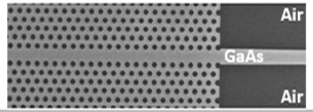
GPW design 1	**Unmodified GPW, adjoined to W1 + NB**	- Chirality destroyed from crossing modes - Moderate Purcell, no chirality at band edge - High Beta (99%)	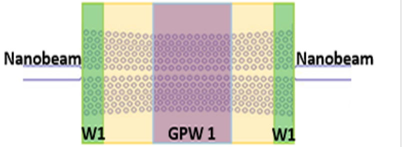
GPW design 2	***Design 1 and*** **hole position shifted from waveguide centre, adjoined to W1 + NB**	- Chirality restored - Moderate Purcell - High Beta (99%)	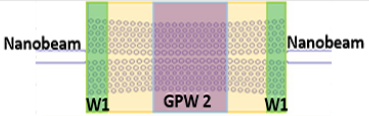
GPW design 3	***Design 2 and*** **increased hole size for decreased mode volume + second GPW taper + GPN + NB**	- 38%: >90%, 23%: >90% - Large Purcell (~30) - High Beta (99%)	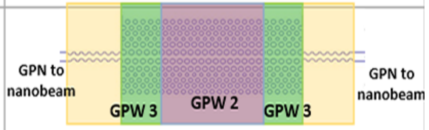 GPN to nanobeam GPW 3 GPW 2 GPW 3 GPN to nanobeam
Glide plane nanobeam	**Perforated nanobeam waveguide design, hole size 35% of period**	- 32% of device has chirality >90% - Moderate Purcell (~2-8) - Moderate Beta (83%) - Band gap	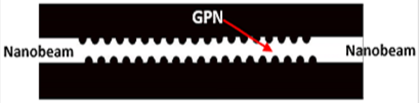

Figure 3.15: **Summary of the devices mentioned in this chapter** | Red, blue and green refer to poor/undesired, moderate, and good/desirable properties respectively. A description of each design, alongside the amount of chirality, the Purcell enhancement and the β-factor is provided in that order in the third column. The strength of the GPW over the standard nanobeam and the GPN is size of the area for which the chirality is beyond 95%. Each design has either an SEM or a representative diagram of the devices in question.

This page is intentionally left blank

Chapter 4

Spin to Path Conversion of QD Excitonic Emission

In chapter 3, a variety of photonic structures were presented, some of which were shown to have large Purcell factors for a spectrally broad slow-light region within their dispersion diagrams. Although the broadband Purcell-enhancement has become a potential primary focus to the designs, the initial goal for some of the presented devices, such as the modified glide plane waveguides, was to offer large chiral areas. Such areas occur when the probability that a randomly placed emitter within the device shows more than some percentage (80% or 90%, as previously presented figures of merit) directional coupling. First, in this chapter, how chiral contrast can be determined is shown, with a short tangent into the specific data analysis method of how to calculate the chiral contrast using curve fitting. Next, a description of how the devices are preliminarily characterised and subsequently probed for chirally-coupled emitters, with a discussion of how the calculation of the QD exciton g-factor proves the magnetic interaction between an externally applied B field and the QD spins. Some results on simple chiral behaviour for QDs within both the fast and slow light regions of the glide-symmetric designs will be presented and compared to previous studies of standard nanobeams and W1 defect PhCs.

4.1 Determination of the Chiral Contrast

Most of the experiments performed to determine the chiral contrasts of either QD of charge states are done with (above-band) PL using a linearly polarised laser source. The principle of operation is shown in figure 4.1, which depicts a scheme where light is directly shone onto a device's centre. Light from the embedded QDs travels accordingly to either one of the outcouplers whereby it is collected and subsequently analysed. The contrast is principally calculated using equation 3.2, but often adjustments have to be made in order to accurately and precisely obtain a value. These methods are discussed in the next paragraph. The strength of the magnetic field which causes the energy separation, so long as it is enough to overcome any fine structure splitting (of energy E_{FSS}) for the neutral exciton, should not influence the chiral contrast itself (for example, a higher field does not imply a higher contrast). An idealised chiral QD emits only one colour in one direction.

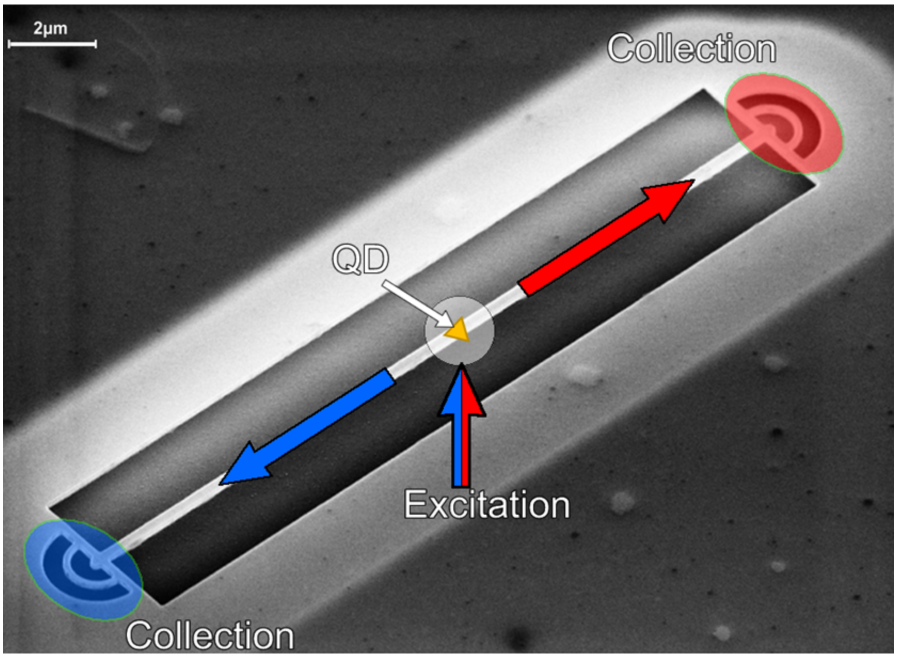

Figure 4.1: **Principle of exciting an emitter and collecting light from outcouplers in a nanobeam waveguide** | This depiction describes either PL or resonant QD excitation for spin-to-path conversion. Incident light excites one of the QD spin states, as marked by the blue/red arrow and light is emitted in one direction or the other depending on the polarisation of the light associated with the QD spin, corresponding to blue or red, depending on what colour was used to excite the system.

Good QDs possess a narrow linewidth which is much smaller than the individual pixel size of a CCD when connected to a high order grating spectrometer (e.g. 1800 lines/mm), but the noisy charge environment can broaden the transition linewidth which, when considered with potential lack of pixel-perfect alignment, appears in experiment as a broadened Gaussian curve. If the transition linewidth could be contained within one pixel, the QD intensity could be characterised as the single pixel brightness. However, this almost never happens, and neither is the number of counts symmetric about the brightest pixel. Such behaviour impacts the calculations of chiral contrast, and accurate calculation of this parameter is of great importance when characterising the proficiency of chiral waveguides. In order to appropriately implement the value for contrast presented in equation 3.2, either a calculated integrated area can be used, or the individually binned pixels within appropriate limits can be summed together. Such a method is shown in figure 4.2, whereby the fitted curve overlaps multiple data points (CCD pixels). In part **(a)**, μPL from a single QD is shown and the use of the peak height would not provide the full picture. The difference is demonstrated in part **(b)** of figure 4.2. The chiral

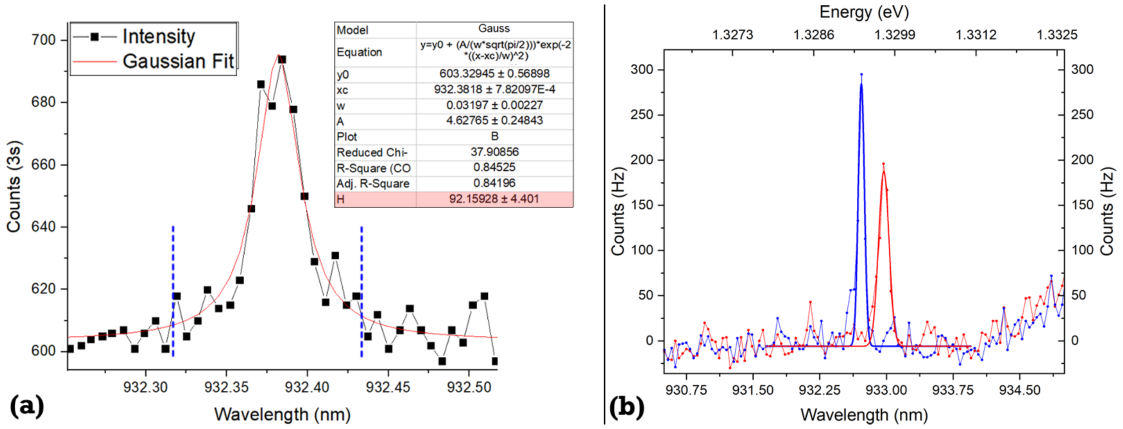

Model	Gauss
Equation	y=y0 + (A/(w*sqrt(pi/2)))*exp(-2 *((x-xc)/w)^2)
y0	603.32945 ± 0.56898
xc	932.3818 ± 7.82097E-4
w	0.03197 ± 0.00227
A	4.62765 ± 0.24843
Plot	B
Reduced Chi-	37.90856
R-Square (CO	0.84525
Adj. R-Square	0.84196
H	92.15928 ± 4.401

Figure 4.2: **(a): QD PL and a Gaussian fit to the QD peak with extracted fit parameters of curve area and peak height, (b): μPL spectrum of a mildly chiral (split) pair of lines to demonstrate the importance of using the calculations presented in the text** | The vertical blue dashed line in **(a)** indicates exemplary boundaries where the summation of individual counts would take place for the calculation discussed in the text. The red and blue data are separate spectra collected from two exposures under the same conditions. By taking the appropriate ratios of the integrated areas, the calculated chirality for the data in **(b)** is C=-6%. Conversely, the chirality for merely taking the extracted peak height (labelled as H in **(a)**) is 20%.

contrast when studying the fitted peak areas of these curves is $C_{Area} = -6.3 \pm 4.0\%$. When taking merely the largest of these data, the contrast is drastically different, at $C_{Peak-Height} = 18 \pm 4\%$. The contrast when performing individual summations within the blue-dashed line estimates is very similar to using the integrated area, with a value that overlaps with the error bars. All chiral contrasts in this work are calculated by studying the fitted area of the Gaussian curve.

4.2 Chiral areas of the Glide Plane Waveguide

As discussed in the previous chapter, one of the fundamental promises of the modified GPW is the chiral area that they possess. It can be predicted that nearly 50% of emitters embedded within the devices should possess a chirality of above 80%. Shown below is experimental data to modestly support this statistic, showing that while the exact distribution does not quite meet theoretical expectations, it still surpasses the results shown in [63] and [100]. Integrated areas were used to measure the contrasts of many QDs, at a variety of wavelengths. Their selection was pseudo-random, as QDs for analysis had to be spectrally isolated at some magnetic field.

Additionally, the decision was made to only include QDs that were identifiable which appeared either at both outcouplers, or could be seen at 0T above the crystal (or both of these).

Shown in figure 4.3, alongside the distribution of data collected by Price et al., is is a bar chart showing the chiral contrast of around fifty QDs found inside glide plane waveguides. The red distribution curve is a skewed distribution fit to indicate the % of QDs with a chirality greater than 70%. The most striking difference between the two QD distributions is the vastly smaller number of QDs with low chiral contrasts in the GPW. This can be explained by simulation, which shows that the non-chiral areas occupy a very small region in the active region of the modified GPW.

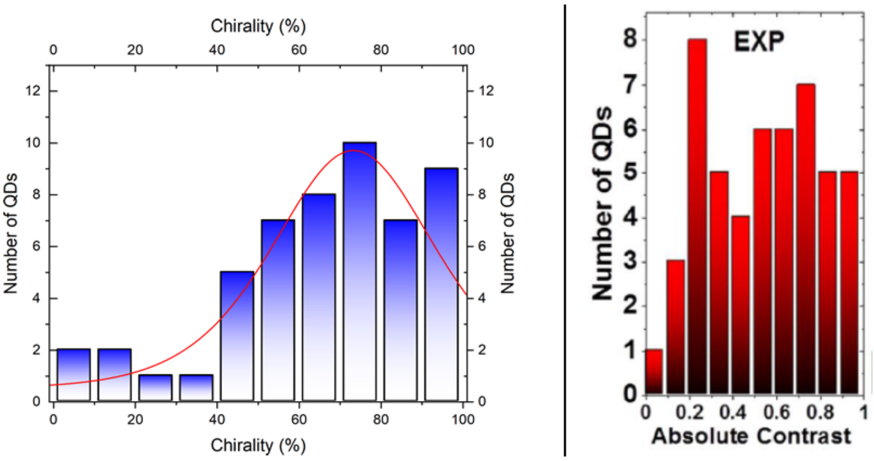

Figure 4.3: **Comparison of experimental distribution of QDs in the GPW and NBWG** | Plotted on the left are data for the glide plane waveguide. Contrasts are obtained at various magnetic fields, from QDs ranging in emission wavelength from 870nm to 934nm, across a multitude of devices with slightly different fabrication parameters. The red curve over the top is a skewed distribution which indicates that 50% of QDs have a chiral contrast of at least 70%. The right hand side shows data collected for QDs within a nanobeam waveguide from [100].

4.3 Spin Readout of QDs Inside Nanophotonic Waveguides

The characterisation of samples often begins with a study of nanobeam waveguides in order to determine whether QDs on the sample are of an acceptable spectral quality, and whether they can be electrically controlled. The qualification of "acceptable" depends on the experiment one wishes to carry out using the QDs. If the QDs are to require resonant excitation for measurements of (spin) lifetimes (see chapter 5), coherence or entanglement generation, they need to be spectrally very narrow. Alternatively, the restriction on their linewidth is not as stringent in a study of the chirality of a nanophotonic architecture. Moreover, nanobeams are often considered for directional readout as they have much higher chiral areas than the W1, as discussed in chapter 3, and therefore W1s would not be fabricated for chiral investigation. Additionally, there is little to no dependence of the transmission of light through a nanobeam unlike the W1, as dispersion lines have an approximately constant gradient in the nanobeam setting.

Applying a magnetic field to QDs in a nanobeam is used to determine the magnetic

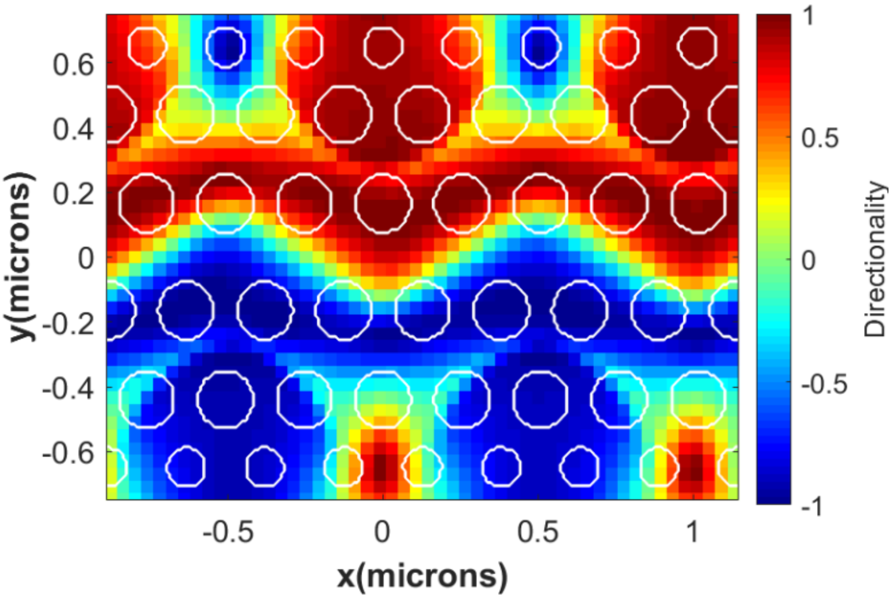

Figure 4.4: **Coarse FDTD simulation of electric field polarisation within the modified GPW, design III** | The colour map indicates the strength of the directionality ranging between 1 and -1 across the crystal. The white circles are etch holes, and no emitter can be found within them. Even when subtracting this area, 39% of the area should house > 90% chiralities.

response of the QDs. Determining if the QDs respond appropriately (by experiencing an expected Zeeman splitting with no losses in total emission intensity) is a useful avenue of investigation should the photonic crystal designs of interest (glide plane waveguides) not show chiral QDs. Successful nanobeam tests will determine whether it is the behaviour of the dots or the photonic structure that is inhibiting hypothetical detection of chiral QDs. The study begins by ensuring a nanobeam showstransmission of PL from both outcouplers, in a similar fashion to the methods described in section 3.5.1. The PL should not only be vertically emitted along the same line as the excitation direction, but also should be directed along the length of the device, towards the other outcoupler, and back out into free space. The comparison of both the vertically emitted and device-transmitted signal should show that the nanobeam is etched smoothly and that the wafer thickness is reasonable (a waveguide that it too thick or thin will cause mode leakage). Naturally, the transmission test is also a measure of the outcoupler behaviour, but as is discussed previously in regards to figure 3.10, fabrication errors with the thickness of a waveguide membrane, for example, would lead to obvious dips in transmission intensity.

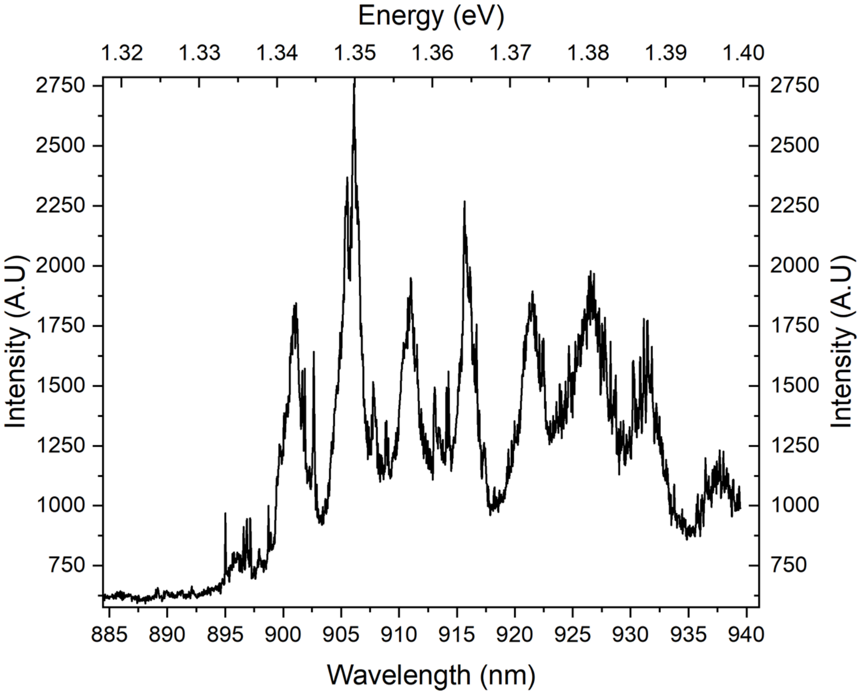

Figure 4.5: **PL transmission along a standard suspended nanobeam waveguide.** | There is little spectral intensity dependence apart from shorter than 900nm, which is due to a spectral filter to remove the wetting layer PL. The brightness oscillations are due to Fabry-Perot interference due to the outcoupler reflections. The separation of the peaks (known as the free spectral range) allows for a calculation of the refractive index, as shown in equation 4.1.

This study is mostly qualitative, as spectrally broad transmission is sensitive to alignment, since there is a slight angular dependence on the wavelength scattered from the (diffraction) grating couplers. However, it is possible to extract the free spectral range (FSR) of the device, by studying the separation in the peaks of the transmission spectrum, such as that shown in figure 4.5.

The FSR can is presented in equation 4.1, which describes the peak-to-peak separation as a function of the weak cavity length and the refractive index.

$$\Delta\mu_{FSR} = \frac{c}{2n_g L} \tag{4.1}$$

For the nanobeam waveguide, the dispersion is approximately flat, meaning that n_g has no frequency dependence. For devices that do, the separation in the fringes changes to reflect the dispersion.

In short, testing PL transmission through a coupler-nanobeam system tests both the etch quality of the couplers along with the membrane thickness of the suspended layers. If SEM images appear clean from dried chemical (cleaning) contaminants and nanoscopic dirt deposits, nanobeam transmission is usually successful. Figure 4.5 shows the transmission of QD PL along a nanobeam. Once this has been generated, an observation of individual QDs within the nanobeam can be observed.

The 70% β-factor of the nanobeam waveguides allows for the detection of quantum dots without using the grating outcouplers at all, much like QD searches in bulk, as 30% of the light is emitted into free space. Overlapping the collection and excitation path and scanning across the nanobeam allows for the identification of bright QDs. If such QDs are narrow, then these are studied in both outcouplers to check for chirality. Part (a) of figure 4.6 shows an example of two QDs at zero magnetic field seen at both outcouplers and above the device. The lines in this device may be chiral, insofar that each exciton component travels in opposite waveguide directions, but it is not provable unless a magnetic field is applied. Part (b) demonstrates the collection of light in a GPW device by collecting the light directly above the crystal

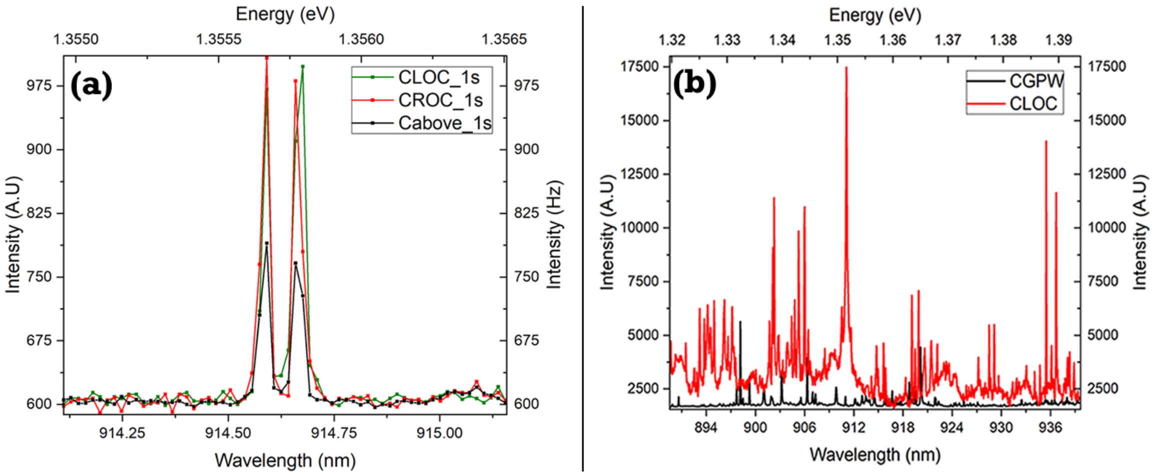

Figure 4.6: **(a): μPL for a QD collected directly above it, and from either of the GPW device outcouplers. (b): Broadband collection μPL demonstrating the effectiveness of grating outcoupler collection** | One second exposures for all three collection regimes show the potential β-factor of the QDs within the nanobeam. From the single QD in **(a)**, there is very little intensity change between the outcouplers, and this QD could host any level of chirality. **(b)** shows that generally emission is way brighter when collected from an outcoupler, in red, compared to whent he light is collected from directly above the excitation location, in black.

and at an outcoupler. In terms of QD searches, it would be difficult to study above the crystal to find the dots, as the light preferentially couples very strongly to the waveguide, and hence towards the outcouplers. This is in contrast to part (a) of the figure, where the QD lines have an appreciable intensity out of plane of the device. Without the magnetic field, a chiral QD will still emit opposite circular polarisations in different directions. However, there is no way to discern these polarisations (due to the outcoupler behaviour), it is not possible to distinguish any chiral contrast.

Once a QD's emission is located at either outcoupler, a magnetic field can be applied to split the transition. At this stage, whether the QD line is a neutral or charged exciton does not matter, as both split similarly in the magnetic field. The revealed chiral contrast should be similar in magnitude across both outcouplers, as each of the circular transitions couple to the opposite propagation directions along the waveguide/crystal. The type of exciton cannot be deduced through noting the chiral contrast within a magnetic field, however. This is because a chiral QD (that is, a QD at a C-point) in a magnetic field will be indistinguishable from a QD at a point in the waveguide where the electric field polarisation is purely linear (i.e. towards the middle of the waveguide, at an L-point). In order to deduce the specific

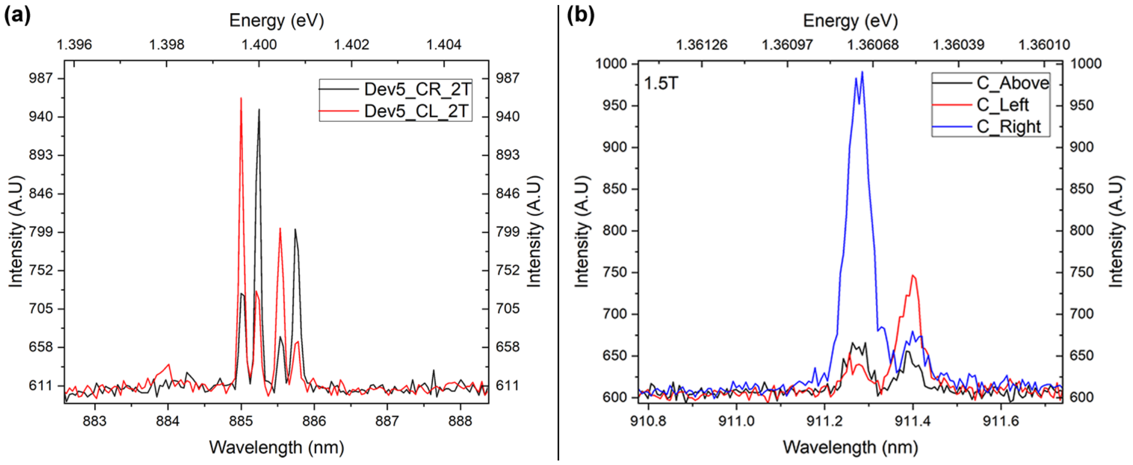

Figure 4.7: **Symmetric (a) and asymmetric (b) chiral QD data** | Two QDs are present in (a), each split by a magnetic field of 2T. The data of (b) shows the QD emission collected above the waveguide in black. Red and blue show different chiral contrasts when collected at different outcouplers, even though the QD is the same.

exciton state, there are many possible avenues [1], such as evaluation of the exciton g-factor, power/saturation dependences, charging thresholds and relative energies to the neutral exciton, or a map of the polarisation of the QD when collecting light not coupled to the waveguide.

Sometimes, the magnitude of the chiral contrasts between outcouplers is not symmetric. The asymmetry is something many emitters experience with differing amounts. This asymmetry manifests itself when studying different outcouplers, meaning that either one transition is dimmer or brighter than expected when viewed at the other end of the device. An example of this is shown in figure 4.7. Unfortunately, there is no obvious solution to this problem in terms of experimental approach. Reversing the sign of the magnetic field switches the energies at which each spin state appears, meaning the $|\Uparrow\downarrow\rangle$ state, for example, possesses the energy in a negative magnetic field that the $|\Downarrow\uparrow\rangle$ state possesses in a positive magnetic field. However, because the spin states themselves are not flipped, no additional information on spin states is obtained by studying only one outcoupler.

Coles offers a possible explanation for the asymmetry phenomenon [113]. The consideration is that the lack of perfect circularity of the dipole (even under an applied magnetic field) can cause the asymmetries. This phenomenon is only possible in a system with back reflections (such as those produced by grating outcouplers, or

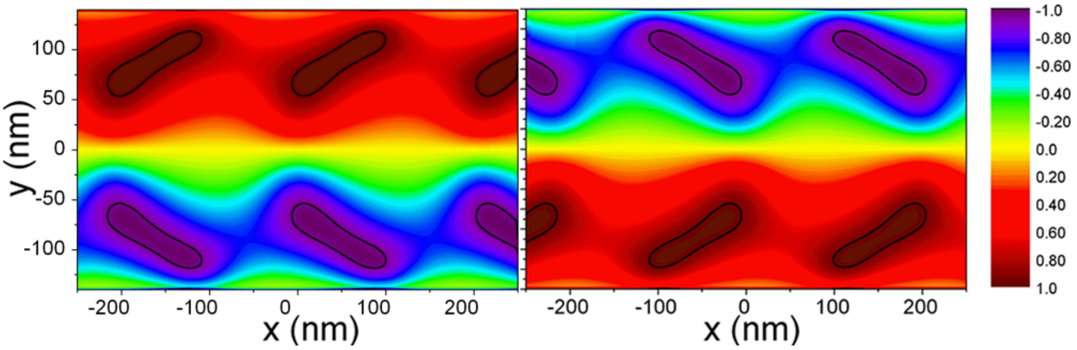

Figure 4.8: **Contrast of elliptical emitters for an ellipticity magnitude of 0.1π** | A birds' eye view of the field in the nanobeam. The anti-symmetry between both plots are for $\pm0.1\pi$. Importantly, there is no overlap between the two plots when they are overlaid. The result are seen in figure 4.9.

---

[1] a full literature review is beyond the scope of this chapter, but the references attached to each avenue provide a discussion of each study

index mismatches between different types of crystal), and is a consequence of the elliptical polarisation of the emitter and the electric field intensity profile. Simulations were performed to study the effects of having an elliptical emitter inside terminated waveguides. The field profiles when studying each emission direction produce different values for the contrasts extracted from the opposite sides of the device. The resultant of left and right contrasts are shown in figure 4.8, which displays the regions in which emission is expected to be asymmetric. For perfect symmetry, the profile in figure 4.9 should be uniform, as the summation of C_L and C_R should be 0 (as C_L = -C_R). The stronger the ellipticity of the emitter, the larger the asymmetry becomes, until the phase of the ellipticity reaches 0.5π. The consequence of this phenomenon is that the devices are best studied under the outcoupler that has the largest chirality. The best workaround to this problem is to generate devices with little back reflections so that emitter ellipticity does not work with the distorted field profile generated by the Fabry-Perót fringing, by using low-reflection gratings and well-matched group velocities between different types of adjoined crystals. It is worth noting that it is still entirely possible to obtain spin-based directional emission in this regime, where a “C-point” is simply a point where the ellipticity of the

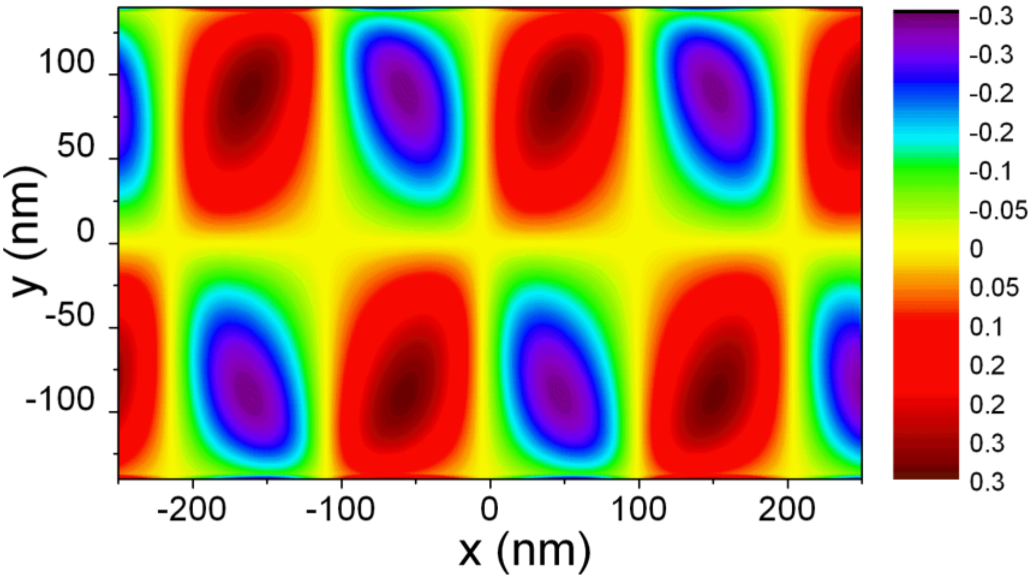

Figure 4.9: **Resultant (summed) phase plots of an elliptical emitter** | For a non-zero phase difference, this plot would be empty. The $\delta_{phase} = 0.1\pi$ produces ellipticities of 30%.

QD is matched by the spin the electric field profile possesses. This asymmetry will be discussed in chapter 7, which will present directions for further study of this phenomenon.

The characterisation and detection of chiral QDs differs slightly in glide plane waveguides. The large β-factors mean that QD searches cannot take place above the crystal. Any QDs visible when searching above the device indicate that they are not well-coupled to the waveguide, as the nominal β-factors are 99%, with little deviation across the surface profile. Shown in figure 4.10 is a plot of a series of β-factors of emitters at a series of locations. At each location the amount of power passing through a simulation monitor either side of the crystal (after a few periods) is measured relative to the total output, and the β-factor is thus determined by taking the ratio of the two. It can be seen that the β-factor is almost constant for the majority of emitter locations, and locations too close to the etched holes' surfaces are not viable locations anyway due to surface charge effects. Importantly, high β-factors

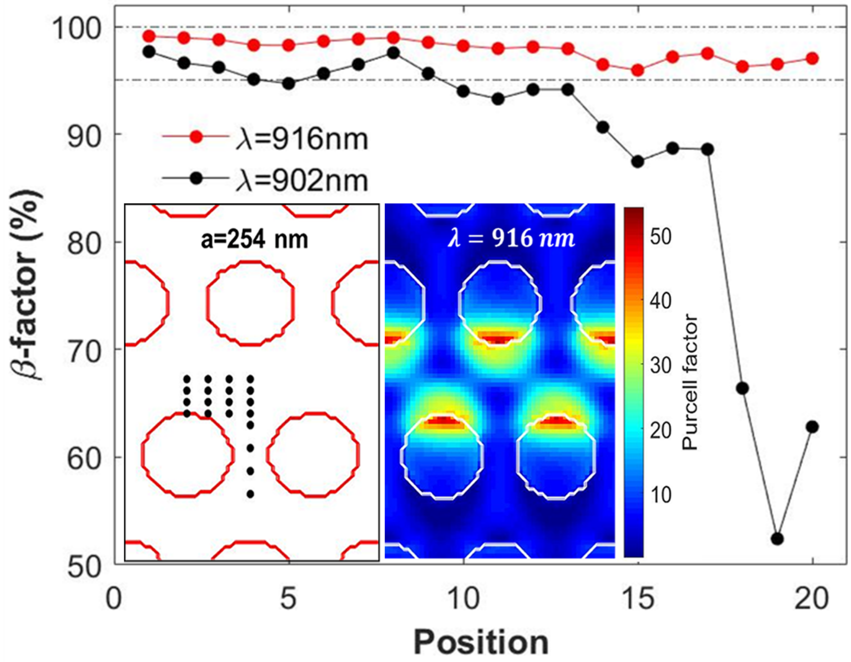

Figure 4.10: **Plot of the β-factor with respect to the lateral QD position within a waveguide. Simulations performed by H. Siampour** | Shown for two different wavelengths, the beta factor was calculated by measuring the fraction of total transmitted power along the waveguide, relative to the system input power, which is a known parameter of the simulation. The coloured plot shows the Purcell profile of the waveguide. The beta factors of emitters at different positions along the x-axis labelled 1 → 20 correspond the small black circles in the bottom left inset.

correspond to areas of high electric field intensity and chirality. Chiral QDs are more easily found inside GPW devices than in the nanobeam waveguide, so much so that many of the QDs found for the lifetime measurements of chapter 5 were chiral as well as close to the slow light region.

4.4 Measurement of Exciton g-factor

Applying a variable magnetic field can allow for the extraction of the exciton g-factors, as described in equation 2.2 from section 2.5.2. Figure 4.11 shows the energy splitting of two Zeeman split lines of a QD collected at one outcoupler. The splitting of the line, in accordance with equation 2.2, consists of a diamagnetic (quadratic) component and the linear Zeeman component. Since both states experience the same diamagnetic shift, subtraction of the lower energy component from the higher

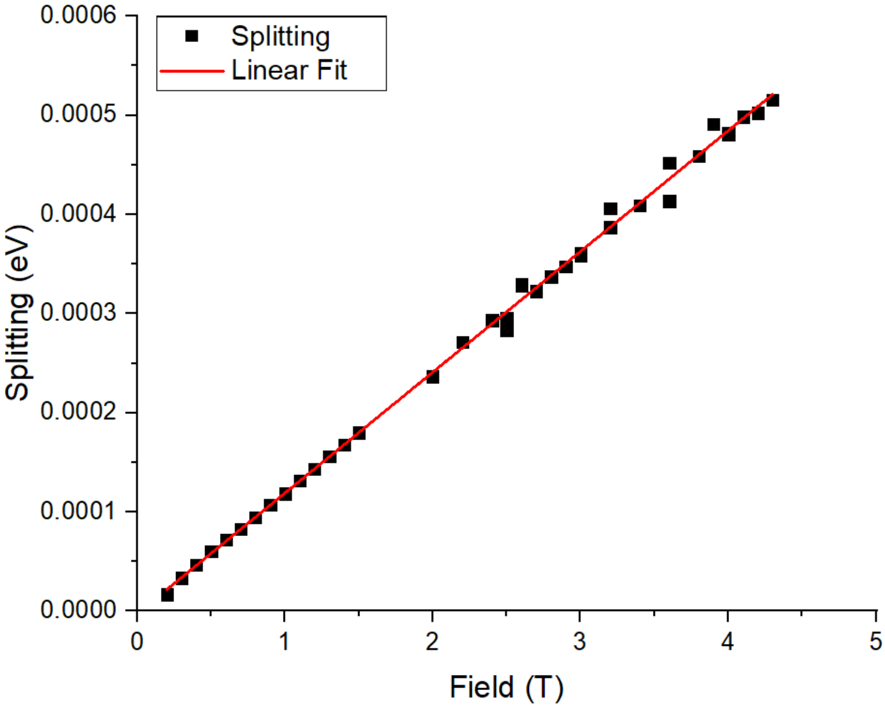

Figure 4.11: **Zeeman splitting vs. magnetic field** | A series of PL peaks are fitted, and the central positions are found for each of the plots. The linear relationship is generated by finding the difference between both components' fit. Consequently, the diamagnetic shift is eliminated, as it affects both components equally. The g-factor for this QD was 2.10±0.02.

energy component for each magnetic field value removes the need to fit for the γB^2 term, and the Zeeman-split lines only experience a relative linear separation. The measurement of the gradient of the splitting between two transitions at multiple fields allows for the determination of the exciton g-factor. For the neutral exciton, the fine structure splitting is often small, especially for and so even small magnetic fields eliminate the need to know this for the purposes of fitting (provided that $\mu B \gg E_{FSS}$. Knowledge of the g-factor is beneficial for understanding QD behaviour in a magnetic field, and determines how large a field is needed to be applied for the purposes of the field.

Figure 4.11 shows the energy separation for a Zeeman split transition in a magnetic field range of 0T up to 3T.

In order to determine the g-factor, the diamagnetic component is subtracted. Individual PL curves are fitted for the two transitions and the peak centre is extracted. A The gradient of a fitted straight line for the resulting plot shown in the figure is the exciton g-factor. This g-factor is (typical) for InGaAs QDs, and therefore it is likely that the fact that the QD is embedded within a nanophotonic device does not affect the QD's magnetic response. This principle is further investigated in chapter 5, where spin-pumping of a charged exciton is performed.

4.5 Summary

The chiral coupling of an integrated QD and the helicity of light leads to the deterministic routing of photons within a network. The designs discussed in chapter 3 show not only how (Purcell-enhanced) slow light can be coupled to fast light through a series of adapters, but also predict highly chiral areas with a strong electric field profile in tandem. The result of an emitter being placed within these chiral areas is the direct correlation between the overall spin of the excited state and the emission direction of the photon. This is to say that, for a neutral exciton, the two spin states $|{\downarrow}{\Uparrow}\rangle$ and $|{\Downarrow}{\uparrow}\rangle$ will emit a photon in different directions in the presence of a magnetic field (without a magnetic field, as discussed in section 1.4, the spin states couple to linear polarisations, which means that an emitter at a C-point couples to either direction symmetrically.) For the X^- state, the $|\uparrow\downarrow\Uparrow\rangle$ and $|\uparrow\downarrow\Uparrow\rangle$ can also couple to two emission directions in or out of a magnetic field (though a magnetic field is used to spectrally distinguish the two states). Fundamentally, both of these experiments mean that deterministic initialisation (such as through polarised excitation) of a particular state is possible with an efficiency equal to the contrast at the emitter's physical location.

Additionally, experimental results were presented demonstrating the basic efficacy of the modified glide plane geometry.

Chapter 5

Demonstration of Purcell Enhancement Tuning Inside Modified Glide Symmetric Structures

Chapter 3 introduced variety of designs which had the potential to show spectrally broadband, chiral, Purcell-enhanced emission - all have which been demonstrated individually yet rarely in combination. In the modified glide plane waveguide, a series of QDs (both chiral and symmetrically-coupled) have been shown to experience modest to large Purcell-enhancements based on their spectral proximity to a slow light region, which can be first theoretically predicted based upon fabrication design, and then retrospectively determined using experimentally-obtained transmission data. In this chapter, data is presented on a series of non-resonant and quasi-resonant (phonon sideband) lifetime measurements of QDs in both bulk and in glide plane waveguides.

5.1 Emitter Lifetime Measurements

The lifetime of an emitter, as discussed in chapter 2, represents a measure for the amount of time for which an emitter contains an active state which can either be acted upon or have information stored within, and is parametrised by the T_1 time. Knowledge of this quantity is incredibly useful for quantum information processing because the recombination/relaxation of the state within the QD is an upper limit for the amount of time a system would have to perform any computation. However, this parameter need not be maximised, and in fact, a minimisation of this lifetime provides a brighter source such that more photons are emitted per unit time. The benefit of a short emitter lifetime is not only that a larger number of information carriers for QIP is produced, but also that the photons are emitted before decoherence processes can take hold of the spin state within the dot. The processes for calculating emitter lifetimes are discussed in chapter 2 but are summarised here.

An incident, mode-locked pulsed laser (either tuned to be spectrally located above the band gap of GaAs or narrowly filtered and tuned to be near the phonon sideband) impinges on both the sample and a heralding photodetector, with the photodetector signal being sent to a photon counting card. The laser generates a state within a QD, which recombines after a certain amount of time (in accordance with the lifetime). The emitted light is sent to either an avalanche photodiode (APD) or a superconducting nanowire single photon detector (SNSPD) which then emits another electrical pulse whose time stamp is corroborated with the heralding photodetector's pulse at the counting card. A time difference can be calculated and multiple measurements/cycles build up a statistical picture of the lifetime curve.
Typical lifetimes for InGaAs QDs within a bulk system (i.e. not within a photonic device) are usally averaged at approximately 1ns in literature [124], with few exceptions. By increasing the speed of the recombination process, the indistinguishability (governed by $T_2/(2T_1)$) can be improved. The radiative emission rate ($1/T_1$) is modified by the Purcell effect [118]. In order to determine the effects of a cavity on a QD candidate, a statistical picture of the general lifetimes on the sample itself must be

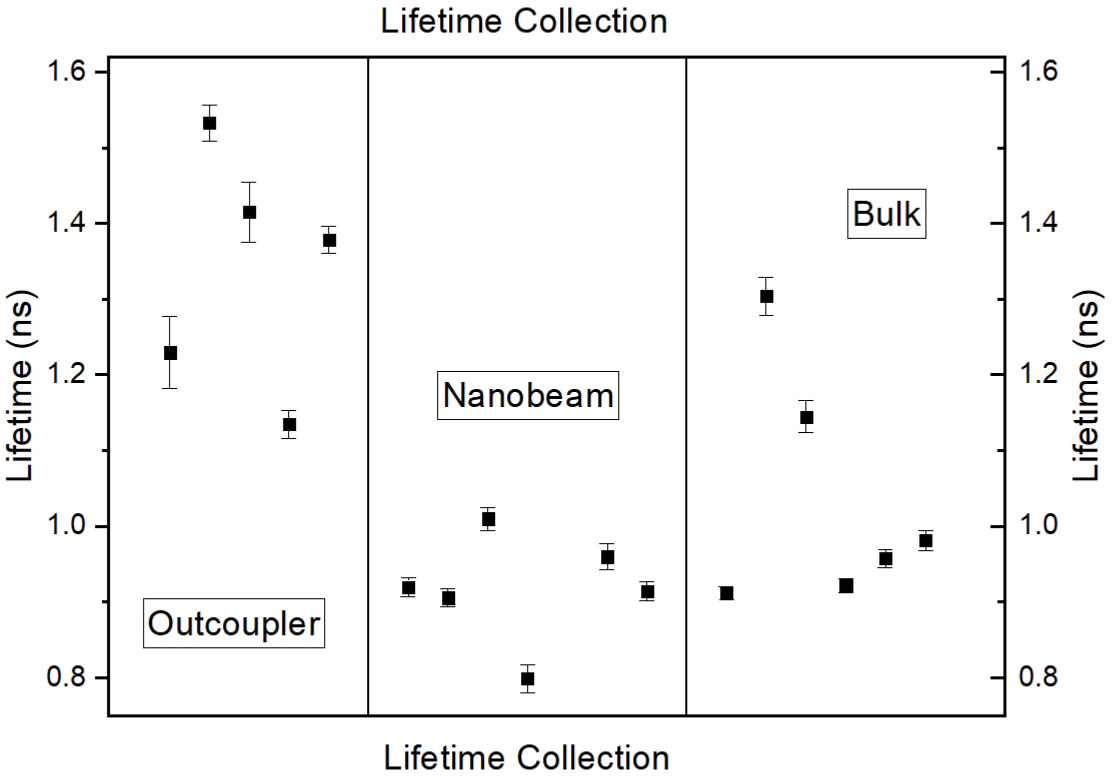

Figure 5.1: **Lifetime measurements for bulk, outcoupler and nanobeam waveguide QDs** | Each data point is either from a high power PL ensemble, or low power single QD PL. The difference between bulk data and nanobeam data is minimal, demonstrating a very small average lifetime reduction of <0.1ns

measured. This is the closest alternative to pre-registering the QD and measuring the lifetime both before and after device fabrication in the dot's vicinity. Quantum dot "bulk" lifetimes were measured for QDs in nanobeam waveguides, grating outcouplers and in glide-symmetric structures (specifically in the final GPW design and the GPN).

Figure 5.1 shows a segmented series of lifetime measurements on QDs in bulk, nanobeam waveguides and on outcouplers. Expected for the case of zero enhancing effects, the average QD lifetime in bulk is 1.04ns. Such lifetimes are well within the detector's capabilities (with a temporal resolution of 400ps), and most lifetime measurements were made from randomly selected (but bright) QDs, at a variety of voltages. An enhancement in the spontaneous emission rate is seen in the case of QDs within nanobeam waveguides with an average lifetime of 0.918ns, providing an enhancement of F_p=1.1. Notably, the enhancement is small, as the Purcell effect is caused purely by the reduction of the mode volume, as described in equation 1.3, and not by any slow-light effects. The lifetime of emitters in outcouplers were found to be τ_{OC}=1.39ns). This lifetime increase is of an unknown origin, as one would expect a reduction in the mode volume due to the air gaps from the etch. Lifetimes from figure 5.1 are an assortment of ensemble measurements (i.e. light is collected from multiple QDs emitting simultaneously) or spectrally-filtered single QD lines. Importantly, the number of emitting QDs makes little difference to the average, and only to the size of the errors.

The full population and recombination/emission process of QDs is multi-faceted, and across a long lifetime range can rely on carrier tunnelling, environmental noise, phonon population (to bring the carriers down from the semiconductor bands to the QD resonance if the charges are created non-resonantly), and ultimately a lifetime-enhancing environment the likes of which can be provided by a PhC cavity or waveguide. Up to the transform-limit, few parameters can be tuned in order to have an effect on the lifetime of a QD, with some having essentially zero effect such as a Faraday magnetic field. Even electric fields may only affect the lifetime implicitly through the elimination of a noisy environment or through minimising the charge tunnelling rates out of the quantum dot.

Presented in figure 5.2 is the transmission spectrum (a), the reconstructed band structure (b) and a series of lifetime measurements (d) for QDs located in the glide plane waveguide for the same design at the spectral locations marked in (c). The QDs selected for these measurements are not located near the slow-light region of the GPW dispersion, and their spectral positions are marked. Some QDs see a small shift in the transition energy because of the applied fields, but none show an appreciable change in the lifetime in the non-resonant scheme. In this case, only the phonon population could be responsible for a change in lifetime (as the slow light region for these QDs is predicted to be at least 30nm away from these transitions).

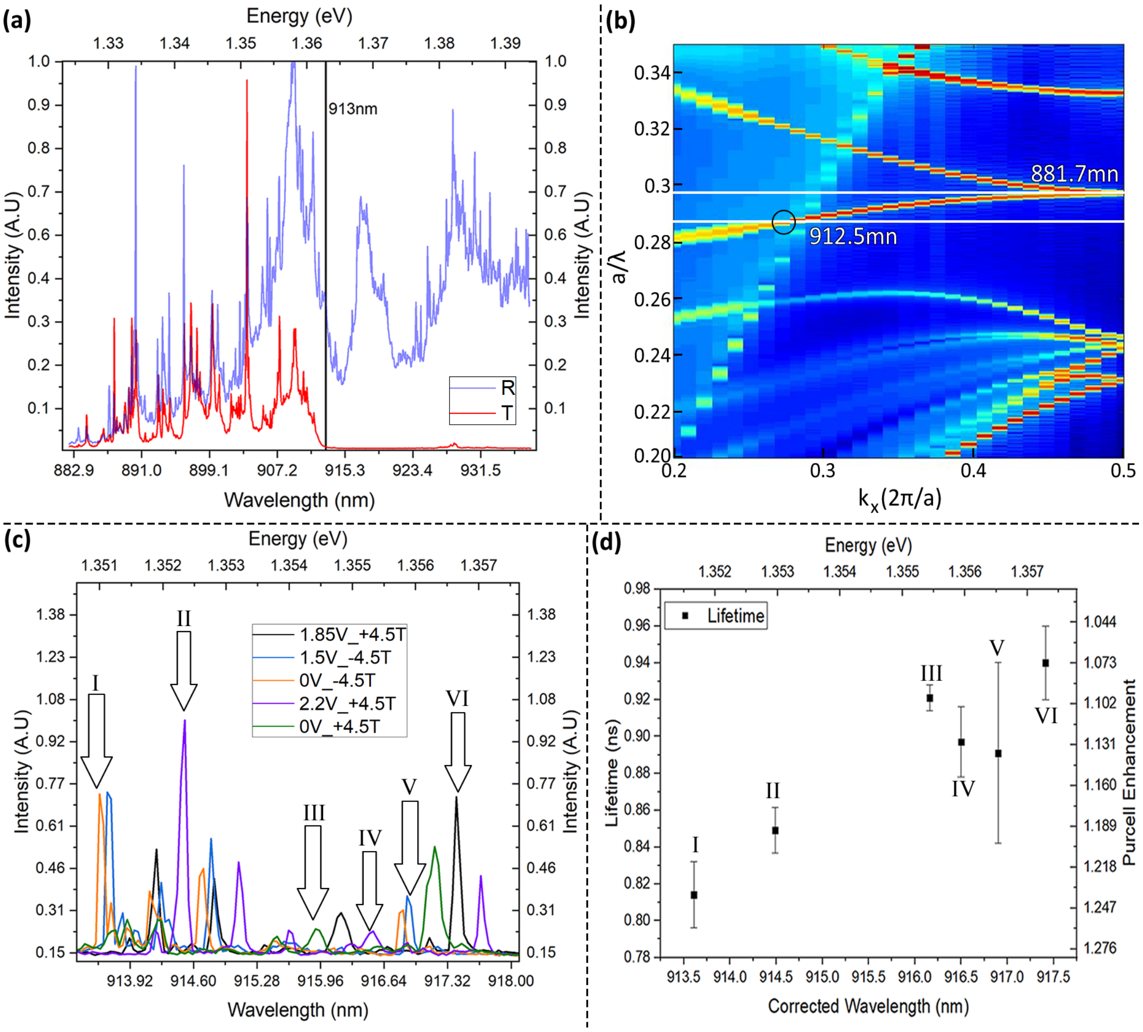

Figure 5.2: **Experimental (a) and theoretical (b) dispersion diagrams of a device with emitters of un-enhanced lifetimes (c) away from the slow light region. Spectral locations shown in (d).** | R and T in part **(a)** stands for the reflection and transmission of light from one outcoupler to another. Different applied voltages and magnetic fields (from 0V to 2.2V and -4.5T to +4.5T respectively) show the lack of explicit changes to the emitter lifetimes caused solely by the fields themselves. The legend in (c) shows the applied voltage and magnetic field for each of the series of lines. Three distinct QDs are featured. Pairs labelled I & II, III & IV and V & VI are iterations of the same three QDs under different voltages or magnetic fields. The QDs between (c) and (d) are labelled. They are located approximately in the black circled area of the dispersion diagram of (b). While the QDs are very close to the light line, their brightnesses are relatively dim when compared to other emitters in the crystal, and long exposures were used to obtain the lifetime plots shown in (d). Figures 5.12 and 5.13 show specific voltages and magnetic fields present for the record-breaking lifetime QD, for different emitters on the same sample.

Section 5.3.2 presents further experimental results of the effects of variable external fields on the lifetime of emitters not located in a Purcell-enhancing environment, in order to properly express how the effects of external fields within the relevant field strength ranges have little effect on the lifetime of the emitter.

5.2 The Glide Plane Nanobeam

Alongside the details of the glide plane waveguide, Chapter 3 discussed the principles of the glide plane nanobeam (GPN) as a possible stand-alone waveguide, with a modest Purcell profile and a competitive chiral contrast area, with a predicted 28% of the device showing chirality of at least 90%, with a slightly stronger Purcell factor (due to the mode volume) than the standard nanobeam waveguide. The benefit of this device over the GPW is the coupling to the regular nanobeam waveguide, and this is known as part of a parameter known as the "insertion" factor of the device [125]. In chapter 3, the band diagram of the GPN is presented with a similarity closer to that of a W1 defect PhC: featuring a band gap. This feature is unlike the GPW design, which instead shows a broad transmission window capped only by the light line at both the long and short wavelength ends of the dispersion. Such a large band gap can be both useful and restrictive when matched with the broadband possibilities of the GPW.

However, the GPN sees a few disadvantages that manifest even in the full GPW design discussed above. Three transmission spectra are shown in figure 5.3, in order to depict the differences that changes to certain parameters can make to the onset and size of the opacity window due to the GPN dispersion's band gap. The design hole sizes differ only by a few % (ranging from radii of 0.28a to 0.32a, for a a variety of crystal periods between 85nm and 97nm) in order to probe a wider parameter space, and to also ensure that if a specific device does not meet the design criteria, that another might incidentally fulfil it instead. The spectral position and size of this band gap is influenced by a complex combination of the size of the holes, and with the period (relating to the hole radius by $a = r/0.35$).

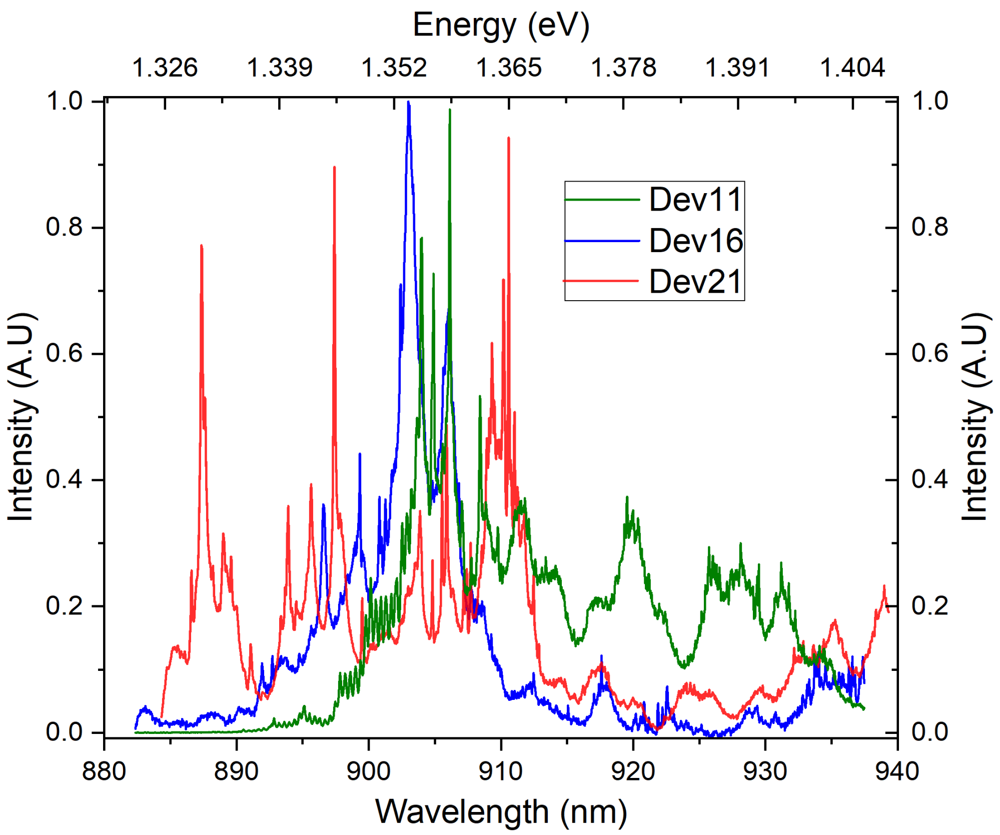

Figure 5.3: **Glide Plane Nanobeam Transmission spectra for three devices with periods: $\mathbf{a_{11} = 258nm, a_{16} = 262nm}$ and $\mathbf{a_{21} = 258nm}$** | μPL transmission of various devices. Each device demonstrates a different onset for the beginning/end of the opacity window or pseudo-band edge. Moreover, the transparency window for devices 16 and 21 are visibly different in magnitude, with the red curve extending into longer wavelengths, owing to both the different hole sizes $r_{21} = 0.3a_{21} = 77nm; r_{11} = 0.28a_{11} = 72nm$ and $r_{16} = 0.28a_{16} = 73nm$ and periods.

Each device shown in figure 5.3 has different parameters, which can lead to one transparency window being over 30nm away from that of another device. The GPN device 11's transmission, as labelled (coloured green) in figure 5.3, shows the upper band portion of the dispersion, as the frequency cut-off is to the left side of the spectrum, starting at around 898nm, extending to the shorter wavelength direction. By contrast, the dispersions of devices 16 and 21 have the lower band present in the majority of the transmission window, with the beginning of the transparency window being at approximately 915nm and 909nm respectively. This principle of tuning the transparency window can be used for generating devices that can act as spectral filters for broadband operation. A dispersion diagram for the infinite GPN (with the parameters of the device discussed in section 5.3), shows a close-up of the

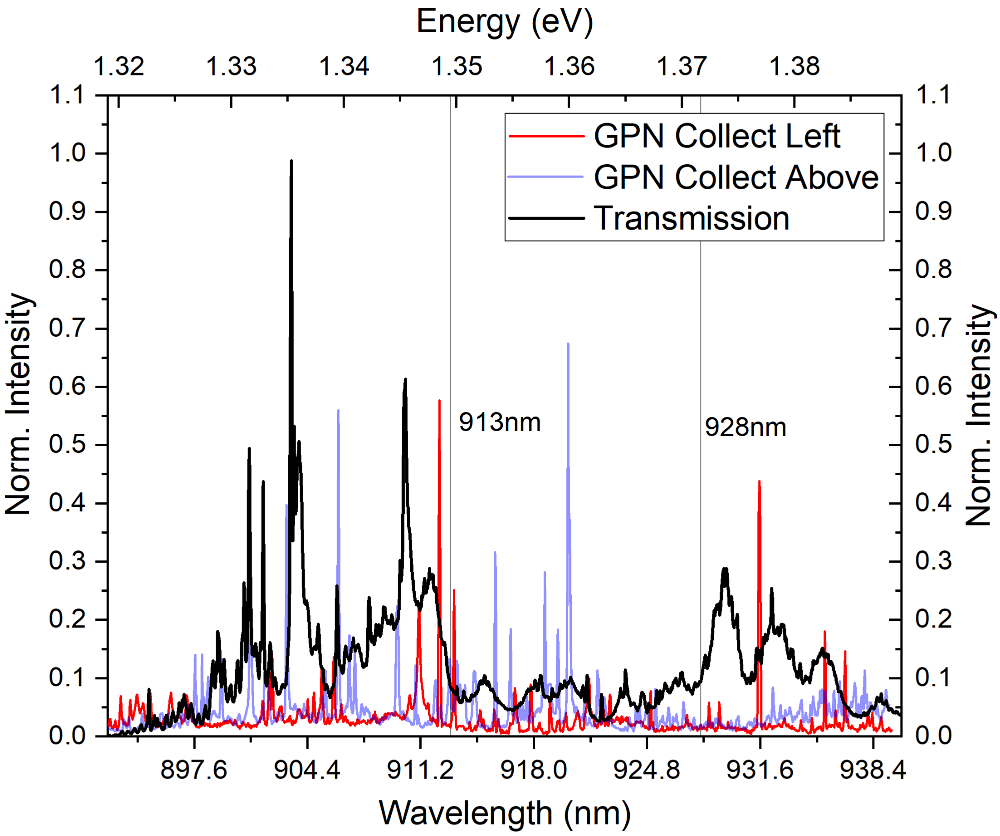

Figure 5.4: **Glide plane nanobeam directional emission** | Colour-coded μPL for QDs collected: directly above the glide plane nanobeam (light blue) and above a grating outcoupler to measure the light coupled into the GPN (red). Presented also is the transmission spectrum (black), where the band gap (marked at 913nm and 928nm with grey lines) marks much lower intensities of coupled PL, as seen by the dimmer red lines relative to the blue lines across the full spectral window. The red and black curves show a similar dip in intensity within the band gap, whilst, as expected, the blue PL shows emission, as this light does not transmit through the crystal.

band gap alongside the turning points for the upper and lower bands of the first order mode.

The fundamental application for the glide plane nanobeam was to act as a mode adapter for the glide plane waveguide, with a simulated TE mode designed to match the spatial mode of light confined to the glide plane waveguide, as the regular GPW does not couple into the standard nanobeam waveguide effectively, as discussed in ref [126]. While ref [127] shows an adiabatic (incremental) reduction of the hole size of the indentations in the GPN, designs here do not invoke this method. Some full GPW transmission profiles are shown in the next section.

Despite the theoretical limitations of the transmission profile of the GPN, devices still showed directional coupling. Figure 5.4 shows a μPL spectrum demonstrating QDs within glide plane nanobeam regions. The overall β-factor for this device is not very high, as the intensity difference between the light collected directly above the excitation location and the light collected above the outcoupler is quite large. The graph shows that between the two marked boundaries of the band gap, detected μPL at the device outcouplers does not show any QDs within this band gap. However, collecting directly above the GPN, plenty of QDs emit within the very same spectral region.

5.2.1 Glide Plane Waveguides with a Glide Plane Nanobeam taper

In chapter 3, dispersion diagrams were provided for a fabricated GPW which show a reasonably broad slow light region. Band structure calculations allow for estimations of slow down factors starting at factors of around 2, over a 10nm window surrounding the crossing point of the two allowed GPW modes. A variety of QDs, which are spectrally distributed randomly within the crystal, across a series of devices, have had their lifetimes measured. These lifetimes are corroborated by their location relative to the slow light region, which was determined by reverse-engineering the band structures based on experimentally-obtained transmission spectra. Many of these QDs are chiral, and the ones that are have their chiralities listed alongside the lifetimes & chiralities. The QD's photoluminescence spectra are provided in the appendix, which also show the slow light region of the device along with the reported lifetimes in table 5.8.

While each GPN device contains ∼55 periods, the four to six indentations present in design four's adapter are enough to provide some spectral filtering which manifests as a small reduction in the transmission intensity. This can cause a reduction in apparent intensity of a QD located within the slow-light (Purcell enhanced) region of the GPW by the pseudo-gap (it is not a full band gap as the number of periods cannot be approximated by an infinite crystal) of the GPN adapter spectrally over-

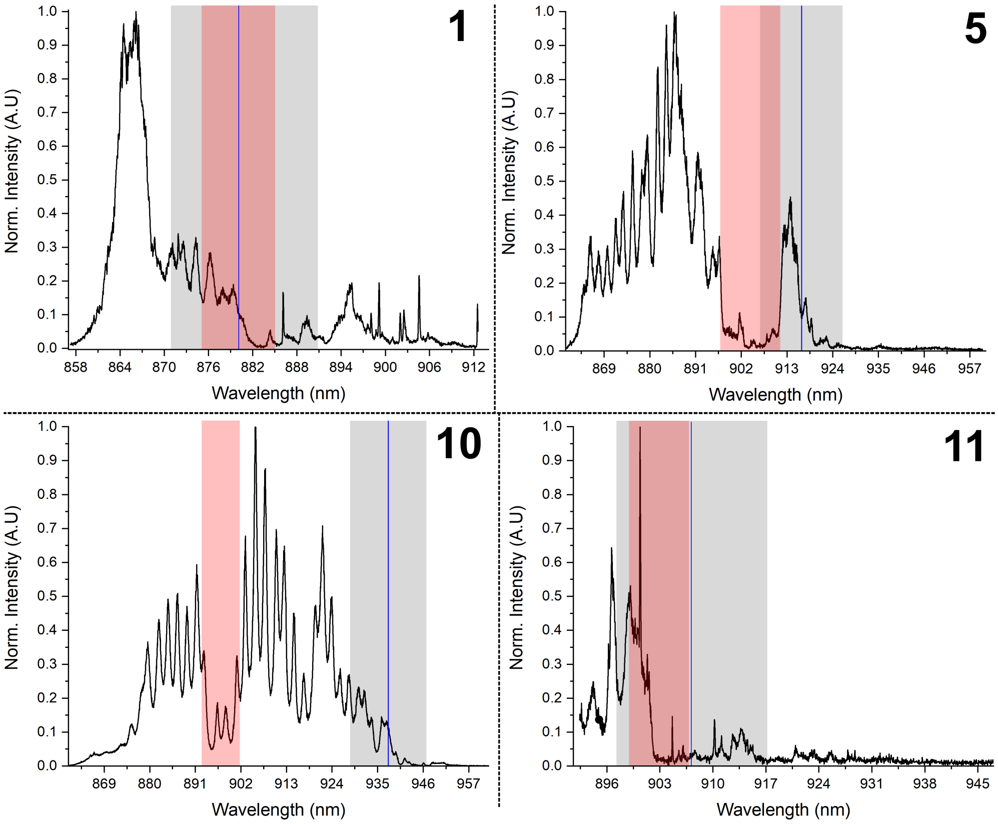

Figure 5.5: **Transmission for four devices of the full optimised GPW, with the glide plane centre and GPN adapter.** | Highlighted in grey are the slow light regions for each device, with the blue line indicating the centre of it. Red indicates the predicted band gaps for the glide plane nanobeam adapater, assuming an infinite number of 1D lattice holes. The differently highlighted regions show that the GPW slow light region need not be contested by the band gap of the GPN. Marked are designs 1 (a=250mn), 5 (a=254nm), 10 (a=258nm) and 11 (a=258nm).

lapping with the QD. As a result, one may expect a relatively dim QD signal at the outcoupler, but a Purcell-enhanced (shortened) lifetime compared to bulk.

A few examples of the phenomenon of overlapping GPN band gaps and GPW slow light regions are shown in some GPW/GPN transmission spectra with an identified slow light region based on the frequency cut-offs in figure 5.5. In this figure, the slow light regions and light line cut-offs are marked in a similar fashion to the way they are highlighted in the dispersion diagram shown in figure 5.2. This time, a 10nm window is highlighted on the transmission spectra across the slow light regions. Within this window, a QD would experience a noticeable Purcell enhancement, but may also have its collected intensity reduced by some factor η. It is worth noting that the spectral overlap between the band gap and the transmission profile of

GPW provides a reduction of magnitude η^2, and so the QD emission is not doubly quenched in photoluminescence as the transmission spectra would show.

The purpose of uncovering short lifetime emitters through Purcell enhancement is useful for fast, single-photon emission, maintaining their coherence and relation to a quantum dot spin in accordance to equation 1.1 in the thesis introduction, where ideally, $T_2=2T_1$. By quenching the number of photons which make it through the GPN adapter, an upper limit is present to the number of coherently extracted photons from a QD embedded within a photonic crystal. However, it is not a requirement for this mismatched alignment between the GPN band gap and the GPW slow-light region to exist, and therefore careful selection of a device could achieve the result of efficient photon extraction.

5.3 Tuning of Emitter Lifetime Through Application of External Fields

The modified GPW within a p-i-n heterostructure culminates a system of a tuneable chiral emitters embedded within a high-β (low-loss) photonic crystal waveguide environment which can efficiently couple to a standard nanobeam waveguide. While other high performance cavities can show enhanced QD emission such as H1 cavities which have demonstrated Purcell factors of over 40 [128], only modest Purcell enhancements (<8) have been found for a waveguide-embedded emitter [129]. With the modified glide plane waveguide, a Purcell enhancement of a QD within a quasi-resonant setting of the order of 15 has been found, with the data presented in this section. On top of this, this Purcell enhancement was maximised via the application of external fields, without which the natural enhancement (due to the randomised QD energy and position) would have been drastically reduced.

Random QD energy distributions in SK growth results in the inability to tailor the spectral properties of the emitters to match those of the crystal. However, with the application of external electric and magnetic fields, the restriction of a precise

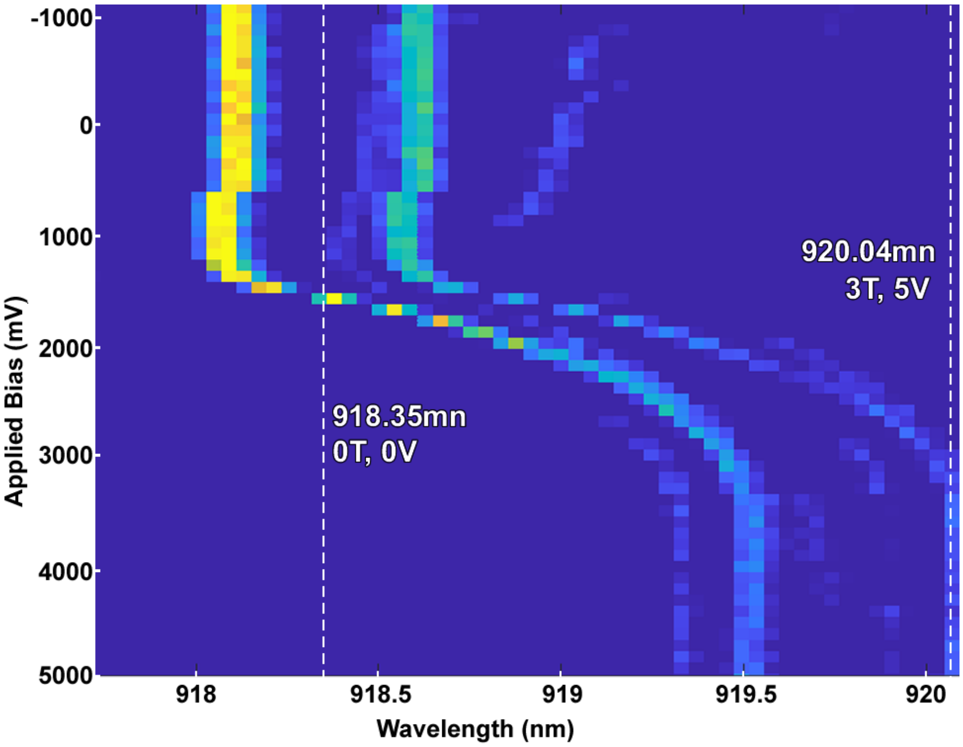

Figure 5.6: **PL tuning map for a magnetically split QD line located in device 10, whose dispersion appears in figure 5.7** | Marked is the central wavelength before the magnetic field of 3T was applied, and the final wavelength after the same QD state is tuned to 5V. This shift of ~1.7nm is typical, but does not take place close to the slow light region of this device.

natural overlap of a narrow emitter and the spectrally-sensitive slow light region can be slightly relaxed, as tuning the energy can bring these two more strongly into resonance. QD energies can be manipulated in this sample to have their emission tuned by up to 3nm with a complimentary effect of Stark and Zeeman tuning, which is a significant fraction of the slow light region. However, this maximal shift is asymmetric and is limited in both energy directions by the QD's response to the fields. For the Stark effect, only a red shift of the QD energy is possible due to the reverse bias scheme used in this work, and the total electric field vector acting on the QD. The magnetic field is more forgiving, as a split transition (corresponding to one spin state only) can technically access a blue-shifted range of energies by flipping the direction of the magnetic field. However, according to equation 2.2, the B^2 (the diamagnetic shift) component always acts to blue shift the excited transition, so a very large magnetic field would only act to counteract the Zeeman

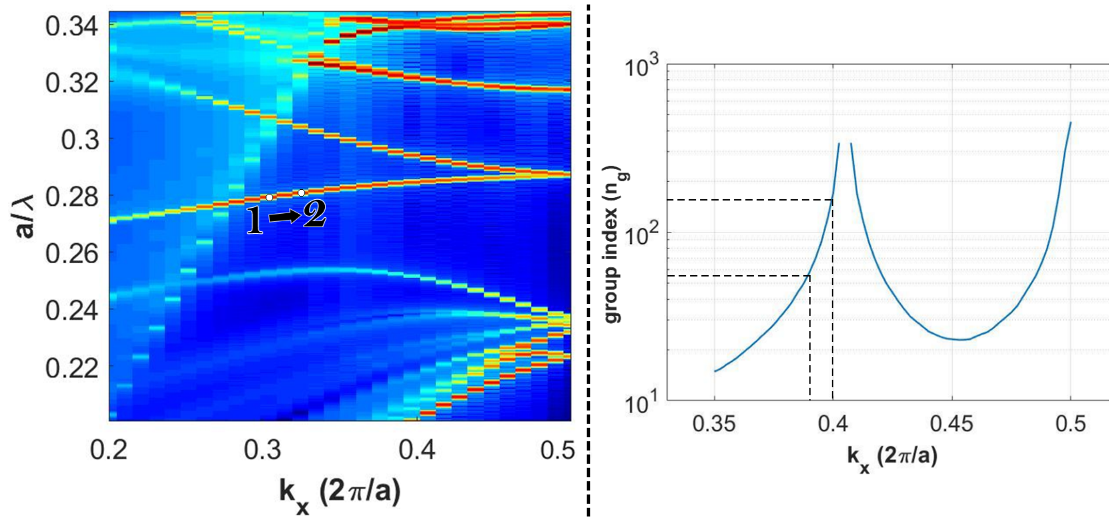

Figure 5.7: **Dispersion for the glide plane waveguide region of the device containing the** $F_p = 15.1$ **QD from table 5.8** | Left: Dispersion for the QD in figure 5.6. Both the dispersion and the group index (convertible to the lifetime enhancement) are plotted against the wavevector, k. The labelled points, $1 \rightarrow 2$ show the energy shift from the QD in figure 5.6. Right: Simulated dispersion, showing how the same energy shift magnitude could change the group index drastically.

shift experienced by one of the components. These limitations can be important, because they result in a favourability of an emitter being on one side of the crossing point to the other, as the energy is more easily shifted towards the slow light than away from it. Moreover, the Zeeman splitting is constant regardless of the applied bias, and so the lower energy transition Zeeman-split line has its shift compounded by the red shift from the bias changes.

The electric tuning of a magnetically-split line is shown in figure 5.6 (p.133), which shows typical tuning of approximately 1.5nm with the work of both fields. Approximately 0.1nm of the tuning comes from the Zeeman splitting, and the rest is from the Stark shift. Observing a reconstructed band structure for this device, the marked QD's tuning moves from the two positions in the diagram, labelled numerically in figure 5.7 (p.134). The change in group index is small at the spectral location, providing alterations to the group velocity of less than an order of magnitude. Closer to the crossing point of the modes, a change in $k(a)$ of 0.2 from 3.8 to 4.0 can result in exponentially large Purcell factors, as is predicted by the (right side) GPW dispersion of figure 5.7.

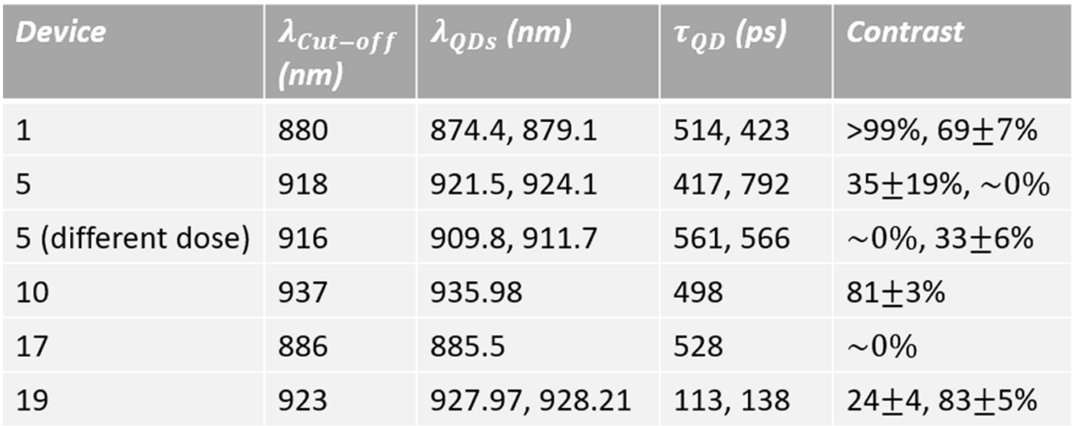

Device	$\lambda_{Cut-off}$ (nm)	λ_{QDs} (nm)	τ_{QD} (ps)	Contrast
1	880	874.4, 879.1	514, 423	>99%, 69±7%
5	918	921.5, 924.1	417, 792	35±19%, ~0%
5 (different dose)	916	909.8, 911.7	561, 566	~0%, 33±6%
10	937	935.98	498	81±3%
17	886	885.5	528	~0%
19	923	927.97, 928.21	113, 138	24±4, 83±5%

Figure 5.8: **Table containing a series of slow light QDs with their chiralities (if applicable) marked.** | Devices labelled are in accordance with those seen in the SEM of figure 2.4, alongside the device's re-estimated cut-off regions. The wavelengths, lifetimes and chiralities of the selected QDs are presented in the same order. A full series of PL spectra, alongside the device's cut-off points are presented in the appendix. QDs with very little discernible directional contrast, or QDs with only one component appearing in the magnetic field spectra, are marked as ~0% and $> 99\%$ respectively.

QDs have been found which show large reductions to their emission lifetimes relative to the nanobeam or bulk lifetimes. These lifetimes are presented in table 5.8, [1]. Table 5.8 (above) summarises this series of QDs, marking their emission wavelength, and any chiral contrasts alongside their lifetimes. A single dispersion diagram for the fully optimised GPW which contains a QD faster than those in table 5.8 is provided in figure 5.9. The design (device 11) is optimised to have the crossing point of the two modes at 907nm (corresponding to a hole period of 258nm, and a hole size of $r = 0.35a \sim 90nm$). This device, discussed more in the following subsection, contained a QD with a very fast lifetime of 70ps, allowing for emission well into the GHz range given a minimum 7% single photon extraction efficiency. However, improvements to the general experimental designs (such as more efficient outcoupler gratings) would need to be made in order to observe the Billions (per second) of emitted photons.

---

[1] Their spectral locations within their device's dispersion diagram are shown in the Appendix.

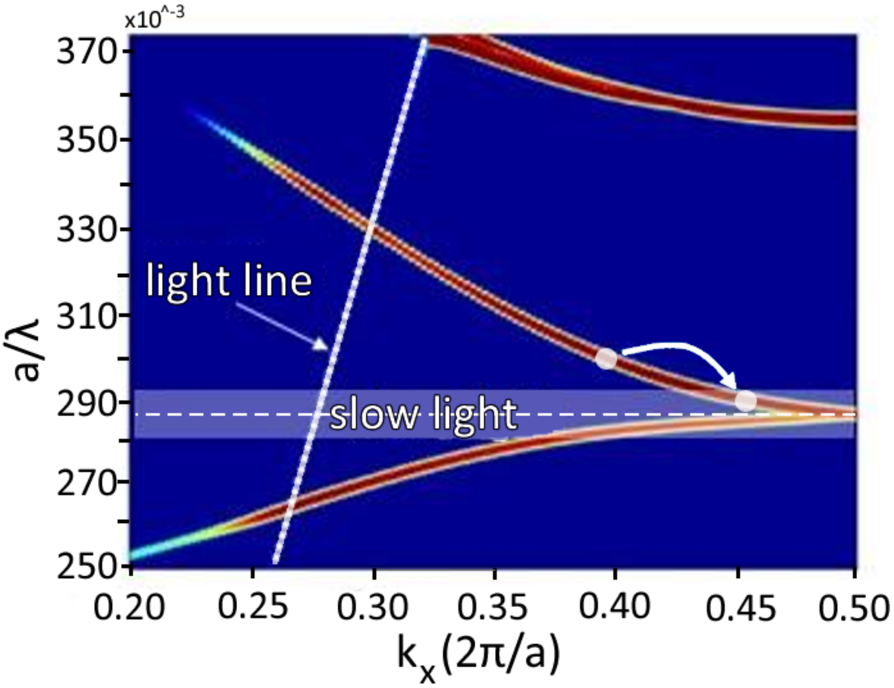

Figure 5.9: **Dispersion for the glide plane waveguide region of the device containing the $F_p = 15.1$ featured in figure 5.11** | As the wavelength of the emitter is shifted within the glide plane, the detected lifetime gets shorter over the range demonstrated in figure 5.10. Labelled here are the light line cut-offs, with the upper band being well into the wetting layer emission region (~880nm) and the lower cut-off near 980nm. Simulation by H. Siampour.

5.3.1 A Waveguide-Based, Record-Breaking Short Lifetime

In figure 5.11 (p.139), a QD is presented that demonstrates the shortest measured lifetime contained within a passive geometry. This subsection discusses how the Stark shift of the QD state alters the lifetime of the emitter by changing its spectral position within the slow light region.

First, a (filtered) PL spectral map is shown to locate the position of the QD, and this is shown in figure 5.10. Interesting locations within the PL map are marked by white circles, and are labelled with their exact energies and the relevant voltage. This is corroborated by two (white-circle) marked locations on the dispersion diagram with the crossing point mentioned above in figure 5.10. At the bottom of the figure are two lifetime curves generated from performing phonon-assisted absorption, known as phonon-sideband excitation. This process was used because above-band excitation limits the potential lifetime that can be observed for this emitter to 135ps. With

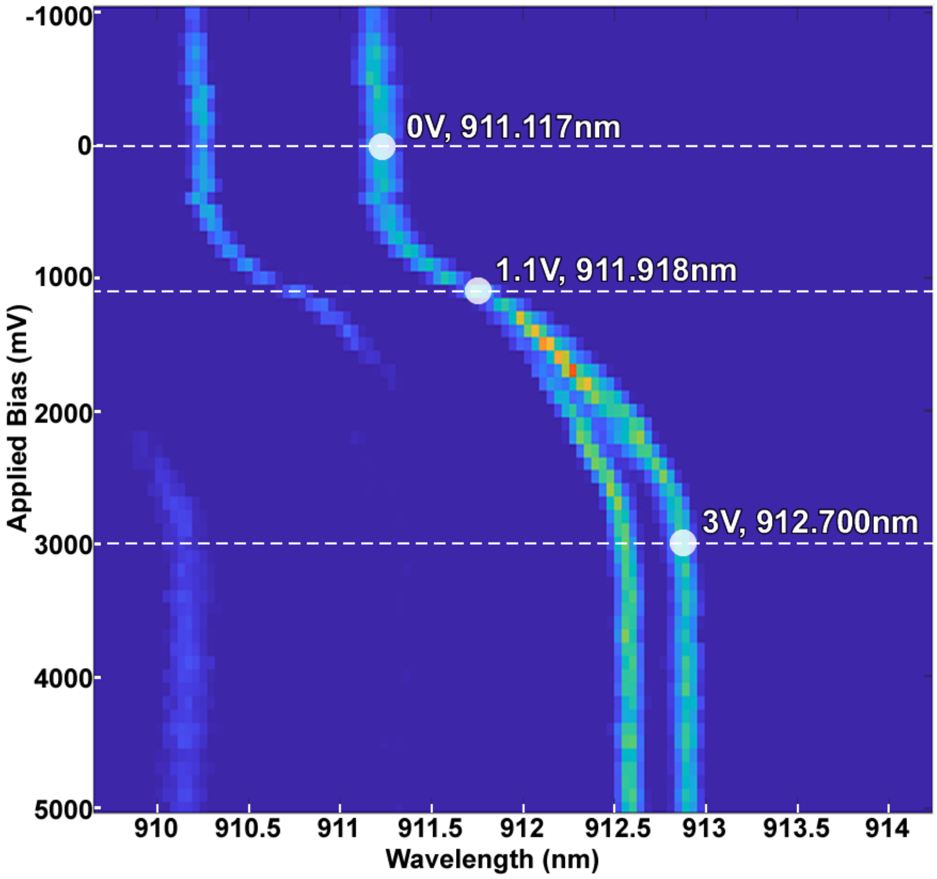

Figure 5.10: **μPL map for the QD featured in figure 5.11, device 11** | The right QD line experiences an energy shift of around 1.5nm due to the externally applied bias, under a CW excitation scheme. Further tuning is from the application of different powers from the pulse laser. The dotted lines show the three main voltages for which the lifetime is recorded. The specific experimental circumstances are outlined in the text.

phonon-sideband excitation, an upper limit to the emission lifetime was measured to be a world-leading time of 69ps (for a photonic crystal waveguide-coupled InGaAs QD). The current (world) record for a QD lifetime is the QD presented in ref [128], of 22.7ps. However, this lifetime was measured in a resonant scheme, using a unique pulsing sequence not performed here.

Figure 5.11 shows a series of lifetimes for the F_p=∼15-limited QD, plotting the magnitude of the Purcell enhancement with respect to the emission wavelength. The rightmost data point is the line QD at 3V marked in figure 5.10 (the left line is not shown in this lifetime progression plot, but for reference, the lifetime of this QD at 3V was (630± 20)ps). The central three data points between 911.6nm and 911.9nm of figure 5.11 show the progression of tuning the voltage from 1.1V to 0.8V

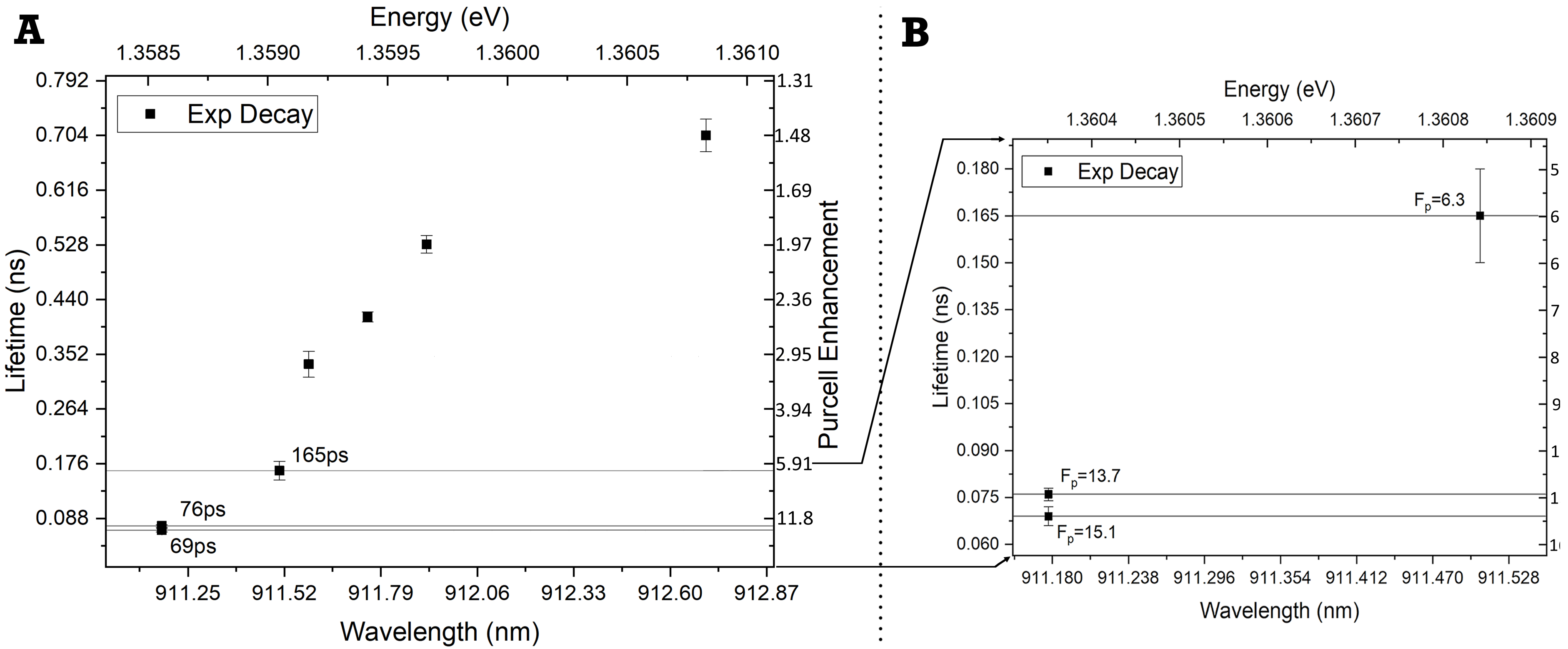

Figure 5.11: **Lifetime exponential decay progression for the QD under above-band and phonon sideband excitation** | As the wavelength of the emitter is shifted within the glide plane, the perceived lifetime gets shorter over the range demonstrated in 5.10. The different conditions of study for each data point are explained in the text. Shown in the inset is a zoomed-in version of the three shortest lifetimes, with the Purcell enhancements labelled rather than the lifetimes as is in the main figure.

to 0V, all performed in the above-band excitation scheme with an 810nm (central wavelength) pulsed laser. The bottom three data points in the series are generated under quasi-resonant excitation. The datum of 165ps is achieved at zero applied magnetic field under the quasi-resonant excitation scheme. The final two shortest lifetime data points (79ps and 69ps) are achieved at a magnetic field strength of -4.5T, with the bottom of the two obtained by applying a different excitation power. With the quasi-resonant excitation, Purcell factors well over 6 are explorable.

5.3.2 Intrinsic Effect of Magnetic and Electric Fields on Lifetime

In order to further evidence the claim that spectral location to the slow light is responsible for the Purcell enhancement changes of the QD discussed above, a series of lifetimes are presented for QDs in bulk and inside nanophotonic devices where the magnetic and electric field are not expected to spectrally shift an emitter towards a slow light region. It is estimated that a modification to the built-in potential, or an external magnetic field, should have some effect on the intrinsic emitter lifetime ([130]) (associated with T_1), especially where the electric field lines are parallel to the growth direction of the QD. The electron hole wavefunction overlap changes in response to the presence of the electric field, may change the recombination probabilities, alongside the QD emission energy. Decoherence mechanisms such as electron co-tunnelling, spin-flip and Auger (in charged excitons) processes may play parts in the recombination behaviour of excitons inside the QD [131], but are more relevant to the single spin coherence and initialisation, rather than exciton recombination (see chapter 6.6).

The homogeneous linewidth of a QD is determined by pure dephasing, providing the unmodified emitter lifetime. In non-resonant excitation schemes, even at low temperatures (to wash out the majority of phonon effects, though phonon scattering is still possible), the observed linewidth of the transition is extensively washed out by inhomogeneous broadening. The largest contribution of such broadening is spectral

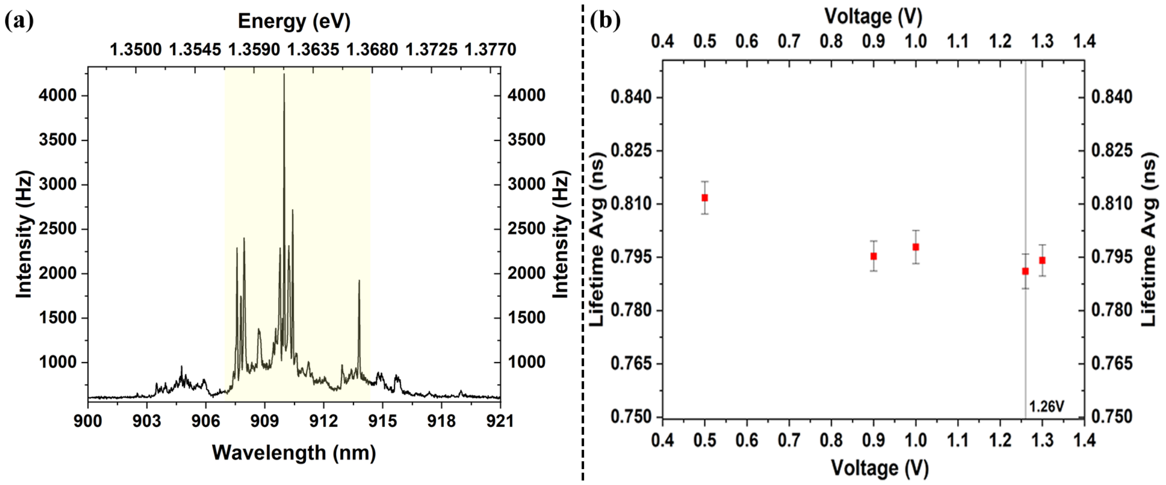

Figure 5.12: **Example ensemble PL (a) and individual QD lifetimes at applied external voltages (b)** | Highlighted in (a) is a typical PL spectrum used to obtain lifetime measurements for those produced in (b). A spectral filter is used to only obtain light present in the lines behind the yellow filter. Across the range 0.5V to 1.3V, no change in ensemble bulk lifetimes are observed, as expected for an electromagnetically unmodified environment.

wandering, where a small fluctuating charge environment acts upon the confined e-h pair. The intensity of such fluctuations are small when compared to the Stark shift that can be provided by the external electric field, but are enough to broaden a transition of 10's of neV to the μeV regime. However, such effects are minimal on the lifetime of the emitter, as the wandering occurs on timescales thousands of times greater than the radiative lifetime. Also, such processes occur on the longest of time scales, much faster than usual recombination times, even in the unmodified, bulk ns regime.

Figures 5.12 and 5.13 show a series of lifetime measurements for high-power bulk (ensemble) PL and lifetime measurements for individual bright dots located within bulk and in a nanobeam waveguide. The measurements feature lifetimes of emitters at different applied voltages in order to demonstrate that the application of an external bias is not necessarily explicitly causative to a change in lifetime of the emitter. The nanobeam measurements show five lifetimes which are consistently around 0.8ns (averaged at 0.79806ns$^{+0.0137}_{-0.0697}$), providing a weak Purcell enhancement of F_p=1.25. The bulk ensemble lifetime measurements are accompanied by the spectra related to those lifetimes. The spectra did not change for the QDs within

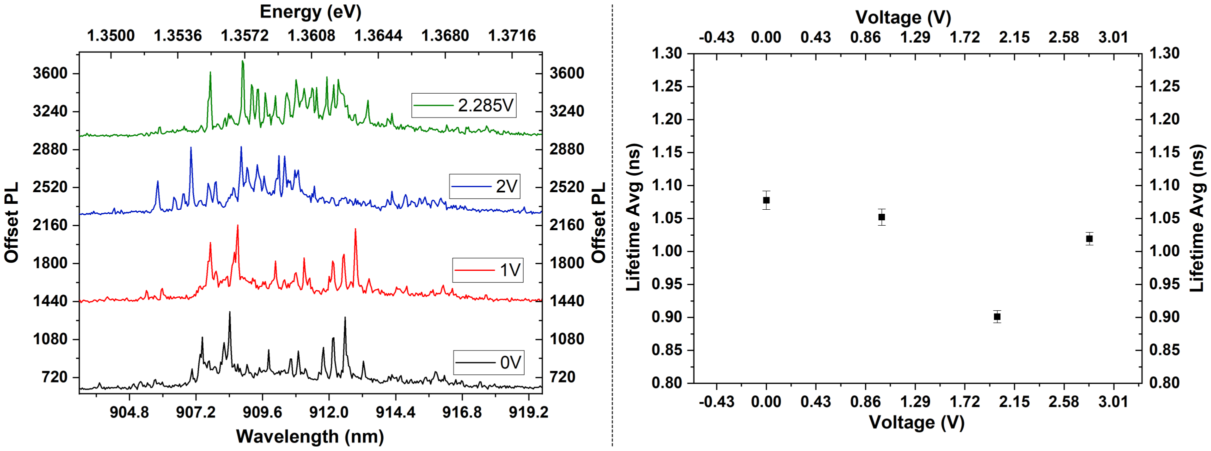

Figure 5.13: **Example ensemble PL (left) and individual QD lifetimes at applied external voltages (right) for QDs in a suspended nanobeam** | Shown on the left are the ensemble spectra associated with the lifetime data points of the right. The individual μPL are shown (unlike in the case of figure 5.12) as they differ at the voltages shown. Only the QDs at 2V seem to differ in lifetime, but this could be attributed to additional short-lifetime QDs that appear in the spectrum.

the nanobeam within the tested ranges, and therefore only one spectrum is shown in figure 5.12.

5.4 Conclusion

The glide-symmetric photonic crystal waveguide poses many advantages for the implementation as a key component for on-chip quantum optical processing. In a fully-optimised device, the GPW has been shown to house emitters with Purcell enhancements of at least 14, a record in the world of waveguide-embedded QDs. Moreover, with careful implementation of a mode-matched glide plane nanobeam and with the application of a magnetic field, chiral, single-photon extraction can take place. Such a device would allow for many of the benefits listed in [94] of chiral, Purcell enhanced interfaces, and would also make a good candidate for a platform carrying out the physics presented in chapter 6. It has been shown that, for emitters in both other passive devices and in bulk (unetched) regions, the lifetme does not change measurably for QDs within a similar spectral range when the same electric and magnetic field conditions were applied.

Chapter 6

Charged QDs and Spin Pumping of QDs Inside Nanophotonic Structures

Previous chapters in this thesis have discussed the control of the flow of light within a nanophotonic circuit through the the use of chirally optimised structures based on glide-plane waveguides. Such waveguide designs were shown to drastically enhance the spontaneous emission rate of quantum dots embedded within them, with the possibility of magnetic and electric fields providing energy tuning, moving them closer to and further away from the glide-plane photonic crystal slow light region. This chapter touches on the use of a quantum dot embedded within an electrically-controlled quantum dot as a static qubit through resonant interactions.

6.1 Electrical Control of Charge-Tuneable Heterostructures

One part of the DiVincenzo criteria concerns the initialisation of QD states. Outside of the photonic device, QD states and single spins can be generated/initialised and manipulated through many means such as optical pulses, or electron spin resonance (though, this was achieved only once for a trapped electron in a heterostructure InGaAs QD [132]). The deterministic population of (charged) quantum dots is achieved through the application of external electric fields. Two methods of applying an electric field across an embedded QD involve sandwiching the QD within a heterostructure. For QDs that do not require nanophotonic structures, electrical control can be performed with a Schottky diode. Schottky heterostructures consist of a neutral (undoped or intrinsic) semiconductor layer sandwiched between a bottom n- contact and a top metallic contact (acting as a very heavily doped n- layer). With an appropriately doped semiconductor n- layer, a permanent, smooth, uniform electric field is applied across the embedded QDs, similarly to the p-i-n wafer described in chapter 2. The Schottky diode is usually implemented in fast electronic systems such as rectifiers or surge protectors. The lack of minority carriers slowly diffusing through the p- and n- layers (as in a p-i-n) allows for fast switching for forward or reverse biasing or even nullifying the junction completely (to produce $\mathbf{E}$=0) as the electrons present in the sample are majority carriers. Such fast electrical switching is useful for differential measurements (where the ratio of emission intensities can be taken for a non-zero and zero electrical field) and is also for charging procedures that involve rapidly flushing the sample of built-up impurities across charge traps.

Recently, the Schottky diode was used in tandem with a variety of tunnelling barriers with differing thickness to show a series of low temperature electron and nuclear spin relaxation rates down to 1s^{-1} and $10^{-3}s^{-1}$ for the single electrons and nuclei respectively (the inverse of these rates referring to the amount of time these spins could remain inside the QD as a quantum memory, for example) [131]. The results of that work allowed for an exploration of electron co-tunnelling, electron-phonon interactions, nuclear quadrupolar-strain coupling and other dephasing mechanisms such as those caused by charge traps and general material impurities, all with the goal of attempting to maximise the stability and coherence of confined charges. At low magnetic fields, the electron spin lifetimes are limited by co-tunneling rates between the QD and the Fermi reservoir of the n- contact, meaning that fundamentally the time for which the electron reliably maintains its spin within the QD is governed by the diode itself, rather than QD quality. At higher fields, phonon-assisted relaxation dominates spin decoherence, meaning that such fields are not necessarily appropriate for spin control. Much of this work is performed resonantly, and relies on the mechanism of spin pumping to initialise states.

Despite the success of the study of single charge interactions between a lone spin and the environmental effects on the coherence of the spin, the Schottky diode is not used to study nanophotonic devices as the metal contact is too difficult to efficiently etch, potentially creating non-uniform sidewalls of etches surfaces and changes to the potential refractive index contrast which assists with electromagnetic confinement within the waveguide geometry. Additionally, etching methods such as inductively-coupled plasma etching (which is used to perform deep etches into the semiconductor layers to allow for the suspension of devices - see section 2.2) require pure etching recipes which is not accessible on metal-covered samples.

Whilst the fundamental mechanisms are similar in other heterostructures designed to control the spin state of charges and nuclei, a heterostructure such as a p-i-n diode should not offer the same level of stability, for the reason provided below. A p-i-n heterostructure (that is used for the majority of Sheffield's GaAs photonic devices) is employed here but it has been suggested that this diode can prove difficult for spin for resonant spin control - or even spin pumping - due to the currents that pass through the device.

Section 6.4 discusses this in further detail, and results are shown which prove the contrary. In ref [133], spin initialisation through coherent control was performed for a nanobeam in the low current regime in the very best of p-i-n diode; but in the Voigt field geometry. Genuine spin pumping was still only performed without the use of a cavity (to enhance specific transitions) in a p-i-n-i-n diode, with appreciable magnetic fields (much larger than 0.2T). A large motivation for pursuing this work but in the regular p-i-n diode is that it offers potentially huge Stark tuning ranges (in some work, up to 25meV has been shown [134]).

6.2 Resonance Fluorescence and Spin Pumping of QDs for State Initialisation

Electron spins are a robust choice as a static qubit which allow for long spin lifetimes and possess the benefit of being optically manipulated. Extensive research performed on spin-relaxation dynamics has resulted in the demonstration of electron spin lifetimes which exceed 1s (hole spins have been shown to persist for an order of magnitude larger, due to the lack of p-type wavefunction overlap at the location of the the nuclear spins [135]). Even more impressively, nuclear spin lifetimes can exist for hours. Such timescales are well beyond the usual timescales of quantum dot behaviour, such as nanosecond spontaneous emission times. The single spins left over after a spontaneous recombination event only occur for charged dots ($X^{+/-}$), leaving behind either an electron or a hole, depending on the constituents of the QD before e-h recombination. Within the Schottky wafer configuration, electron spin lifetimes have been found to last up to 20s at 4.2K for a singly-charged InGaAs QD. In order to achieve spin initialisation, a QD transition must be resonantly pumped.

The process of spin pumping is described here, starting with an explanation of quantum dot resonance fluorescence (RF). In chapters 1 and 2 (figures 1.3, 2.12), the simplest of quantum dot transitions are presented, being depicted as three or four energy levels occupied by up to three spins. Focus is made here on the X^{-1} state as it is single electrons which will experience spin shelving. In the presence of an external magnetic field (in the Faraday geometry), the X^{-1} transition can be described as a four level system, with each of the states: $|\uparrow\rangle$, $|\downarrow\rangle$, $|\uparrow\downarrow\Uparrow\rangle$ and $|\uparrow\downarrow\Downarrow\rangle$ having different energies within the QD. These levels are expanded upon from chapter 2's level diagram in figure 6.1. When non-resonant light is incident upon the QD, electron and hole spins can fall into the QD, but do so randomly, and

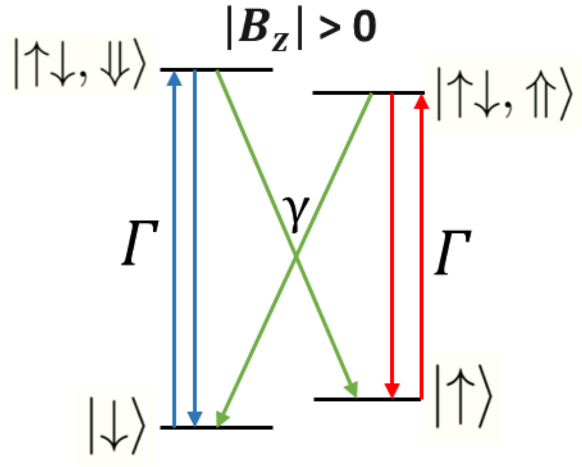
$|\uparrow\downarrow,\Downarrow\rangle$
$|B_z| > 0$
$|\uparrow\downarrow,\Uparrow\rangle$
Γ
γ
Γ
$|\downarrow\rangle$
$|\uparrow\rangle$

Figure 6.1: **Spin Pumping of a charged exciton, with lifted degeneracy of the ground state** | The colours illustrate the energy differences indicated by the distances between the transitions, which are arrow marked. As in figure 1.3 of the introduction, the arrows represent carrier spins. The green transitions allow for the shelving of the carriers, which are normally pumped up and down the red and blue transitions, depending on the carrier spin.

therefore the resulting trion spin states are also random. Under the magnetic field, the two allowed transitions (which conserve angular momentum) are orthogonally polarised and are at different energies. In order to selectively populate the states, a polarised and/or resonant laser is used. A polarised incident laser which is resonant to either of the transitions will excite that transition only (assuming the polarisation is appropriate), if the energy of the incoming laser is still spectrally close enough to the transition. If the incoming laser is spectrally far away enough from the transition, the maintenance of polarisation (through a so-called spin memory) is weakened [1]. With enough power, the emission results in a non-linear response, where the coherent, continuous driving of a single transition continuously populates one of the higher energy states. For example, a spin in the $|\downarrow\rangle$ state will become excited to reach the $|\uparrow\downarrow\Downarrow\rangle$. After a characteristic lifetime, the state will de-excite, releasing a photon of energy equal to the difference in energies of the $|\uparrow\downarrow\Downarrow\rangle$ and the $|\downarrow\rangle$ states. The resultant QD population of the electron and hole recombination will revert to the previous $|\downarrow\rangle$ state.

Figure 6.1 describes this process occurring with a rate Γ, which can translate to a single event basis with an assigned a probability. While only the "strongly" allowed transitions conserve angular momentum, the cross transitions ($|\uparrow\downarrow\Downarrow\rangle$ to $|\uparrow\rangle$ and $|\downarrow\uparrow\Uparrow\rangle$ to $|\downarrow\rangle$ can happen due to light and heavy hole admixtures. Such cross transitions are associated with a rate (or single-event probability) γ. Even though Γ is much larger than γ, the small probability of an excited state following a cross-transition pathway leaves the four-level system locked in one of the ground states associated with the cross-transition. This locking arises from the fact that the laser, which was once resonant with one of the transitions, is now resonant with a state that contains no spins. Moreover, in order to access the spin which has been shelved in the new state, the polarisation and energy of a resonant laser must be changed to match other of the two vertical transitions. This process of resonantly populating a charged transition QD and leaving a shelved charge is known as spin pumping. The time for which the charge is shelved is governed by both T_1, through various spin-flip processes like co-tunnelling [131, 136].

---

[1] see R. Oulton et al., PRL 98 107401 (2007)

It has been presented in literature that the p-i-n diode layering should not allow for spin pumping to take place. In the work presented in the main body and appendices [1], it was proposed that the p-i-n-i-n was necessary in order to reduce the current flow through the device. Moreover, it was suggested in 2013 that spin pumping at low magnetic fields ought not to be possible (B<0.3T) as the hyperfine interaction between nuclei is too pronounced, and nuclear-electron spin flipping can destroy the

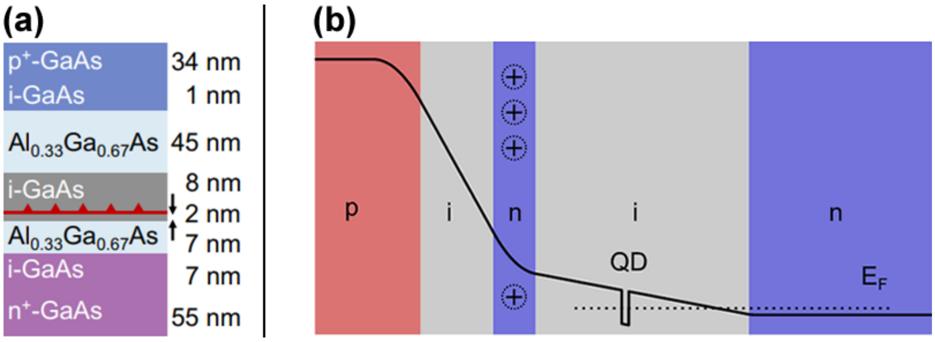

Figure 6.2: **(a): p-i-n vs (b): p-i-ni-n** | Colour coded on the right are the doping profiles, positively doped by the p label in red, and negatively by the n in blue. "i" (grey) indicates neutral doping and contains the thin QD layer, as seen in (**a**). The p-i-ni-n has a smaller voltage across the QD region in the centre than the p-i-n. (a) from [137], (b) from [1].

QD charge's spin. However, results are presented below on a strong spin pumping signature for a moderately chiral QD inside a nanobeam waveguide surrounded by a p-i-n wafer heterostructure. Figure 6.2 explores the differences between the standard p-i-n heterostructure and the p-i-ni-n.

6.3 The Charging Plateau

Spin pumping of the X^- state relies on the deterministic population of the QD with a single electron. RF can be achieved across a large voltage range as long as the laser remains resonant with the state, regardless of its Stark-shifted energy. The resonant laser, therefore, must be tuned to match the new QD energy. However, spin pumping can only be effectively achieved within a small window within the charging region of the X^- state. In the absence of a magnetic field for the X^- state, or in the case of a neutral exciton, spin pumping is not observable. The reason a neutral exciton can not experience spin pumping is that there is simply nothing to be pumped, as the recombination event of the exciton leaves the dot empty.

Within the single electron charging region of the QD, there are two main voltage/spectral regions of interest. Towards the edges of the charging region, where the X^- transition begins to be appear in PL from the start of the tunnelling region and where the X^{-2} (doubly charged QD) begins the form, population of the QD is unstable. This region is highlighted in figure 6.3, which shows a charging threshold for a single QD, transitioning between neutral and charged. While RF can take place (as the photon emission governed by the lifetime happens much faster than the QD charges can tunnel out), the lone spin undergoes rapid dephasing through processes like Auger recombination or co-tunnelling. The consequence of such processes is that a charge may be shelved through a cross-transition relaxation, but the shelving lasts only a very short amount of time. As a result, the spin behaves as if it experiences no shelving, as it is immediately available for the resonant transition again.

Within the centre of the charging region, by contrast, the electron spin is more

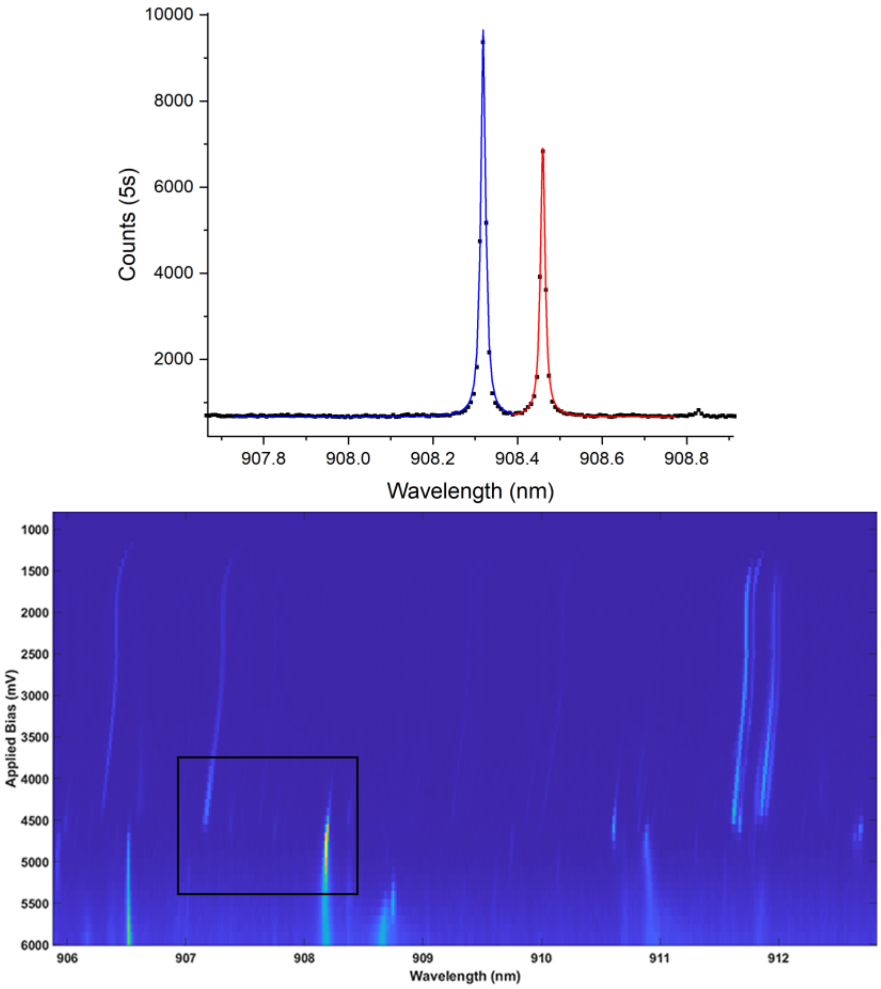

Figure 6.3: **PL map to find a charged exciton, and micro-photoluminescence of a magnetically split line under consideration for spin pumping** | The QD would be identified in the boxed region of the PL map. Linewidths are at least within the resolution limit of the highest order grating on the spectrometer (∼9pm). This QD is the QD for which spin pumping failed, despite the obvious identification of a charged exciton.

stable. Continuously driving the transition results in spin pumping, and the shelved charge's stability manifests as an intensity drop in the resonant scans, as the charge remains shelved for a much longer time before decoherence destroys the spin for the cycle to begin again.

Figure 6.4 diagrammatically explains the effect of charge stability on the resonance fluorescence spectrum. The figure shows the two cases of a neutral QD (in or out of a **B** field)/a charged exciton with zero applied field (left), and a spin-pumpable charged exciton in a magnetic field (right). It can be seen on the left of figure 6.4 that the intensity of the RF does not change across the majority of the voltage

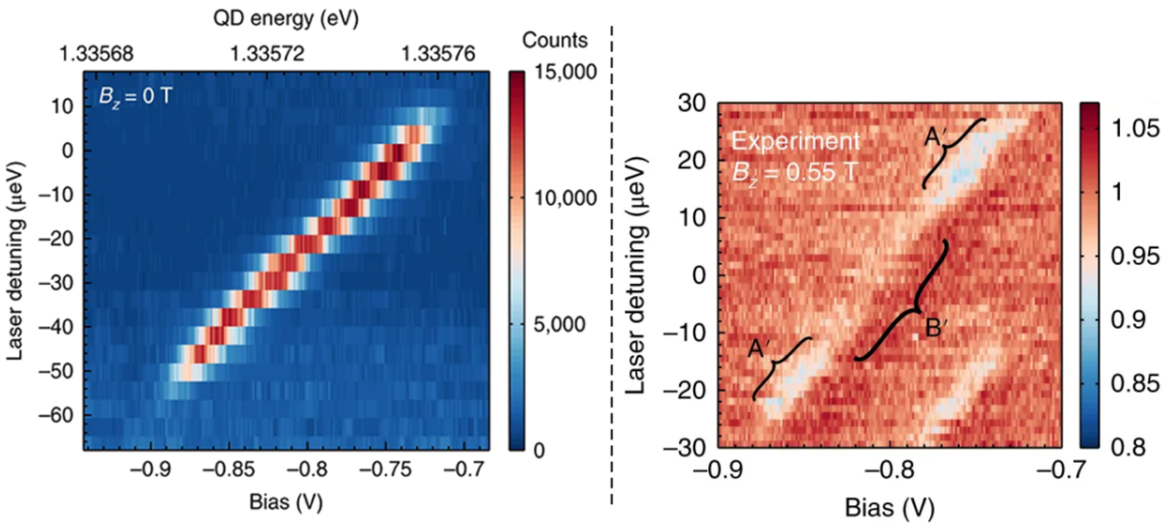

Figure 6.4: **Voltage plateau for a QD in zero field (left) and a non-zero B field (right)** | Both images are experimental data, showing the success of spin pumping at the centre of the voltage plateau. A resonant laser is scanned across a range of 70μeV across zero detuning. Images from [138]

plateau. On the right, the situation is more interesting. The very edges of the plateau are similarly cut off as they are on the left, as the usual charging thresholds appear. The RF intensity on the edges of the plateau surround a very dim, central section of the plateau. For this work, only a small magnetic field was needed to see this process (see figure 6.6 in the next section).

6.4 Spin Pumping Inside Nanobeam Waveguides

The first stages of achieving spin initialisation inside a QD require the identification of a QD with a narrow linewidth which also shows large emission intensities in μPL after the single-electron charging threshold of the diode. The general electrical behaviour and charging properties are found through the means of an electrical PL scan, an example of which is discussed in section 2.5.1. Such diagrams are generated by performing a short PL exposure at a series of applied external voltages in the reverse bias regime. Ideally, the built-in potential prevents the emission from QDs as generated charges are swept out to the p- and n- layers before they have the opportunity to fall into the QD to recombine. At a certain voltage, the bands begin to flatten around the QD allowing for the occupation of charge carriers through single-electron charging. In this regime, the QD can be sequentially occupied by electrons, with a limiting mechanism known as the Coulomb barrier. The Coulomb interaction between the charges prevents an influx of charges tunnelling into the dot, allow for control of single spins. While the injected spin is random, half of the time the electron spin will be appropriate for the transition being pumped.

The process of single electron charging is outlined in [104]. Once the QD transition is identified in low power μPL, the QD can be probed resonantly. Figure 6.3 showed the μPL for the single QD identified in a nanobeam waveguide wich demonstrated spin pumping. Light is collected from one outcoupler, in a magnetic field. The curves were fit with a Gaussian lineshape to produce a 15μeV FWHM, which is the minimum width measurable using an 1800 lines/mm grating and CCD combination. The data on the left of figure 6.5 is the brightest RF curve of the diagonal profile that is depicted on the right of the same figure. Low power is necessary to ensure that the transition location in μPL is as similar as possible to the resonant case. The production of many photo-excited carriers from above bandgap laser light can potentially cause charges to shield the QD from the heterostructure layers (i.e. the p-n junction), meaning that the effective Stark shift the QD states experience is reduced. Such a change alters the energy of the transition, requiring a wider scan of the parameter space to spectrally locate the transition.

A tuneable near- IR, single mode laser (860-920nm) is tuned to the approximate spectral location of the transition found in PL. The laser is then made to scan back and forth within a small voltage window, often of around 0.026nm (40μeV, which is a few lindwidths).

The collection path of the optical table is aligned to maximise the counts from the outcoupler (as the emission from an outcoupler has preferential polarisation) and the resonant excitation path is cross polarised to ensure there is no accidental collection of the incident laser. Such rejection is performed before the QD is directly excited. If the transition can be observed in zero magnetic field, the entire voltage plateau can be used to identify the QD as no spin pumping is possible, if not a wider range

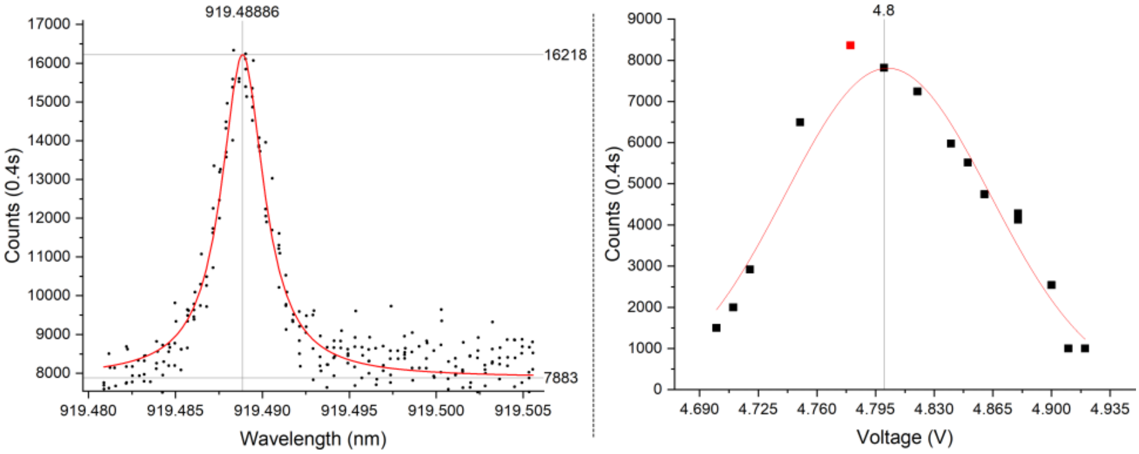

Figure 6.5: **RF voltage plateau along the diagonal of the full contour plot (shown in 6.4)** | The brightest RF curve along the plateau is shown on the left, and the brightest sections of the full diagonal profile is shown on the right. The Gaussian lineshape is expected for the diagonal plateau. The red data point is excluded from the fit.

of energies and voltages must be explored to find the transition at the edges.

Two different QDs were studied in the context of spin pumping. One showed no signature of spin pumping through RF intensity reduction. This is unexpected, and it might imply that the QD contained a neutral exciton state, even though both QDs were selected beyond the charging threshold defined in the PL maps. A discussion is provided later into the possible decoherence mechanisms which could destroy potential spin shelving. The other QD showed a strong sign of spin pumping by demonstrating an easily-measurable RF signal on the edges of the voltage plateau while also showing a drop in signal in the centre of the plateau as the magnetic field was turned on.

Resonance fluorescence for a QD that showed the spin-pumping signature is shown above in figure 6.5. This RF was taken at the brightest point of the voltage plateau for this transition, which is at the centre in zero field. By producing an RF curve at small voltage increments and calculating the integrated areas of a fitted Gaussian curve, a contour along the central axis of the voltage plateau is taken at zero magnetic field. This process allows for the identification of the outer edges of the plateau, where the differential measurements can take place. This contour is shown in part (b) of figure 6.5, and shows a voltage region similar to the one presented in the p-i-n-i-n diode (FWHM of 0.2mV). The side-by-side comparison of resonant

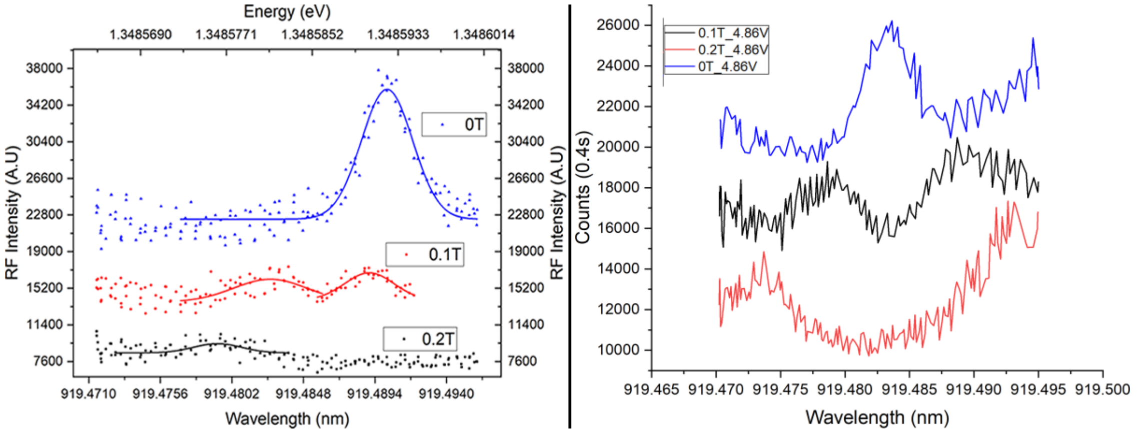

Figure 6.6: **Spin pumping signature for a charged QD. Left is at the centre of the plateau, right is at the plateau edges.** | Signal intensity quickly drops as soon as a magnetic field is applied at the plateau centre, in accordance with the electron spin becoming shelved/initialised. The fitted Gaussian curves drop over 5x in integrated area between 0T and 0.1T. The right side of the 0.2T data could not be fit as there is no appreciable curve. No clear sign of signal decrease occurs for the plateau edge data, shown on the right, which maintain their magnitudes.

laser scatter for the transition pumped at the centre and edges of the plateau are shown in figure 6.6. Data is presented for weak (Faraday) magnetic fields of 0.1T and 0.2T. Towards the edge of the plateau, the data, as expected, shows two clear (slightly broadened) peaks as the QD line splits. As the magnetic field changes, there is no appreciable change in the relative intensity between the peak areas before and after the magnetic field is applied. This is in complete contrast to the centre of the plateau, at 4.78V. Here, a strong RF signal at 0T is present, with a fitted linewidth of 3.3±0.1μeV. As the magnetic field is applied, the transition begins to split, and the transitions' intensities drastically decrease, and can be seen to decrease further between 0.1T and 0.2T.

The laser takes 12.5s to traverse the full extent of its scanning range, meaning that if the polarisation is not strictly overlapped with either of the circular transitions (e.g. the laser has a linear polarisation), both transitions will be expected to undergo spin pumping a number of times given the suggested spin lifetimes within the μs regime. Because the laser is resonant, the linear combination of the two circular polarisations is required, as exciting with one polarisation only would result in scanning across

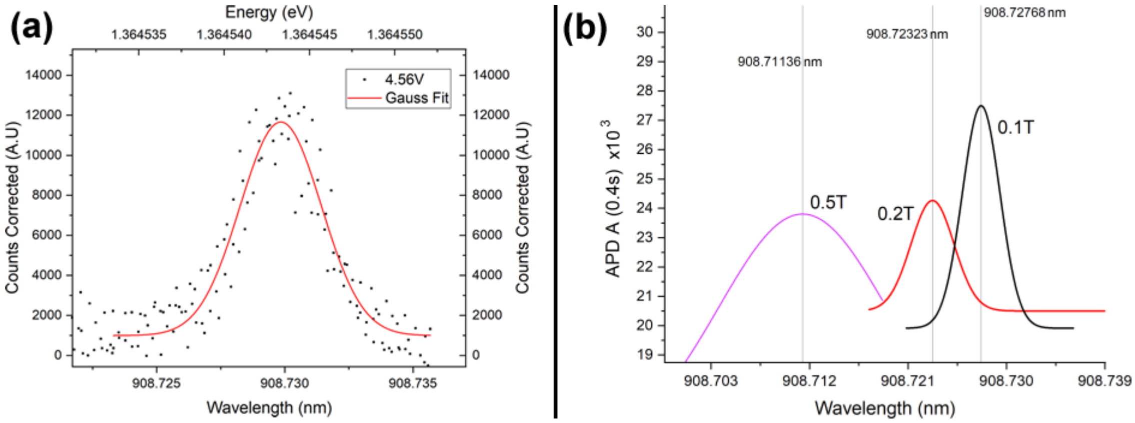

Figure 6.7: **(a): RF at zero magnetic field for a QD which did not experience spin-pumping. (b): Demonstration of RF failure through fields up to 0.5T** | (a): Sub-3pm RF at 0T, in the centre of this QD's plateau. (b): Spin pumping attempts at the centre of the plateau. The QD spectrally moves similarly to the one in figure 6.6, but there is no appreciable quenching of the RF intensity, even though the data is taken at the centre of the RF plateau. The central wavelength of each curve is marked explicitly to denote the differences in energy induced by the magnetic field. The broadening of the 0.5T curve is discussed in the main text.

only one of the Zeeman transitions. The linear polarisation, while providing a smaller effective power to the transition over which it spectrally crosses (as half of the power is wasted on the wrong polarisation), allows both transitions to be probed in one sweep. As a result, both transitions are expected to disappear when the laser is swept across them. In order to assist in the confirmation of spin pumping, resonance fluorescence data for a QD that did not show spin pumping signatures is shown. The identification process of this QD is the same as before. A sub 3pm resonance fluorescence curve at zero applied magnetic field is shown for the centre of the voltage plateau, with 100nW of resonant laser power. Data was taken at 0T, 0.1T, 0.2T and 0.5T (which should be substantial for spin pumping) and is presented in figure 6.7.

Only one transition is spectrally followed for this data set, but no pumping is observed as the integrated area does not quench at appreciable magnetic fields. Similarly, RF spectra towards the edges of the plateau show a similar, non-vanishing curve, demonstrating that this QD would not show signs of spin pumping. The spin initialisation fidelity can be extracted from equation D1 in the appendix of [1]. The calculation can be performed by using the RF integrated areas of the peaks at the plateau centre. By performing this, the spin initialisation fidelity can be calculated to be $F_{Spin} = 1 - \frac{RF_{B-on}}{RF_{B-off}} = 94\%$

6.5 Comparison of Spin Pumping Success Rates Between p-i-n and p-i-n-i-n Heterostructures

The advantages proposed in reference [1] of the p-i-n-i-n over the standard p-i-n are numerous. These include lower voltage thresholds required to achieve the flat-band regime and lower currents to reduce potential electroluminescence intensities and resistive (Ohmic) heating from gold contacts. It was proposed in that paper that in order to achieve spin pumping for appropriate spin memory in QIP, a minimised current is needed to avoid decoherence processes which occur “only” at biases close to 0V, which is near the flat-band in the n-i-n region. The p-i-n-i-n also maintains many of the benefits of the standard p-i-n insofar that the tunnelling barrier allows for deterministic charging through the Coulomb blockade while maintaining a small enough thickness to allow for nanophotonic confinement within the waveguide environment. However, it has been shown here that spin pumping is possible despite relatively large currents passing through the p-i-n diode. It is not clear, therefore, whether the requirement of lower currents passing through the sample is particularly important.

The I-V curve for this sample is provided alongside the charging map for a wider spectral range which includes, but is not limited to, the QD studied above. It can be seen that, in contrast to the sub-10μA currents presented in the appendices of ref [1], the currents present in the p-i-n sample are orders of magnitude larger, at 60μA at 4.85V - the plateau centre, which provides very strong evidence that the sheer magnitude of the current is not the relevant component for dephasing.

Low currents are suggested to be necessary to remove decoherence sources, as an electron drift through the diode could provide a source of electrons which are in much closer physical proximity to the embedded dot's own carriers. Both nanobeams are the same length from both groups, and so a hypothesis of low current specifically only near the emitter (due to resistance along the nanophotonic device) can be ruled out.

6.6 Conclusion

Spin pumping has been demonstrated inside a nanophotonic device to achieve spin preparation fidelities of 94%. Surprisingly, the results indicate that, unlike what refs [1, 139] suggest, low currents tunnelling through the heterostructure are not necessarily a clear requirement to achieve spin preparation. Further investigations should take place to determine how precisely it was possible, or perhaps why low currents aren't the principle reason for difficulty associated with spin preparation of an InGaAs QD embedded within a nanophotonic (p-i-n) device using a Faraday magnetic field.

Chapter 7

Further Work and Project Direction

To summarise, the three main chapters - 4, 5 and 6 - respectively involve novel work regarding the

- Design and fabrication of a variety of photonic structures that hybridise and maximise chirality, Purcell-enhancement and β-factor within
- Manipulation and reduction of QD lifetime for rapid, single photon emission via the assistance of electrical and magnetic tuning
- Measurement of high-fidelity spin initialisation (pumping) in a p-i-n diode

A variety of avenues exist to expand upon the work already completed in this thesis. This chapter presents a few possible links to continue the projects in the future.

7.1 Spin Pumping of Purcell-Enhanced, Chirally-Coupled Emitters Inside Glide-Symmetric Structures

Much of this thesis is geared towards the engineering and design of spin-friendly photonic crystal architectures. The goal in mind being an all-crystal-based, on-chip network of different photonic crystals with a variety of emitters which can be encouraged to emit directionally. In order to make the most of the chiral properties of these crystals, a hybridisation of the main chapters would be immediate and obvious way forwards. Housing emitters inside these chiral photonic crystals would enable deterministic and directional spin initialisation, which opens up a whole host of directions of work. First, the current nanobeam work is improved by allowing for brighter emission that is more likely directional, paving the way to deterministic spin transfer between two embedded emitters on the same chip. Secondly, the strong directional emission coupled with the improved light-matter interaction allows for the realisation of an even better single photon switch, as was presented by A. Javadi et al., in 2019.

7.2 Use of QD Registration to house Super-Radiant Emission

There has been some research effort in recent years into the investigation of waveguide-based superradiant studies. Most studies rely on individually tuning embedded emitters that are spectrally similar, either through Hafnium Oxide deposition, or striking lucky with the QCSE and two QDs having different electric polarisabilities and dipole moments. Once two emitters are brought into resonance, the strength of superradiance surfaces. Each QD emits in accordance to a particular lifetime, and therefore can be associated an individual brightness. When the two spectrally-distant have the same energy, the light generated from one may, through a stimulated emission process, influence the second QD to emit sooner than its usual lifetime would show. The result is a pair of QDs both emitting faster than either of the QDs individually, for generation of bright entangled photon sources.

Pre-registering the position of the QDs and marking their energies, devices can be arbitrarily constructed around these emitters to ensure that they share the same waveguide mode. Recent advances at Sheffield have enabled more efficient means of

QD registration, and so it would be a fairly simple and yet advantageous direction to employ the chiral glide planes in the context of measuring (Purcell-enhanced) superradiance.

A simple goal would be to match and enhance the results demonstrated in [140], by achieving superradiant emission of more than two QDs, where the solid state coherence of carriers have no opportunity of being affected by the local heating, thus eliminating many phonon effects. Explicitly demonstrating a reduced lifetime of all emitters, while maintaining enhanced photon number extraction could pave the way for bright entangled emission. This could be combined with chiral phenomena to achieve thresholdless lasing [141], but with the light generated within the passive structure with remarkable β-factors.

7.3 Measurement of Phase Shifts through Chiral Resonant Scattering

Though it is not discussed in this thesis, previous work in Sheffield involved the theoretical calculation of an ideal π phase shift provided to a single photon through the means of chiral interaction between a single photon and a chirally-coupled emitter. One of the largest factors limiting the scope of that work was the Beta factor, which ultimately drops the interaction probability on a per-photon basis, and therefore the brightness when integrated over multiple interaction cycles. Moreover, the stronger chirality makes the finding of a QD candidate much higher, meaning much less time would be spent on locating a QD, as was done in the phase shift work presented by D. Hurst et al., in 2018. This work was not performed in a charge-controllable heterostructure. With the work in this thesis showing that the basic p-i-n heterostructure is enough to house resonant work, performing phase shift estimations, or even real measurements (see below) would be possible.

7.3.1 The Implementation of an on-chip Mach-Zender Interferometer for Induced Phase Shifts on Flying Qubits

As listed in the Chiral Quantum Optics review by P. Lodahl, one of the ultimate triumphs for linear-based on-chip QIP is the generation of a Mach-Zender interferometer, with the ability to deterministically measure *and* provide a π phase shift to flying qubits along the chip. This idea follows from the section above, where single photons can experience a full π phase rotation by means of interacting with a QD, not only in the stable environment of a p-i-n heterostructure, but in one where the chirally coupled (phase-applying) emitter can be effectively turned on and off with an applied electric field. If one can produce a working MZI, measureabale phase shifts are possible that should theoretically beat polaritonic work, and at least match the free space cavity work demonstrated by the Warburton group this year.

Finally, and perhaps the most basic of avenues, lies on the further study of the current designs to completely ensure the best figures of merit are achieved. This may involve generating new designs which adiabatically reduce the indentation size of the glide plane nanobeam adapter in the fully-optimised glide lane structures, or even studying the GPN further, investigating the Purcell factor experimentally. Like most PhD projects, this was time-limited, and a hierarchy of priorities did not bring a full investigation into the GPN to light.

Chapter 8

Conclusion

This thesis studied a basic overview into the world of quantum information processing, and presented a possible engineering solution to some of the most basic fundamental requirements regarding a potential linear optical information processor. By generating new designs, or improving other older ones, a platform for directionally guiding and controlling the flow of light-based information on-chip is introduced. This platform boasts some of the best figures of merit ever seen in a photonic crystal waveguide interface, hosting a record-breaking emission enhancement in the waveguide geometry. Additionally, this thesis demonstrated that well-established heterostructures are perfectly capable of hosting quantum memories (spins), which would only be improved by using the designs also introduced in the fourth chapter. Below is a summary of the main content of the thesis outside of the introduction and experimental methods.

8.1 Chapter 3

In order to manifest any of the proposed physics of nanophotonic architectures, the passive and specialist structures designed to guide and control the flow of light must be optimised from an engineering standpoint. This chapter introduced how chirality is generated within the nanophotonic environment, and potentially what it means for QIP. Starting at a basic design such as a suspended nanobeam waveguide, a series of more complicated (and yet related) devices are discussed, with the ultimate design being a type of photonic crystal with glide symmetry. Alterations to hole periodicity, sizes, and positions, all combined with appropriate adapters and tapers, allowed for the definitive design of photonic crystal, embodying strong chirality, unity beta factors and slow light effects. Preliminary data presented on a few of the sub-components of the ultimate design showed their lack of individual viability as candidates for passive nanophotonic elements. However, this investigation allows for important considerations when designing the optimum overarching device containing the sub-elements. Specifically, studying the glide plane nanobeam structure, in section 3.5.3, allowed designs to be changed to ensure that their band gaps did not interfere with the relatively broadband slow light regions of the glide plane waveguide.

8.2 Chapter 4

Shorter than the rest, the purpose of this chapter was to outline the experimental method of determining the chiral contrast of the nanophotonic devices used. Instead of using the direct single photon transmission as outlined at the end of the introduction, the much simpler approach is taken to observe the relative intensities collected at the device ends. After presenting a simple exploratory test for a nanophotonic device, examples of emitters are shown which demonstrate chiral behaviour. A divergence is made to show a potential difficulty in the determination of chiral contrast due to potential QD asymmetries (with different values for directional beta factors) combined with a Fabry-Perót fringing from device back reflections. Following this are reassurances relating to the behavioural consistency of an emitter with regards to two device properties. First, simulation results are presented to show the robustness of the beta factor with respect to the emitter's position within a glide plane waveguide. This is in contrast to the issues presented by the chirality above. Next is the experimental extraction of the exciton g-factor through observing the energy splitting magnitude of the two circularly polarised components within a magnetic field. The strong correlation shows that, at least, there is no dependence of the chirality across a varying magnetic field. The chapter summarises that it is possible to extract both β and $C_{L/R}$ experimentally, so long as appropriate consideration is taken regarding the differences in C_L and C_R due to the effects discussed previously.

8.3 Chapter 5

In this chapter, the record-breaking lifetime for a QD embedded in a waveguide architecture is presented. Magnetic and electric fields are used to induce a spectral tuning of the emission energy of a quantum dot. First, a base series of reference lifetimes are shown. Nanobeam lifetimes are presented, which show a relative Purcell enhancement to the lifetime of emitters within the bulk of the wafer. The small enhancement, as predicted by the reduced mode volume caused by the size of the waveguide, shows the consistency of the structures ability to change the emission properties. Data is then presented to show that, individually, within a nanophotonic device, the lifetime does not intrinsically depend on an electric or magnetic field. This is important when studying the main series of data, which looks at a QD near the slow light region of the device. Over a tuning range of only 1.6nm, QD lifetimes of 69ps are produced, starting from a lifetime just above 725ps. When the same voltage range is studied in the nanmobeam (a device with no appreciable dispersion within the wavelength ranges involved), emitter lifetimes do not change. In addition to this, a series of reasonably chiral dots with impressively short lifetimes are shown, to advertise the promising yield of the devices. To conclude, a powerful insight as to the effectiveness of the glide plane waveguide is presented. Chiral dots can be shown to regularly have highly Purcell-enhanced lifetimes.

8.4 Chapter 6

Finally, this chapter oversaw a demonstration of a physical process that was deemed unlikely by other research groups within a particular set of conditions. The overall goal was the demonstration of spin pumping of a InGaAs QD within a p-i-n diode structure. Single electron charging was achieved within a nanobeam waveguide by slowly changing the diodes' bias voltage. By using a tuneable laser to facilitate resonant excitation, charged exciton states were located with an energy that depended on the applied voltage. Scanning across the applied bias, a voltage plateau was achieved. Application of a weak external magnetic field allowed the observation of a total loss of signal towards the edges of the plateau, whilst the spin states remained visible at the edges of the plateau - a key signature of spin pumping.

The potential avenues of this work are numerous. First, it should be suggested that spin pumping be demonstrated across a wider range of QDs within a different sample, with a better working diode. The sample used in this chapter contained diodes with drastically different behaviour, with some showing large turn-on voltages, such as 8V. Many diodes also showed electroluminescence on-set very close to the charging threshold, which will naturally destroy the Coulomb blockade within QDs through saturation of carriers.

After the reliable demonstration of spin-pumping, with the fidelities shown in this work (i.e. at least 96%), the process should be modified to include a second resonant laser which will revitalise the signal. This functions by having the second laser resonant with the transition into which the first laser pumps the electron. In principle, time-resolved experiments would show shelving times, furthering a relatively untapped investigative avenue.

Spin-pumping encompasses one of the DiVincenzo criteria, which is the initialisation of the static qubit. By embedding this with the chiral interface, a vital direction of this research would be: the initialisation of a chirally-coupled quantum dot, which sends light in one direction only - *depending on the specific spin state.* This directionally emitted light can excite a second QD. Either this QD could be used as a quantum repeater, whose emission is stimulated by the incoming photon. Alternatively, the secondary static bit could be read out, in terms of spin transfer, or even spin-flipped through radio frequency pulses. This control would subsequently allow for emission into the other direction, demonstrating full optical control for photon routing. Utilising the glide plane waveguide would enhance the chirality for these potentialities, alongside ensuring sufficiently high interaction probabilities through the strong β-factors.

Appendix A

Appendix

Some PL and lifetime measurements are presented here for the QDs in table 5.8. The g(2) measurements are for the fastest QD shown in figure 5.11.

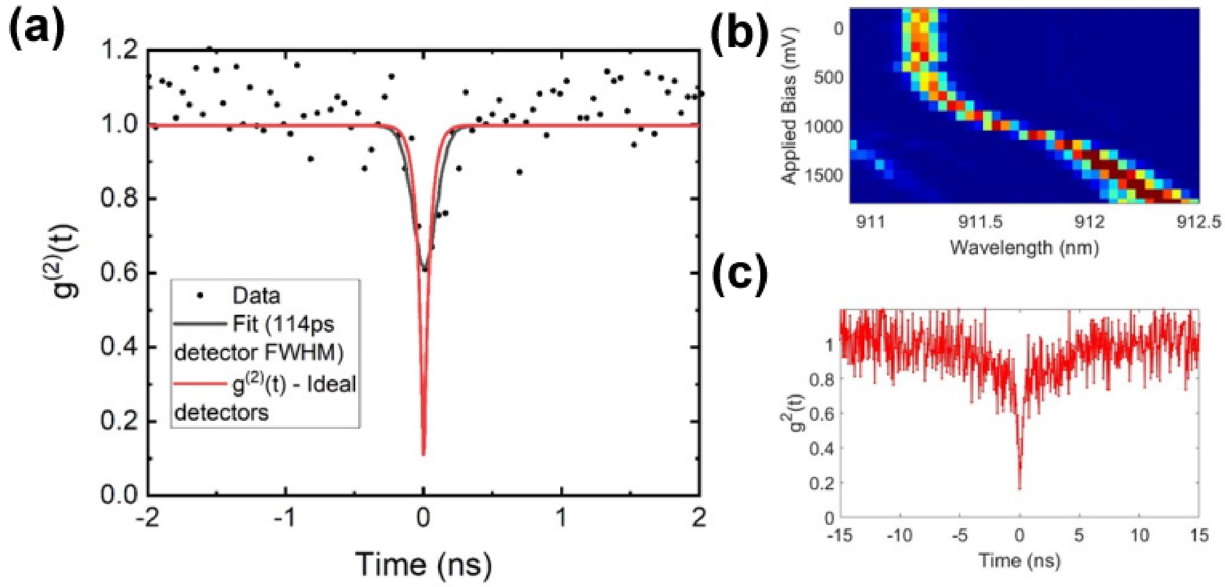

Figure A.1: **Second order correlation of the tuned QD from figure 5.11** | (a) shows the $g^2(0)$ when the QD is tuned to the shortest wavelength, seen in (b). When convolved with the detector response, the $g^2(0)$=0.11. The $g^2(0)$ without deconvolution when the QD is at the longer wavelength is shown in (c), with a value of 0.16. This proves the single photon nature of the emitter.

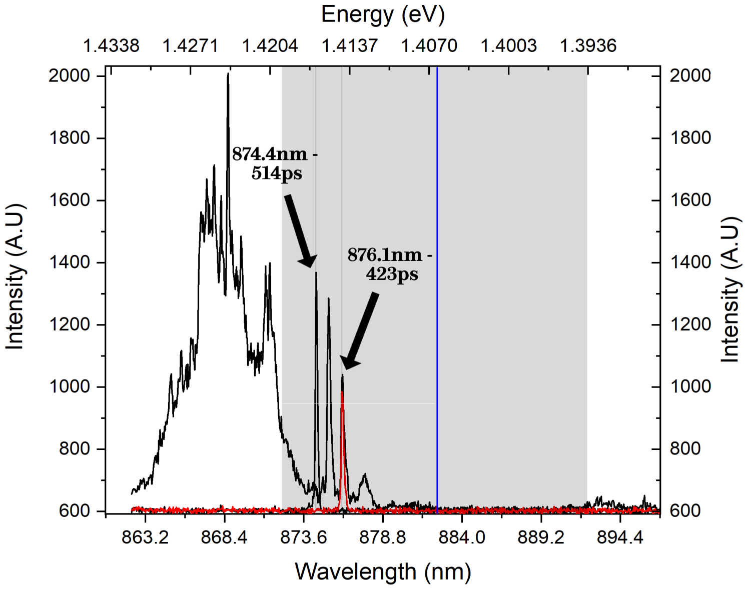

(a) Device 1 slow light region

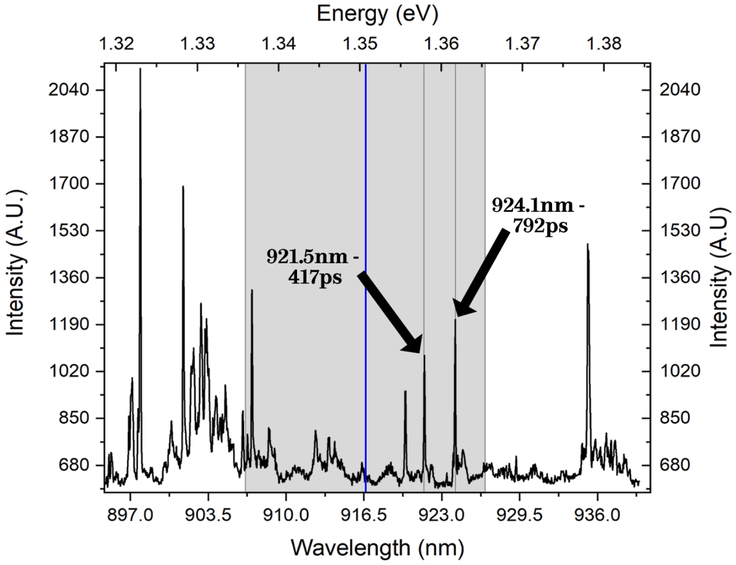

(b) Device 5 slow light region

Figure A.2: Two spectra are presented for Device 1, in red (filtered) and black. The blue line indicates the slow light position, and the grey shading indicates a 10nm window either side of it. Lifetimes of QDs are arrow marked.

.

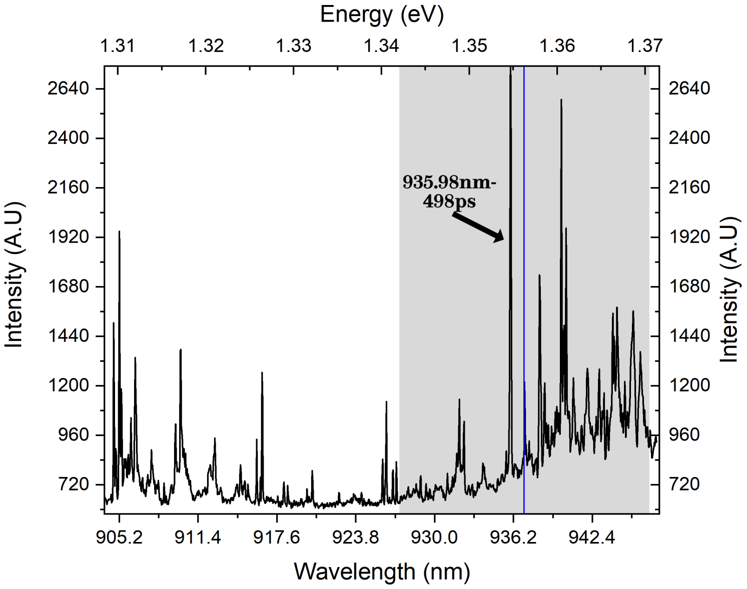

(a) Device 10 slow light region

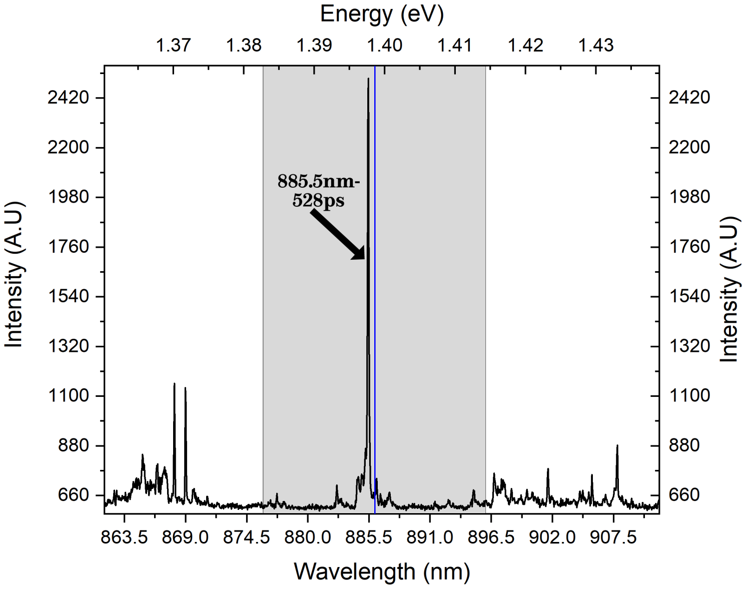

(b) Device 17 slow light region

Figure A.3: The blue line indicates the slow light position, and the grey shading indicates a 10nm window either side of it. Lifetimes of QDs are arrow marked.

Bibliography

1. Lobl, M. C. *et al.* Narrow optical linewidths and spin pumping on charge-tunable close-to-surface self-assembled quantum dots in an ultrathin diode. *Physical Review B* **96,** 165440 (2017).
2. Fortsch, M. *et al.* A versatile source of single photons for quantum information processing. *Nature communications* **4,** 1–5 (2013).
3. Pearce, E., Phillips, C. C., Oulton, R. F. & Clark, A. S. *A Fiber Photon-Pair Source for Enhanced Spectroscopy and Imaging* in *Nonlinear Optics* (2021), NM2B–5.
4. Chen, J., Pearlman, A. J., Ling, A., Fan, J. & Migdall, A. A versatile waveguide source of photon pairs for chip-scale quantum information processing. *Optics express* **17,** 6727–6740 (2009).
5. Fiorentino, M. *et al.* Spontaneous parametric down-conversion in periodically poled KTP waveguides and bulk crystals. *Optics express* **15,** 7479–7488 (2007).
6. Pravia, M. A. *et al.* Robust control of quantum information. *The Journal of chemical physics* **119,** 9993–10001 (2003).
7. Hincks, I., Granade, C., Borneman, T. W. & Cory, D. G. Controlling quantum devices with nonlinear hardware. *Physical Review Applied* **4,** 024012 (2015).
8. O'brien, J. L. Optical quantum computing. *Science* **318,** 1567–1570 (2007).
9. Kozhekin, A., Molmer, K. & Polzik, E. Quantum memory for light. *Physical Review A* **62,** 033809 (2000).

10. Zhao, R. *et al.* Long-lived quantum memory. *Nature Physics* **5,** 100–104 (2009).

11. Lvovsky, A. I., Sanders, B. C. & Tittel, W. Optical quantum memory. *Nature photonics* **3,** 706–714 (2009).

12. Specht, H. P. *et al.* A single-atom quantum memory. *Nature* **473,** 190–193 (2011).

13. Lugiato, L., Gatti, A. & Brambilla, E. Quantum imaging. *arXiv preprint quant-ph/0203046* (2002).

14. Wolley, O., Gregory, T., Beer, S., Higuchi, T. & Padgett, M. Quantum imaging with a photon counting camera. *Scientific Reports* **12,** 1–9 (2022).

15. Lahiri, M., Viswanathan, B. & Lemos, G. B. *Twin-photon Correlations in Quantum Imaging with Undetected Photons* in *Quantum 2.0* (2022), QW2A–22.

16. Feynman, R. P. Optical quantum computing. *International Journal of Theoretical Physics* **21,** 467–488 (1982).

17. DiVincenzo, D. P. The physical implementation of quantum computation. *Fortschritte der Physik: Progress of Physics* **48,** 771–783 (2000).

18. Wang, X. *et al.* III–V compounds as single photon emitters. *Journal of Semiconductors* **40,** 071906 (2019).

19. Englund, D. *et al.* Ultrafast photon-photon interaction in a strongly coupled quantum dot-cavity system. *Physical review letters* **108,** 093604 (2012).

20. Stace, T., Milburn, G. J. & Barnes, C. Entangled two-photon source using biexciton emission of an asymmetric quantum dot in a cavity. *Physical Review B* **67,** 085317 (2003).

21. Bliokh, K. Y. & Nori, F. Transverse and longitudinal angular momenta of light. *Physics Reports* **592,** 1–38 (2015).

22. Bliokh, K. Y., Rodriguez-Fortuno, F. J., Nori, F. & Zayats, A. V. Spin-orbit interactions of light. *Nature Photonics* **9,** 796–808 (2015).

23. Vetsch, E. *et al.* Optical interface created by laser-cooled atoms trapped in the evanescent field surrounding an optical nanofiber. *Physical review letters* **104,** 203603 (2010).

24. Mitsch, R., Sayrin, C., Albrecht, B., Schneeweiss, P. & Rauschenbeutel, A. Exploiting the local polarization of strongly confined light for sub-micrometer-resolution internal state preparation and manipulation of cold atoms. *Physical Review A* **89,** 063829 (2014).

25. Knill, E., Laflamme, R. & Milburn, G. J. A scheme for efficient quantum computation with linear optics. *nature* **409,** 46–52 (2001).

26. Browne, D. E. & Rudolph, T. Resource-efficient linear optical quantum computation. *Physical Review Letters* **95,** 010501 (2005).

27. Kok, P. *et al.* Linear optical quantum computing with photonic qubits. *Reviews of modern physics* **79,** 135 (2007).

28. Sergienko, A., Kiess, T., Shih, Y., Rubin, M. & Alley, C. *Quantum correlation of polarization of two-photon entangled state in type-II spontaneous parametric downconversion* in *OSA Annual Meeting* (1993), WXX–2.

29. Magnitskiy, S. *et al.* A SPDC-based source of entangled photons and its characterization. *Journal of Russian Laser Research* **36,** 618–629 (2015).

30. Haque, A. & Sumaiya, S. An Overview on the Formation and Processing of Nitrogen-Vacancy Photonic Centers in Diamond by Ion Implantation. *Journal of Manufacturing and Materials Processing* **1.** ISSN: 2504-4494 (2017).

31. Childress, L. & Hanson, R. Diamond NV centers for quantum computing and quantum networks. *MRS Bulletin* **38,** 134–138 (2013).

32. Benson, O., Santori, C., Pelton, M. & Yamamoto, Y. Regulated and entangled photons from a single quantum dot. *Physical review letters* **84,** 2513 (2000).

33. Fiorentino, M., Voss, P. L., Sharping, J. E. & Kumar, P. All-fiber photon-pair source for quantum communications. *IEEE Photonics Technology Letters* **14,** 983–985 (2002).

34. Smith, B. J., Mahou, P., Cohen, O., Lundeen, J. & Walmsley, I. Photon pair generation in birefringent optical fibers. *Optics express* **17,** 23589–23602 (2009).

35. Fang, B., Cohen, O. & Lorenz, V. O. Polarization-entangled photon-pair generation in commercial-grade polarization-maintaining fiber. *JOSA B* **31,** 277–281 (2014).

36. Kang, D., Kim, M. & Helmy, A. S. Two polarization-entangled sources from the same semiconductor chip. *Physical Review A* **92,** 013821 (2015).

37. Matthews, J. C. F., Politi, A., Bonneau, D. & O'Brien, J. L. Heralding Two-Photon and Four-Photon Path Entanglement on a Chip. *Phys. Rev. Lett.* **107,** 163602 (16 2011).

38. Huber, T. *et al.* Coherence and degree of time-bin entanglement from quantum dots. *Phys. Rev. B* **93,** 201301 (20 2016).

39. Appel, M. H. *et al.* Entangling a Hole Spin with a Time-Bin Photon: A Waveguide Approach for Quantum Dot Sources of Multiphoton Entanglement. *Phys. Rev. Lett.* **128,** 233602 (23 2022).

40. Antelius, M., Gylfason, K. B. & Sohlstrom, H. An apodized SOI waveguide-to-fiber surface grating coupler for single lithography silicon photonics. *Opt. Express* **19,** 3592–3598 (2011).

41. Sattari, H. *et al.* Compact broadband suspended silicon photonic directional coupler. **45** (2020).

42. Lu, Z. *et al.* Broadband silicon photonic directional coupler using asymmetric-waveguide based phase control. *Opt. Express* **23,** 3795–3808 (2015).

43. Fainman, Y. *et al.* Silicon nanophotonic devices for chip-scale optical communication applications [Invited]. *Applied Optics* **52,** 613–624. ISSN: 1559-128X (2013).

44. Schnauber, P. *et al.* Indistinguishable Photons from Deterministically Integrated Single Quantum Dots in Heterogeneous GaAs/Si 3 N 4 Quantum Photonic Circuits. *Nano letters* **19,** 7164–7172. ISSN: 1530-6984 (2019).

45. Vermersch, B., Ramos, T., Hauke, P. & Zoller, P. Implementation of chiral quantum optics with Rydberg and trapped-ion setups. *Phys. Rev. A* **93,** 063830 (6 2016).

46. Lanyon, B. P. *et al.* Universal Digital Quantum Simulation with Trapped Ions. *Science* **334,** 57–61 (2011).

47. Pla, J. J. *et al.* Coherent Control of a Single ^{29}Si Nuclear Spin Qubit. *Phys. Rev. Lett.* **113,** 246801 (24 2014).

48. Nakamura, Y., Pashkin, Y. A. & Tsai, J. S. *Coherent control of macroscopic quantum states in a single-Cooper-pair box* 1999.

49. Bladh, K., Duty, T., Gunnarsson, D. & Delsing, P. The single Cooper-pair box as a charge qubit. *New Journal of Physics* **7,** 180–180 (2005).

50. Hafenbrak, R. *et al.* Triggered polarization-entangled photon pairs from a single quantum dot up to 30K. *New Journal of Physics* **9,** 315–315 (2007).

51. Ramsay, A. J. A review of the coherent optical control of the exciton and spin states of semiconductor quantum dots. *Semiconductor Science and Technology* **25,** 103001 (2010).

52. Huggenberger, A. *et al.* Narrow spectral linewidth from single site-controlled In(Ga)As quantum dots with high uniformity. *Applied Physics Letters* **98,** 131104 (2011).

53. Ramsay, A. J. A review of the coherent optical control of the exciton and spin states of semiconductor quantum dots. **25,** 103001. ISSN: 0268-1242 (2010).

54. Kim, C. C., Garland, J. W., Abad, H. & Raccah, P. M. Modeling the optical dielectric function of semiconductors: Extension of the critical-point parabolic-band approximation. *Phys. Rev. B* **45,** 11749–11767 (20 1992).

55. Sturge, M. D. Optical Absorption of Gallium Arsenide between 0.6 and 2.75 eV. *Phys. Rev.* **127,** 768–773 (3 1962).

56. Yamaguchi, K., Yujobo, K. & Kaizu, T. Stranski-Krastanov Growth of InAs Quantum Dots with Narrow Size Distribution. *Japanese Journal of Applied Physics* **39,** L1245–L1248 (2000).

57. Carmesin, C. *et al.* Structural and optical properties of InAs/(In)GaAs/GaAs quantum dots with single-photon emission in the telecom C-band up to 77 K. *Phys. Rev. B* **98,** 125407 (12 2018).

58. Bayer, M. & Forchel, A. Temperature dependence of the exciton homogeneous linewidth in InGaAs self-assembled quantum dots. *Phys. Rev. B* **65,** 041308 (4 2002).

59. Lohrmann, A., Johnson, B. C., McCallum, J. C. & Castelletto, S. A review on single photon sources in silicon carbide. *Reports on Progress in Physics* **80,** 034502 (2017).

60. Aghaeimeibodi, S. *et al.* Integration of quantum dots with lithium niobate photonics. *Applied physics letters* **113,** 221102. ISSN: 0003-6951 (2018).

61. Jin, B., Mishra, D. & Argyropoulos, C. Efficient single-photon pair generation by spontaneous parametric down-conversion in nonlinear plasmonic metasurfaces. *Nanoscale* **13,** 19903–19914 (47 2021).

62. Liu, S. *et al.* Thermo-optic phase shifters based on silicon-on-insulator platform: state-of-the-art and a review. *FRONTIERS OF OPTOELECTRONICS* **15.** ISSN: 2095-2759 (2022).

63. Coles, R. *et al.* Chirality of nanophotonic waveguide with embedded quantum emitter for unidirectional spin transfer. *Nature communications* **7,** 11183–11183. ISSN: 2041-1723 (2016).

64. Mrowiński, P. *et al.* Directional Emission of a Deterministically Fabricated Quantum Dot–Bragg Reflection Multimode Waveguide System. *ACS photonics* **6,** 2231–2237. ISSN: 2330-4022 (2019).

65. Winger, M., Badolato, A., Hennessy, K. J., Hu, E. L. & Imamoglu, A. Quantum Dot Spectroscopy Using Cavity Quantum Electrodynamics. *Phys. Rev. Lett.* **101,** 226808 (22 2008).

66. Ovenden, C. *Development and characterisation of site-controlled quantum dot arrays* PhD thesis (2021).

67. Flissikowski, T., Betke, A., Akimov, I. A. & Henneberger, F. Two-Photon Coherent Control of a Single Quantum Dot. *Phys. Rev. Lett.* **92,** 227401 (22 2004).

68. Mortemousque, P.-A. *et al.* Coherent control of individual electron spins in a two dimensional array of quantum dots (2018).

69. Gaudreau, L. *et al.* Coherent control of three-spin states in a triple quantum dot. *Nature physics* **8,** 54–58. ISSN: 1745-2473 (2012).

70. Brash, A. *Ultrafast Dynamics of Single Quantum Dots* PhD thesis (2016).

71. Petersen, J., Volz, J. & Rauschenbeutel, A. Chiral nanophotonic waveguide interface based on spin-orbit interaction of light. *Science (American Association for the Advancement of Science)* **346,** 67–71. ISSN: 0036-8075 (2014).

72. Ramos, T., Pichler, H., Daley, A. J. & Zoller, P. Quantum Spin Dimers from Chiral Dissipation in Cold-Atom Chains. *Phys. Rev. Lett.* **113,** 237203 (23 2014).

73. Antoniadis, N. O. *et al.* A chiral one-dimensional atom using a quantum dot in an open microcavity. *NPJ Quantum* **8,** 1–5. ISSN: 2056-6387 (2022).

74. Hurst, D. L. *et al.* Nonreciprocal Transmission and Reflection of a Chirally Coupled Quantum Dot. *Nano letters* **18,** 5475–5481. ISSN: 1530-6984 (2018).

75. Smith, D. K., Goodfellow, B., Smilgies, D.-M. & Korgel, B. A. Self-assembled simple hexagonal AB2 binary nanocrystal superlattices: SEM, GISAXS, and defects. *Journal of the American Chemical Society* **131,** 3281–3290 (2009).

76. Ameh, E. A review of basic crystallography and x-ray diffraction applications. *The international journal of advanced manufacturing technology* **105,** 3289–3302 (2019).

77. Zhou, W. & Greer, H. F. What can electron microscopy tell us beyond crystal structures? *European Journal of Inorganic Chemistry* **2016,** 941–950 (2016).

78. Walker, M., Cryan, M., Strasser, P. & Srinivasan, K. Fabricating photonic crystals in InP. *III-Vs Review* **18,** 46–49 (2005).

79. Shalaev, M. I., Walasik, W., Tsukernik, A., Xu, Y. & Litchinitser, N. M. Robust topologically protected transport in photonic crystals at telecommunication wavelengths. *Nature nanotechnology* **14,** 31–34 (2019).

80. Conteduca, D. *et al.* Ultra-high Q/V hybrid cavity for strong light-matter interaction. *APL Photonics* **2,** 086101 (2017).

81. Zhan, J., Jafari, Z., Veilleux, S., Dagenais, M. & De Leon, I. High-Q nanobeam cavities on a silicon nitride platform enabled by slow light. *APL Photonics* **5,** 066101 (2020).

82. Kuruma, K., Ota, Y., Kakuda, M., Iwamoto, S. & Arakawa, Y. Surface-passivated high-Q GaAs photonic crystal nanocavity with quantum dots. *APL Photonics* **5,** 046106 (2020).

83. Tang, J. *et al.* Room temperature exciton–polariton Bose–Einstein condensation in organic single-crystal microribbon cavities. *Nature Communications* **12,** 3265 (2021).

84. Byrnes, T., Kim, N. Y. & Yamamoto, Y. Exciton–polariton condensates. *Nature Physics* **10,** 803–813 (2014).

85. Poole Jr, C. P. *Encyclopedic dictionary of condensed matter physics* (Academic Press, 2004).

86. Jaynes, E. T. & Cummings, F. W. Comparison of quantum and semiclassical radiation theories with application to the beam maser. *Proceedings of the IEEE* **51,** 89–109 (1963).

87. Manga Rao, V. S. C. & Hughes, S. Single quantum-dot Purcell factor and β factor in a photonic crystal waveguide. *Phys. Rev. B* **75,** 205437 (20 2007).

88. Santra, S., Cruikshank, B., Balu, R. & Jacobs, K. Fermi's golden rule, the origin and breakdown of Markovian master equations, and the relationship between oscillator baths and the random matrix model. *Journal of Physics A: Mathematical and Theoretical* **50,** 415302 (2017).

89. Micklitz, T., Morningstar, A., Altland, A. & Huse, D. A. Emergence of Fermi's Golden Rule. *Physical review letters* **129,** 140402 (2022).

90. Xu, S. & Fan, S. Fano interference in two-photon transport. *Phys. Rev. A* **94,** 043826 (4 2016).

91. Hallett, D. *Electrical Tuning of Integrated III-V Quantum Dots in Quantum Nano-Photonic Circuits* PhD thesis (2019).

92. Hurst, L. D. *Photon Scattering in Semiconductor Nanostructures* PhD thesis (2019).

93. Hurst, D. *et al.* Nonreciprocal transmission and reflection of a chirally coupled quantum dot. *Nano Letters* **18,** 5475–5481 (2018).

94. Lodahl, P. *et al.* Chiral quantum optics. *Nature* **541,** 473–480 (2017).

95. Antoniadis, N. O. *et al.* A chiral one-dimensional atom using a quantum dot in an open microcavity. *npj Quantum Information* **8,** 27 (2022).

96. Johnson, M. *et al.* A Critical Comparison Between Movpe and MBE Growth of III-V Nitride Semiconductor Materials for Opto-Electronic Device Applications. *MRS Proceedings* **537** (1999).

97. Guha, S., Madhukar, A. & Rajkumar, K. C. Onset of incoherency and defect introduction in the initial stages of molecular beam epitaxical growth of highly strained InxGa1-xAs on GaAs(100). *Applied Physics Letters* **57,** 2110–2112 (1990).

98. Danescu, A. The Asaro-Tiller-Grinfeld instability revisited. *International Journal of Solids and Structures* **38,** 4671–4684. ISSN: 0020-7683 (2001).

99. Griffiths, I. M. *Nuclear magnetic resonance studies of spin and strain phenomena in nanohole GaAs/AlGaAs quantum dots* PhD thesis (2021).

100. Price, D. M. *Chiral Interactions of Quantum Dots Embedded within Nanophotonic Wavegudies* PhD thesis (2019).

101. Stievater, T. H. *et al.* Rabi Oscillations of Excitons in Single Quantum Dots. *Phys. Rev. Lett.* **87,** 133603 (13 2001).

102. Press, D., Ladd, T. D., Zhang, B. & Yamamoto, Y. Complete quantum control of a single quantum dot spin using ultrafast optical pulses. **456.** ISSN: 0028-0836 (2008).

103. Yoneda, J. *et al.* A quantum-dot spin qubit with coherence limited by charge noise and fidelity higher than 99.9. **13.** ISSN: 1748-3387 (2018).

104. Warburton, R. J. Single spins in self-assembled quantum dots. **12.** ISSN: 1476-1122 (2013).

105. Van Bree, J., Silov, A. Y., Koenraad, P. M., Flatté, M. E. & Pryor, C. E. g factors and diamagnetic coefficients of electrons, holes, and excitons in InAs/InP quantum dots. *Phys. Rev. B* **85,** 165323 (16 2012).

106. Van Bree, J., Silov, A. Y., Koenraad, P. M. & Flatte, M. E. Geometric and compositional influences on spin-orbit induced circulating currents in nanostructures. *Phys. Rev. B* **90,** 165306 (16 2014).

107. Tholen, H. M. G. A. *et al.* Strain-induced g-factor tuning in single InGaAs/GaAs quantum dots. *Phys. Rev. B* **94,** 245301 (24 2016).

108. Nakaoka, T., Saito, T., Tatebayashi, J. & Arakawa, Y. Size, shape, and strain dependence of the g factor in self-assembled In(Ga)As quantum dots. *Phys. Rev. B* **70,** 235337 (23 2004).

109. Ulhaq, A. *et al.* Vanishing electron g factor and long-lived nuclear spin polarization in weakly strained nanohole-filled GaAs/AlGaAs quantum dots (2016).

110. Mehrabad, M. J. *et al.* Chiral topological photonics with an embedded quantum emitter. *Optica* **7,** 1690–1696. ISSN: 2334-2536 (2020).

111. Jalali Mehrabad, M. *et al.* A chiral topological add-drop filter for integrated quantum photonic circuits (2021).

112. Jalali Mehrabad, M. *et al.* A semiconductor topological photonic ring resonator. *Applied physics letters* **116,** 61102. ISSN: 0003-6951 (2020).

113. Coles, R. J. *Quantum Optical Circuits using III-V Nanophotonic Structures* PhD thesis (2015).

114. Zhou, X. *et al.* High-efficiency shallow-etched grating on GaAs membranes for quantum photonic applications. *Applied physics letters* **113,** 251103. ISSN: 0003-6951 (2018).

115. Lindley, D. Landmarks-The Birth of Photonic Crystals. eng. *Physics (College Park, Md.)* **6.** ISSN: 1943-2879 (2013).

116. Yablonovitch, E. Inhibited Spontaneous Emission in Solid-State Physics and Electronics. *Phys. Rev. Lett.* **58,** 2059–2062 (20 1987).

117. Yablonovitch, E. & Gmitter, T. Photonic band structure: The face-centered-cubic case. eng. *Journal of the Optical Society of America. A, Optics, image science, and vision* **7,** 1792–1800. ISSN: 1084-7529 (1990).

118. Purcell, E. M. in *Confined Electrons and Photons: New Physics and Applications* (eds Burstein, E. & Weisbuch, C.) 839–839 (Springer US, Boston, MA, 1995). ISBN: 978-1-4615-1963-8.

119. Hallett, D. *et al.* Electrical control of nonlinear quantum optics in a nanophotonic waveguide. *Optica* **5,** 644–650. ISSN: 2334-2536 (2018).

120. Liang, J., Ren, L.-Y., Yun, M.-J. & Wang, X.-J. Wideband slow light with ultralow dispersion in a W1 photonic crystal waveguide. **50,** G98–G103. ISSN: 1559-128X (2011).

121. Lang, B., Oulton, R. & Beggs, D. M. Optimised photonic crystal waveguide for chiral light-matter interactions. *Journal of optics (2010)* **19,** 45001. ISSN: 2040-8978 (2017).

122. Le Feber, B., Rotenberg, N. & Kuipers, L. Nanophotonic control of circular dipole emission. *Nature communications* **6,** 6695 (2015).

123. Sollner, I. *et al.* Deterministic photon emitter coupling in chiral photonic circuits. *Nature nanotechnology* **10,** 775–778 (2015).

124. Borri, P. *et al.* Ultralong Dephasing Time in InGaAs Quantum Dots. *Phys. Rev. Lett.* **87,** 157401 (15 2001).

125. Siampour, H. *et al.* Single quantum-dot Purcell factor and β factor in a photonic crystal waveguide. *ArXiv Preprint* **2208.06453** (2022).

126. Mahmoodian, S., Lodahl, P. & Sorensen, A. S. Quantum Networks with Chiral-Light–Matter Interaction in Waveguides. *Phys. Rev. Lett.* **117,** 240501 (24 2016).

127. Patil, C. M. *Experiments on Glide-Symmetric Photonic-Crystal Waveguides* PhD thesis (2020).

128. Liu, F. *et al.* High Purcell factor generation of indistinguishable on-chip single photons (2018).

129. Zhou, Y., Wang, Y., Yvind, K., Gregersen, N. & Pu, M. *High Purcell Factor Single-Photon Emitter based on Extreme Dielectric-Confinement GaAs-on-Insulator Waveguides* in *Conference on Lasers and Electro-Optics* (Optica Publishing Group, 2022), JTu3B.30.

130. Grijseels, S. *A study of radiative lifetimes, spectral wandering and radiative coupling of individual InAs quantum dots* PhD thesis (2016).

131. Gillard, G. *et al.* Fundamental limits of electron and nuclear spin qubit lifetimes in an isolated self-assembled quantum dot (2021).

132. Kroner, M. *et al.* Optical detection of single-electron spin resonance in a quantum dot. *Physical review letters* **100,** 156803 (2008).

133. Appel, M. H. *et al.* Coherent Spin-Photon Interface with Waveguide Induced Cycling Transitions. *Phys. Rev. Lett.* **126,** 013602 (1 2021).

134. Bennett, A. J. *et al.* Giant Stark effect in the emission of single semiconductor quantum dots. *Applied physics letters* **97,** 031104–031104-3. ISSN: 0003-6951 (2010).

135. Prechtel, J. H. *et al.* Decoupling a hole spin qubit from the nuclear spins. *Nature materials* **15,** 981–986 (2016).

136. Smith, J. *et al.* Voltage control of the spin dynamics of an exciton in a semiconductor quantum dot. *Physical Review Letters* **94,** 197402 (2005).

137. Kirsanske, G. *et al.* Indistinguishable and efficient single photons from a quantum dot in a planar nanobeam waveguide. *Phys. Rev. B* **96,** 165306 (16 2017).

138. Javadi, A. *et al.* Spin-photon interface and spin-controlled photon switching in a nanobeam waveguide. **13,** 398–403. ISSN: 1748-3387 (2018).

139. Pinotsi, D., Fallahi, P., Miguel-Sanchez, J. & Imamoglu, A. Resonant Spectroscopy on Charge Tunable Quantum Dots in Photonic Crystal Structures. **47,** 1371–1374. ISSN: 0018-9197 (2011).

140. Kim, J.-H., Aghaeimeibodi, S., Richardson, C. J., Leavitt, R. P. & Waks, E. Super-radiant emission from quantum dots in a nanophotonic waveguide. *Nano Letters* **18,** 4734–4740 (2018).

141. Ota, Y., Kakuda, M., Watanabe, K., Iwamoto, S. & Arakawa, Y. Thresholdless quantum dot nanolaser. *Optics Express* **25,** 19981–19994 (2017).